

Copyright © 2000, by the author(s).  
All rights reserved.

Permission to make digital or hard copies of all or part of this work for personal or classroom use is granted without fee provided that copies are not made or distributed for profit or commercial advantage and that copies bear this notice and the full citation on the first page. To copy otherwise, to republish, to post on servers or to redistribute to lists, requires prior specific permission.

**PICOSECOND ULTRASONIC  
CHARACTERIZATION OF MO/SI  
MULTILAYERS FOR EXTREME  
ULTRAVIOLET LITHOGRAPHY**

by

Nen-Wen Pu

Memorandum No. UCB/ERL M00/19

14 May 2000

**PICOSECOND ULTRASONIC  
CHARACTERIZATION OF MO/SI  
MULTILAYERS FOR EXTREME  
ULTRAVIOLET LITHOGRAPHY**

by

Nen-Wen Pu

Memorandum No. UCB/ERL M00/19

14 May 2000

**ELECTRONICS RESEARCH LABORATORY**

College of Engineering  
University of California, Berkeley  
94720

Picosecond Ultrasonic Characterization of Mo/Si Multilayers for  
Extreme Ultraviolet Lithography

by

Nen-Wen Pu

B.S. (Chung-Cheng Institute of Technology, Taiwan) 1990

M.S. (National Chiao-Tung University, Taiwan) 1994

A dissertation submitted in partial satisfaction of the

requirements for the degree of

Doctor of Philosophy

in

Engineering-Electrical Engineering  
and Computer Sciences

in the

GRADUATE DIVISION

of the

UNIVERSITY OF CALIFORNIA, BERKELEY

Committee in charge:

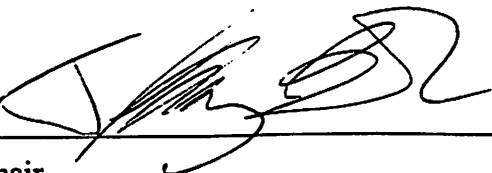
Professor Jeffrey Bokor, Chair

Professor Steven G. Louie

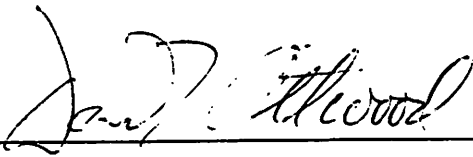
Professor David T. Attwood

Spring 2000

The dissertation of Nen-Wen Pu is approved:

 4/28/00  
\_\_\_\_\_  
Chair Date

 5/3/00  
\_\_\_\_\_  
Date

 5/4/2000  
\_\_\_\_\_  
Date

University of California, Berkeley

Spring 2000

**Picosecond Ultrasonic Characterization of Mo/Si Multilayers for  
Extreme Ultraviolet Lithography**

**© 2000**

**by**

**Nen-Wen Pu**

Abstract

Picosecond Ultrasonic Characterization of Mo/Si Multilayers for  
Extreme Ultraviolet Lithography

by

Nen-Wen Pu

Doctor of Philosophy in Engineering-Electrical Engineering  
and Computer Sciences

University of California, Berkeley

Professor Jeffrey Bokor, Chair

We have performed experimental and theoretical studies on the vibrational behavior of Mo/Si multilayers for EUV Lithography using picosecond ultrasonics. Foundations have been laid for applying this technique in nondestructive characterization of multilayer coatings. Picosecond ultrasonics is a pump-probe transient reflectivity technique in which the acoustic waves are impulsively excited by an ultrashort "pump" laser pulse and detected as a reflectivity change of a time-delayed "probe" pulse. In particular, surface modes lying within frequency gaps of the acoustic-phonon dispersion curve can be excited in a periodic structure.

An alternating-pump technique has been successfully demonstrated to enhance the signal-to-noise ratio by 10 to 20 dB. Up to three surface modes were observed in Mo/Si multilayers using this technique. Their frequencies depend on two coating parameters:  $d$  (the bilayer thickness), and  $\Gamma$  (thickness ratio of the Mo layer to bilayer) of multilayers, and these functional dependences have been studied both experimentally and

theoretically. By measuring two vibration frequencies simultaneously, we can extract  $d$  and  $\Gamma$ . To demonstrate the utility of this technique, we performed a cross-correlation experiment with EUV reflectometry on seven test samples. The results of these two techniques were in good agreement.

The non-vibrational part of the transient reflectivity change ( $\Delta R(\tau)$ ) was also studied. It was found that the small thermal conductivity in amorphous silicon causes the observed slow decay of the  $\Delta R(\tau)$  curves. We also discussed the issue of laser damage to multilayers. The mechanism for this damage is most likely due to relaxation of the intrinsic film stress. Its effect on EUV reflectivity was found negligible.

Two approaches were employed to simulate the physical process: Approach 1 ignored a thermal expansion term, resulting in absence of the non-vibrational signal. Nonetheless, various surface and bulk modes were seen. Approach 2 incorporated heat diffusion to calculate the thermal expansion term and allowed a finite delay time  $t_1$  for stress build-up. Simulations suggested that  $t_1 \sim 600$  fs, a rough estimate for the electron-phonon interaction time in Mo. The calculated strengths of vibration modes agreed well with the experiment. In addition, experimentally observed vibration spectra were reproduced.

A handwritten signature in black ink, appearing to be 'J. S. R.', located at the bottom center of the page.



**To my wife, Tracy,  
and my parents**

# Table of Contents

<b>List of Figures</b>	vii
<b>List of Tables</b>	xi
<b>Acknowledgements</b>	xii
<b>Chapter 1. Introduction</b>	1
1.1 Multilayer interference coatings	2
1.2 Picosecond ultrasonics	7
References	12
<b>Chapter 2. Theory of Picosecond Ultrasonics</b>	15
2.1 Acoustic pulse generation and detection in a bulk material	15
2.1.1 Generation of acoustic pulses	15
2.1.2 Detection of acoustic pulses	19
2.2 Theory of multilayer eigenmodes	21
2.2.1 Bulk modes in an infinite multilayer	23
2.2.2 Local modes at a free surface	28
2.3 $n$ -sublayer structure with cap layers	29
2.3.1 General solution for a capped $n$ -sublayer structure	31
2.3.2 Solution for a 4-sublayer system	34
2.3.3 Surface oxide treated as a cap layer	36

References	39
<b>Chapter 3. Experimental Setup</b>	41
3.1 Experimental setup	41
3.2 The alternating-pump technique	46
References	58
<b>Chapter 4. Experimental Results</b>	60
4.1 Study of the thickness dependence of surface modes	60
4.1.1 $d$ -dependence of vibration frequencies	60
4.1.2 Vibration amplitudes of surface modes	64
4.2 Thickness profile measurement	67
4.3 $\Gamma$ -dependence of the surface-mode frequencies	70
4.4 Simultaneous extraction of $d$ and $\Gamma$	74
4.5 Study of the non-vibrational response	77
4.6 Laser damage to the Mo/Si multilayers	84
4.7 Summary	93
References	95
<b>Chapter 5. Numerical Simulations</b>	97
5.1 Overview	97
5.2 Initial stress generation	98
5.3 Sensitivity function	103

5.4	Calculation of $\Delta R$	105
5.4.1	Approach 1	105
5.4.2	Approach 2	109
	References	116
<b>Chapter 6. Conclusions</b>		<b>118</b>
6.1	Conclusions	118
6.1.1	Analytical theory of picosecond ultrasonics	118
6.1.2	Experimental setup - the alternating-pump technique	119
6.1.3	Experimental results	120
6.1.4	Numerical simulations	121
6.2	Future directions	122
6.2.1	Experimental setup	122
6.2.2	Experiments and applications	123
6.2.3	Numerical simulations	124
	References	127

# List of Figures

Fig. 1-1	Computational model for calculating multilayer reflectivity	3
Fig. 1-2	Reflectance response of typical Mo/Si and Mo/Be multilayer mirror coatings measured at $5^\circ$ from normal incidence	3
Fig. 1-3	Schematic diagram of the experiment for measuring the index of refraction in a transparent material	9
Fig. 2-1	The spatial dependence of the elastic strain at different times after the pump pulse is absorbed	18
Fig. 2-2	Geometry of an infinite 2-sublayer multilayer structure	22
Fig. 2-3	Calculated dispersion relation for longitudinal acoustic phonons in a Mo/Si multilayer with $d = 6.8$ nm and $\Gamma = 0.4$	26
Fig. 2-4	Spatial dependence of the stress and strain for the surface modes in the first gap and the second gap for a Mo/Si multilayer beginning with a Si layer ( $d = 70$ angstrom and $\Gamma = 0.4$ )	30
Fig. 2-5	Geometry of an $n$ -sublayer structure with $n_c$ cap layers	32
Fig. 2-6	Calculated frequencies for the lowest two surface modes as a function of $d_{ox}$ .	37
Fig. 3-1	Experimental setup	42
Fig. 3-2	The SHG autocorrelation traces of a laser pulse measured before and after the AO modulator	44

Fig. 3-3	The measured dependence of stage displacement on $V_{po}$	44
Fig. 3-4	(a) A measured trace $\Delta R(\tau)$ for a Mo/Si multilayer (b) A magnified view	47
Fig. 3-5	Timing of the pump and probe laser pulses in (a) the conventional scheme and (b) the alternating-pump scheme	49
Fig. 3-6	(a) $\Delta R(\tau)$ measured by conventional pump-probe technique (b) Same result obtained using the 2-pump scheme with $\tau_{AB} = 0.57$ ps (2nd-gap mode fully revealed) (c) 2-pump scheme with $\tau_{AB} = 1.14$ ps (2nd-gap mode cancelled)	50
Fig. 3-7	Noise power spectra of the lock-in amplifier output at a fixed time delay using the conventional scheme and the 2-pump scheme	55
Fig. 3-8	Comparison of the Fourier transform of $d\Delta R(\tau)/d\tau$ using (a) the conventional scheme, (b) the alternating-pump scheme with $\tau_{AB} = 0.57$ ps and (c) $\tau_{AB} = 1.14$ ps	56
Fig. 4-1	The derivative of $\Delta R(\tau)$ measured by the alternating-pump technique for $d =$ (a) 6.84 (b) 19.55 and (c) 32.56 nm	61
Fig. 4-2	Fourier transform of $d\Delta R(\tau)/d\tau$ for $d =$ (a) 6.84 (b) 19.55 and (c) 32.56 nm	62
Fig. 4-3	Top: The geometry of the graded sample. Bottom: peak frequency $\nu_2$ as a function of position	68
Fig. 4-4	The spectra (amplitude) of the surface modes at different $z$ positions on a graded sample	69

Fig. 4-5	(a) The vibration frequencies of the two surface modes vs. $\Gamma$ ( $d = 6.9\text{nm}$ ) (b) $g_{21}$ (the ratio $v_2/v_1$ ) as a function of $\Gamma$	72
Fig. 4-6	Comparison of the vibration spectra for $\Gamma = 0.4$ and $0.5$	73
Fig. 4-7	(a) (b) and (c) measured $v_1, v_2$ and $g_{21}$ for test wafers (d) Comparison of $d/d_{ref}$ extracted from $v_1$ and $v_2$ and $\lambda_{euv}/\lambda_{euv\_ref}$ measured by EUV reflectometry	76
Fig. 4-8	(a) Normalized $\Delta R(\tau)$ traces for $\Gamma = 0.3, 0.4,$ and $0.5$ (b) Same traces for thick Mo and Si films	80
Fig. 4-9	Logarithmic plot of $\Delta R(\tau)$ in a Mo film	83
Fig. 4-10	The echo time of the initial acoustic pulse for samples with various $\Gamma$	83
Fig. 4-11	(a) and (b): the vibration spectra of the 1 <sup>st</sup> - and 2 <sup>nd</sup> -gap mode after various amount of laser illumination time. (c): $v_1$ as a function of illumination time	85
Fig. 4-12	An areal EUV-beam scan of the sample with a $4 \times 4$ array of laser-damaged spots	87
Fig. 4-13	(a) The EUV reflectance spectra measured in laser-damaged and clear regions. (b) The corresponding vibration spectra	88
Fig. 4-14	The vibration spectra near $v_1$ for annealed and unannealed samples	90
Fig. 4-15	$v_1$ as a function of illumination time in samples with $d = 19.55$ and $32.56$ nm	92
Fig. 4-16	Frequency shifts induced by changes in acoustic impedance $Z$	92

Fig. 5-1	The geometry for an electromagnetic wave incident on a Mo/Si multilayer stack	99
Fig. 5-2	The spatial profile of optically deposited energy for a Mo/Si multilayer	102
Fig. 5-3	The sensitivity function $f(z)$ for various ratios of $\partial n / \partial \eta$ to $\partial \kappa / \partial \eta$ in Mo	104
Fig. 5-4	(a) $\Delta R(\tau)$ calculated using approach 1. (b) The corresponding vibration spectrum (semi-log). (c) The spectrum with $T_a = 15$ ps. (d) The spectrum for a multilayer begins with molybdenum	107
Fig. 5-5	The calculated spatiotemporal profile for temperature rise in a Mo/Si multilayer	110
Fig. 5-6	The $\Delta R(\tau)$ traces calculated via approach 2 for $t_1 =$ (a) 400, (b) 500, (c) 600, and (d) 700 fs , respectively	112
Fig. 5-7	The corresponding spectrum for the curve with $t_1 = 600$ fs	112
Fig. 5-8	The calculated spectra with various $\Gamma$ values	114



## List of Tables

Table 4-1	List of surface-mode frequencies in the 1 <sup>st</sup> , 2 <sup>nd</sup> , and 6 <sup>th</sup> gaps determined by theory and experiment	63
-----------	---	----

# Acknowledgements

I would like to express my sincerest thanks to my advisor, Professor Jeffrey Bokor for providing vision, advice, support, patience, and challenges throughout the most educational years of my life at Berkeley. This thesis would not be possible without his guidance. I also would like to express my deepest gratitude to Dr. Edward Budiarto and Dr. Seongtae Jeong. They were my colleagues, my friends, my mentors, and literally my trainer in the laboratory. It was an unforgettable experience to have an opportunity to work with them and learn from them for more than two years. Without the foundations they laid for the Ultrafast Laser Lab, I could not have finished my research in four years. I also want to thank the sponsors of my research project: the Semiconductor Research Corporation under contract 96-LC-460, DARPA Advanced Lithography Program under grant No. MDA972-97-0010, and AFOSR under grant No. F49620-97-1-0220.

Many people have also helped my progress immensely over the years. First and foremost I must thank Ri-An Zhao, my coworker in the lab, for his invaluable help and frequent discussions on my experimental problems. Next I would like to thank all of my colleagues in Professor Bokor's research group for their support and interaction. In particular, I want to mention Sang Hun Lee for discussions and group study for the prelim and many courses, and Dr. Chang Hyun Cho for his help in depositing Mo and a-Si films in the Microfabrication Laboratory. I also appreciate the great help from Patrick Kearny and Jim Underwood for providing the multilayer samples for my research, and from Marco Wedowsky for providing the EUV reflectometry data for cross correlation.

My fellowship provider, the Department of National Defense in Taiwan, not only supported me and my family financially throughout my graduate study but also spurred me to magically complete my program in four years. Without their rigid rule and constant reminders, it could easily dragged on for four more semesters.

On a more personal note, I must thank my family for support and understanding. Two great women in my life especially deserve my deepest thankfulness: my mother and my wife. And of course, my father, who gave me the momentum to pursue this degree. I cannot say enough words to thank them for everything they've done.

The help from my friends has also been tremendous. I thank Hung Pham, Janet Hoang and her family wholeheartedly for welcoming me to US and helping me and my wife settle down in Berkeley four years ago. Carole Jennings offered her valuable time to help me with my spoken English. The numerous brothers and sisters in S.M. International Association offered me unconditional love, generosity and friendship without limits, and made me feel at home in a strange land. Leina Leong, Khoa Luong, Betty Luong, Tho Nguyen, Tammy Bui, Jim Su,.... — you guys will be greatly missed!

There are so many people to thank, and I finally realize that the one I should really pay my homage to is the Supreme Lord, who forever loves me through my mother, through my wife, and through everyone I come across in the journey of life; who enlightens me when I see no light and inspires me when I see no hope; who clears the obstacles, shoulders the burdens and smoothes the way for me. Meditation in my Lord calms my mind, relieves my stress and recharges my spirit everyday. By praising thy name, I sincerely thank the numerous other friends who are the physical manifestations of thee.

# Chapter 1. Introduction

Extreme ultraviolet lithography (EUVL) is a promising next-generation-lithography (NGL) technology for the mass production of integrated circuits with design rules below 0.1  $\mu\text{m}$ . By using short wavelength (10-15 nm) and low numerical aperture (NA) optics (e.g.,  $\text{NA} < 0.1$ ), both high resolution and an acceptable depth of focus (e.g.,  $\pm 0.5 \mu\text{m}$ ) can be achieved. According to the 1999 International Technology Roadmap for Semiconductors (ITRS), 157-nm wavelength “deep ultraviolet” (DUV) sources with high NA optics and resolution enhancement technologies (RET) is becoming a preferred option for printing circuits with feature sizes of 100 nm (and maybe below), and most of the EUVL researchers are targeting for the introduction node at 70- or 50-nm feature size. Multilayer mirror coatings which reflect extreme ultraviolet (EUV) radiation are a key enabling technology for EUVL. In fact, it is the recent advances of multilayer mirror technology that spurred the great interest in projection lithography at EUV wavelengths. However, in order for a production EUVL system to be practical in terms of performance and throughput, the multilayer mirrors must meet many stringent requirements, which pose daunting challenges on the state-of-the-art technologies in mirror fabrication, thin film deposition, and optics design. To characterize the quality of multilayer mirrors is another big technical challenge: the accuracy and precision requirements on the characterization tools are difficult to achieve. Many novel techniques have thus been developed in the past few years to deal with various aspects of this big issue. In this dissertation, I will limit my scope only on the characterization of multilayer coatings using a nondestructive picosecond ultrasonic technique.

## 1.1 Multilayer interference coatings

Multilayer interference coatings, more often simply referred to as multilayers, are formed by depositing alternating layers of two materials of different refractive indices. In the visible, non-absorbing dielectric multilayer films have been extensively used in many optical components such as high reflection (HR), antireflection (AR), and partial reflection (beam splitters) mirror coatings, dichroic coatings, and broad or narrow band-pass filters. Their application has long been extended to IR, UV, and more recently to EUV, soft x-ray, and even x-ray wavelengths. However, at wavelengths shorter than  $\sim 120$  nm, the optimal multilayer reflectance is not comparable to that in the visible (e.g.  $>99\%$ ) due to the unavoidable absorption problem in all materials. For example, the peak reflectance for a soft x-ray W/C multilayer at  $8.34 \text{ \AA}$  is less than 70% at a grazing incidence angle of  $\sim 11^\circ$ [1.1]

For EUV, soft x-ray, and x-ray wavelengths, typically the two materials are of alternating high and low atomic number ( $Z$ ) so as to maximize the difference in electron density (and thus, in refractive index)[1.2]. Being largely amorphous or polycrystalline in nature, multilayer coatings have the great advantage of being adaptable to curved surfaces, leading them to convenient use as reflective optics in EUV lithography, microscopes, telescopes, and other applications. Analogous to Bragg diffraction in natural crystals, high reflectance (or diffraction) peaks can be achieved with artificial multilayer coatings, provided Bragg's law is satisfied[1.2]:

$$m \lambda = 2 d \sin \theta \quad (1.1)$$

where  $m = 1, 2, 3, \dots$ ,  $\lambda$  is the wavelength,  $d$  is the periodicity, and  $\theta$  is the angle between

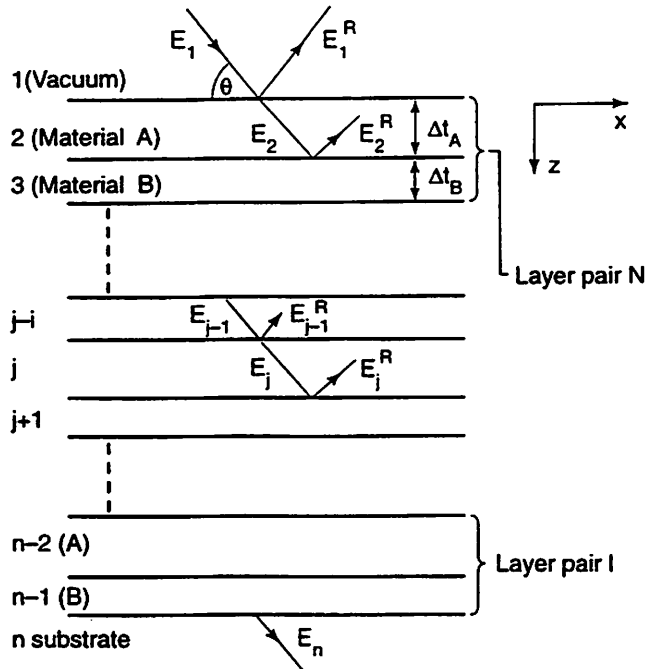


Figure 1-1 Computational model for calculating multilayer reflectivity, shown here as  $N$  bilayer pairs of two materials, A and B, of thickness  $\Delta t_A$  and  $\Delta t_B$ , where the multilayer period is  $d = \Delta t_A + \Delta t_B$  (From J.H. Underwood *et al.*, Ref.[1.3])

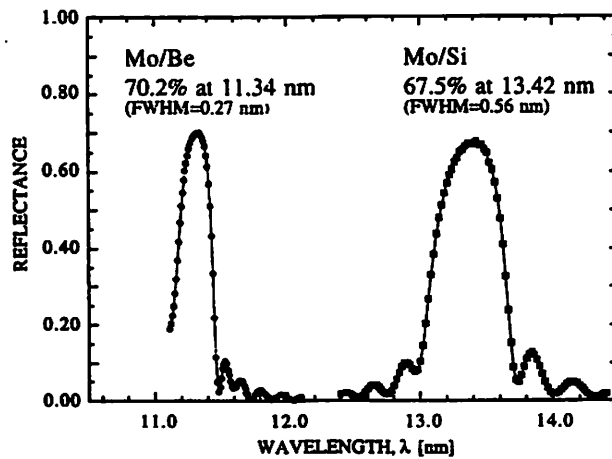


Figure 1-2 Reflectance response of typical Mo/Si and Mo/Be multilayer mirror coatings measured at  $5^\circ$  from normal incidence. Peak reflectance of 70.2% and 67.5% are routinely achieved for Mo/Be and Mo/Si, respectively. (From Ref. [1.5])

the incidence beam and the multilayer surface. For instance, the coating periodicity ( $d$ -spacing) required for a Mo/Si multilayer reflecting 13.4 nm radiation at normal incidence will be about 6.7 nm.

A more rigorous computational model for calculating multilayer reflectance is proposed by Underwood *et al.*[1.3]. The calculation is performed for incident radiation at an angle  $\theta$  from the surface, applying the boundary conditions that tangential components of electric and magnetic fields be continuous at each interface (Fig. 1-1). Each material is characterized by a refractive index  $n$ :

$$n = 1 - \delta + i\beta = 1 - \frac{n_a r_e \lambda^2}{2\pi} (f_0' - i f_0'') \quad (1.2)$$

where  $n_a$  is the density in atoms per unit volume,  $r_e$  is the classical electron radius, and  $f_0', f_0''$  are the real and imaginary parts of the complex atomic scattering function, which are roughly proportional to  $Z$ [1.2]. For the simplest case of normal incidence *at a single interface* between a high- $Z$  and a low- $Z$  layer, the reflectance is given by:

$$R_{LH} = \left| \frac{n_H - n_L}{n_H + n_L} \right|^2 = \frac{(\delta_H - \delta_L)^2 + (\beta_H - \beta_L)^2}{(2 - \delta_H - \delta_L)^2 + (\beta_H + \beta_L)^2} \approx \frac{(\delta_H - \delta_L)^2 + (\beta_H - \beta_L)^2}{4} \quad (1.3)$$

Therefore, the optical constants of the low- $Z$  material,  $\delta_L$  and  $\beta_L$  should be as small as possible to provide the greatest refractive index contrast at the interfaces. On the other hand,  $\delta_H$  and  $\beta_H$  of the high- $Z$  material should be as big as possible to have higher reflectance at a single interface. To go a step further from a single interface to the multilayer structure, a transfer-matrix method in classic electromagnetics is used[1.3] (to be introduced in Chapter 5).

The imaginary part of refractive index represents absorption in a material. So a larger  $\beta_H$ , although increases  $R_{LH}$ , also means a higher absorption and thus a shorter

penetration depth into the multilayer, which reduces the overall reflectance. The tradeoff is then to obtain a sufficiently high  $R_{LH}$ , through refractive index contrast at the interfaces, while minimizing the absorption by choosing a lower  $\beta_H$  or alternatively, by reducing the thickness of the high-Z material. A well-known design parameter in maximizing the peak reflectance is the ratio of high-Z material thickness to bilayer period,  $\Gamma$ [1.2], i.e.

$$\Gamma = \frac{\Delta t_H}{\Delta t_H + \Delta t_L} = \frac{\Delta t_H}{d} \quad (1.4)$$

where  $\Delta t_H$  and  $\Delta t_L$  are the thicknesses of the high- and low-Z materials. The low-Z material acts like a “spacer” since it has a smaller absorption. Therefore, to optimize the overall reflectance, it is better to make the low-Z layers somewhat thicker, to an extent that the phases of reflected beams do not deviate too much from the constructive-interference condition. Vinogradov *et al.*[1.4] have studied this and found an optimized value  $\Gamma_{opt}$ , given by

$$\tan(\pi\Gamma_{opt}) = \pi \left[ \Gamma_{opt} + \frac{\beta_L}{\beta_H - \beta_L} \right] \quad (1.5)$$

For Mo/Si and Mo/Be multilayers, this  $\Gamma_{opt}$  is around 0.4. The theoretical peak reflectance of an ideal multilayer is ~75% for the Mo/Si multilayer and ~80% for the Mo/Be multilayer.

Figure 1-2 is an example of the measured reflectance versus wavelength curves of the Mo/Si and Mo/Be multilayer mirrors at  $5^\circ$  from normal incidence[1.5]. The period thickness  $d$  is 6.89 nm for Mo/Si, and 5.74 nm for Mo/Be. The reflectance curve of the Mo/Si multilayer reaches a peak value of 67.5% at 13.42 nm while the Mo/Be multilayer



has a peak reflectance of 70.2% at 11.34 nm. These values of peak reflectance are somewhat lower than the theoretical prediction due to the existence of diffuse interlayers at the layer boundaries and a contamination or corrosion layer on the surface[1.5]. The spectral bandwidth measured at full width at half-maximum (FWHM), is 0.56 nm and 0.27 nm for the Mo/Si and Mo/Be multilayer, respectively. The Mo/Si multilayer has a Si layer as the top-most layer on the surface while the Mo/Be multilayer has a Be top layer. This is because Mo strongly oxidizes in the air and forms various compounds which severely degrade the reflectance[1.6]. Finally, multilayer reflectance also strongly depends on the high-spatial-frequency roughness of the optical substrate. Advanced EUVL system designs require aspheric optical substrates with extremely tight specifications on aspheric figure and both mid- and high- spatial frequency roughness[1.5].

Since these coatings have fairly narrow bandpass, and typically seven to eight optics are used for a prototype projection lithography system[1.7], the wavelength of the peak reflectance for each coating must be aligned to within 0.05 nm to preserve at least 90% of the optimum throughput[1.5]. For example, this requirement sets the run-to-run deposition reproducibility of Mo/Si bilayer thickness to within 0.025 nm (0.36%). In addition, to minimize the phase errors that affect the imaging performance, the deviation from the designed coating thickness profile across an optic must be less than 0.1%[1.8]. In order to meet these stringent requirements, a good characterization technique is necessary to measure the physical period,  $d$  and the  $\Gamma$  ratio (the thickness ratio of Mo layer to the bilayer), and to evaluate the uniformity and repeatability of the deposition process. Grazing incidence x-ray diffraction offers high accuracy in measuring  $d$ .

However, the small grazing angle requirement, and the relatively large x-ray spot size (typically  $\sim 3$  mm) greatly limit its usefulness and preclude its application in measuring curved optics and in evaluating coating uniformity. Another frequently used diagnostic tool, at-wavelength reflectance measurement, has the advantage of small spot size, near normal incidence, and good accuracy for  $d$  measurement. However, the high cost and limited access to EUV sources make this tool unavailable to many researchers. In addition, neither of these two techniques can separately measure  $\Gamma$  accurately. Consequently, it is very desirable to develop a nondestructive characterization technique which is more available and can overcome these technical problems. This is the motivation for me to study the possibility of using the ultrasonic technique as a nondestructive tool to characterize EUVL multilayers.

## **1.2 Picosecond ultrasonics**

After the invention of the first laser in 1960, a considerable amount of pioneering work has been devoted to ultrasound generation by lasers[1.10]-[1.14]. Materials with high optical absorption can be used to transfer energy from an optical beam to acoustic waves – the photoacoustic effect. The change in temperature and the thermal expansion which accompanies the absorption of optical energy generates acoustic waves at frequencies corresponding to the amplitude modulation of the optical beam. In 1963, shortly after the successful operation of the first ruby laser, R.M. White[1.9] demonstrated, for the first time, the generation of acoustic pulses by laser irradiation on a metal surface using a pulsed ruby laser. Progress in this area was closely related to the development of the laser sources, and several techniques have been proposed, which

mainly differ by the characteristics of the laser sources. Most of the early works employed Q-switched lasers with pulsewidths in the tens of nanoseconds regime, which can only excite ultrasonic waves in the 10 MHz frequency range. This sets a limit in some applications, particularly when a high spatial resolution is required. For example, the corresponding acoustic wavelength in a solid is greater than 100  $\mu\text{m}$ . It has to be further reduced and hence, shorter optical pulses are necessary, if a better resolution is desired.

In 1978, Wickramasinghe *et al.*[1.14] used a Nd:glass mode-locked laser to generate a 840 MHz ultrasound in 25- $\mu\text{m}$ -thick aluminum sheets. This is a remarkable result since it brings the frequency of ultrasound generated by laser near the GHz range. However, this frequency is not high enough for applications in probing submicron structures. With the advances in laser mode-locking techniques in the last two decades, reliable ultrafast lasers with femtosecond pulsewidths become available and easy-to-use. These new laser sources enabled researchers to generate ultrasounds in the THz regime and created a new research field - Picosecond Ultrasonics, first named by Grahn *et al.* in 1988[1.15]. Unlike conventional laser ultrasonic techniques, which generally use interferometric schemes or piezo-electric transducers as detectors, the picosecond ultrasonic technique is an optical pump and probe technique, which monitors the elastic behavior of the sample with a time-delayed optical probe pulse through the changes of the optical reflectance  $\Delta R(t)$  induced by the pump pulse. In 1986, Thomsen *et al.*[1.16] observed successive echoes of laser-induced acoustic pulses in a 220-nm film of a-As<sub>2</sub>Te<sub>3</sub>. These acoustic pulses were excited near the free surface of the film with a mode-locked dye laser (pulsewidth = 200 fs), and their width is less than 50 ps. As a first application, they

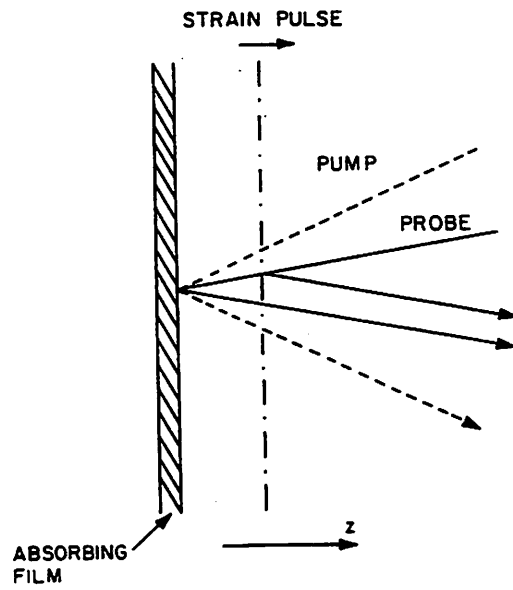


Figure 1-3 Schematic diagram of the experiment for measuring the index of refraction in a transparent material. (From C. Thomsen *et al.*, Ref.[1.19])

determined the sound velocity of the material by measuring the propagation time between echoes[1.15]-[1.17]. Alternatively, knowing the sound velocity, the film thickness can be determined from the same measurement. Another piece of information obtained in this experiment is the attenuation strength of longitudinal-acoustic phonons within the ultrasonic frequency bandwidth[1.18]. An interesting application of this technique is to measure the refractive index of a transparent material[1.15]. The probe light wave reflected from the surface interferes constructively or destructively with the wave reflected at the propagating strain(acoustic) pulse plane, depending on the optical path difference between the two waves (see Fig. 1-3) . Thus, the trace of  $\Delta R(t)$  shows an oscillatory behavior with a period  $T$  given by [1.19]

$$T = \lambda / 2 v n \cos \theta \quad (1.6)$$

where  $n$  and  $v$  are, respectively, the refractive index and the sound velocity of the transparent material.  $\theta$  is the angle between the light wave vector (in the medium) and the normal to the surface.

The echoes can betray many other characteristics of the film stack. For instance, when a sound pulse reflects from a rough boundary, it will broaden in space and time. Therefore, analyzing the echo's shape can indicate the roughness of a surface. In addition, from the intensity of the echoes, it is possible to characterize the quality of interfacial bonding in adjacent films[1.20]. Detection of  $\text{TiSi}_2$  phase transformation using picosecond ultrasonics has also been demonstrated[1.21] by analyzing the change in the echo pattern during annealing.

Superlattice and multilayer structures have unique vibrational properties that distinguish them from bulk materials. The differences in behavior are related to the

folding and opening of gaps on the phonon dispersion relation curves, due to the periodic boundary condition imposed by the structure. Sharp resonant modes existing within the frequency band gaps have been observed in many superlattice and multilayer nanostructures[1.22]-[1.29]. These modes are non-propagating, persistent, and localized near the free surface of a film stack, hence the name “localized surface modes”. The detailed theory of these surface modes will be discussed in the next chapter. It can be shown that[1.29], if two surface modes can be simultaneously detected, the two key parameters of a multilayer,  $d$  and  $\Gamma$ , can be extracted from their vibration frequencies. In chapter 4, I will describe the details of our experimental results on EUV Mo/Si multilayers and the procedures to extract useful information from the data.

## References

- [1.1] J.H. Underwood, *Optics News*, **12**, 20 (OSA, Washington, DC, March 1986).
- [1.2] D.T. Attwood, *Soft X-Rays and Extreme Ultraviolet Radiation: Principles and Applications*, Cambridge University Press, 1999.
- [1.3] J.H. Underwood and T.W. Barbee, Jr., *Applied Optics*, **20**, 3027 (1981).
- [1.4] A.V. Vinogradov and B.Y. Zeldovich, *Applied Optics*, **16**, 89 (1977).
- [1.5] C. Montcalm, S. Bajt, P.B. Mirkarimi, E. Spiller, F.J. Weber, and J.A. Folta, *Proceedings of SPIE on Emerging Lithographic Technologies II*, vol.3331, p.42, 1998.
- [1.6] J.H. Underwood, E.M. Gullikson, and K. Nguyen, *Applied Optics*, **32**, 6985 (1993).
- [1.7] D.W. Sweeney, R.M. Hudyma, H.N. Chapman and D.R. Shafer, *Proceedings of SPIE on Emerging Lithographic Technologies II*, vol.3331, p.2, 1998.
- [1.8] J.A. Folta, S. Bajt, T.W. Barbee, Jr., R.F. Grabner, P.B. Mirkarimi, T. Nguyen, M.A. Schmidt, E. Spiller, C.C. Walton, M. Wedowski, and C. Montcalm, *Proceedings of SPIE on Emerging Lithographic Technologies III*, vol. 3676, p.702, 1999.
- [1.9] R.M. White, *Journal of Applied Physics*, **34**, 3559 (1963).
- [1.10] C.B. Scruby, R.J. Dewhurst, D.A. Hutchins and S.B. Palmer, *Journal of Applied Physics*, **51**, 6210 (1980).
- [1.11] R.J. Dewhurst and W.S.A.R. Al'Rubai, *Ultrasonics*, **27**, 262 (1989).
- [1.12] L.F.R. Rose, *Journal of the Acoustic Society of America*, **75**, 723 (1975).
- [1.13] C.A. Calder and W.W. Wilcox, *Review of Scientific Instruments*, **45**, 1557 (1974).
- [1.14] H.K. Wickramasinghe, R.C. Bray, V. Jipson, C.F. Quate and J.R.Salcedo, *Applied Physics Letters*, **33**, 923 (1978).

- [1.15] H.T. Grahn, D.A. Young, H.J. Maris, J. Tauc, J.M. Hong, and T.P. Smith III, *Applied Physics Letters*, **53**, 2023 (1988).
- [1.16] C. Thomsen, H.T. Grahn, H.J. Maris, and J. Tauc, *Physical Review*, **B 34**, 4129 (1986).
- [1.17] H.T. Grahn, H.J. Maris, J. Tauc, and K.S. Hatton, *Applied Physics Letters*, **53**, 2281 (1988).
- [1.18] T.C. Zhu, H.J. Maris, and J. Tauc, *Physical Review*, **B 44**, 4281 (1991).
- [1.19] C. Thomsen, H.T. Grahn, H.J. Maris, and J. Tauc, *Optics Communications*, **60**, 55 (1986).
- [1.20] G. Tas, J.J. Loomis, H.J. Maris, A.A. Bailes III, and J. Tauc, *Applied Physics Letters*, **72**, 2235 (1998).
- [1.21] H.-N. Lin, R.J. Stoner, H.J. Maris, J.M.E. Harper, C. Cabral, Jr., J.-M. Halbout, and G.W. Rubloff, *Applied Physics Letters*, **61**, 2700 (1992).
- [1.22] H.T. Grahn, H.J. Maris, J. Tauc, and B. Abeles, *Physics Review*, **B 38**, 6066 (1986).
- [1.23] W. Chen, Y. Lu, H.J. Maris and G. Xiao, *Physical Review*, **B 50**, 14506 (1994).
- [1.24] B.Perrin, B.Bonello, J.C.Jeannet and E.Romatet, *Physica*, **B 219&220**, 681 (1996).
- [1.25] B.Bonello, B.Perrin, E.Romatet and J.C.Jeannet, *Ultrasonics*, **35**, 223 (1997).
- [1.26] H.T.Grahn, H.J.Maris, and J.Tauc, *IEEE J. Quantum Electron.*, **25**, 2562 (1989).
- [1.27] N-W.Pu, S.Jeong, R-A.Zhao, and J.Bokor, *Applied Physics Letters.*, **74**, 320 (1999).
- [1.28] N-W.Pu, S.Jeong, R-A.Zhao, and J.Bokor, *Proceedings of SPIE on Emerging Lithographic Technologies III*, vol.**3676**, p.627, 1999.



[1.29] N-W.Pu, J. Bokor, S. Jeong, and R-A. Zhao, *Journal of Vacuum Science and Technology*, **B 17**, 3014 (1999).

# Chapter 2. Theory of Picosecond Ultrasonics

In this chapter, the theory of picosecond ultrasonics is reviewed. Acoustic waves excited by ultrafast laser pulses, in both bulk materials and multilayers, are discussed. An analytical model to determine the vibration frequencies of the localized surface modes in a 2-sublayer semi-infinite multilayer will be described, and generalized further to include capped n-sublayer structures.

## 2.1 Acoustic pulse generation and detection in a bulk material

### 2.1.1 Generation of acoustic pulses

When a light pulse is incident on the surface of an absorbing material, it is the electrons that are initially excited. While diffusing into the sample, these “hot electrons” lose their excess energy to the lattice via electron-phonon interaction in 0.1 to 1 ps [2.1]-[2.2], and set up a local thermal stress field. This field is determined by the initial temperature distribution. The relaxation of this stress launches strain pulses, viz. ultrasound, that propagate through the structure. Neglecting the electron diffusion which takes place in a few hundred femtoseconds[2.3][2.10] and assuming a spatial dependence of the energy density deposited onto the sample of the form  $e^{-z/\zeta} I(x, y, \tau)$ , the temperature change  $\Delta T$  is given by:

$$\Delta T(x, y, z) dx dy = \frac{1}{\rho C \zeta} e^{-z/\zeta} dx dy \int_0^{t_p} d\tau I(x, y, \tau) \quad (2.1)$$

where  $\zeta$ ,  $C$  and  $\rho$  are respectively the optical absorption length, the specific heat and the

density of the sample.  $\tau$  is time and  $t_p$  is the laser pulse duration. Here the surface of the sample defines the  $x$ - $y$  plane. In most metals, for visible and near-infrared light, the absorption length  $\zeta$  is in the range of 10 to 30 nm. Given a focal spot size on the order of one micron or larger, the lateral dimensions of the thermoelastic source are much larger than its extent in the  $z$  direction. As a consequence of this spatial dependence, the propagation of strain waves can be treated as a 1-D problem (only  $z$ -dependence), and the only component of the strain tensor to be considered is  $\eta_{33}$ . Note that the energy density  $I(x,y,\tau)$  induces a small temperature gradient in  $(x,y)$  plane and hence, strain with components parallel to the surface is not strictly zero, but can be neglected with a good accuracy. Neglecting the heat diffusion and elastic relaxation during the ultrashort time of light pulses, Eq. (2.1) can be integrated over  $x$  and  $y$  coordinates to yield a 1-D initial temperature distribution:

$$\Delta T(z, \tau = 0) = \frac{(1-R)}{\rho C A \zeta} Q \exp(-z/\zeta) \quad (2.2)$$

where  $R$  is the optical reflectance of the sample,  $A$  is the laser spot area, and  $Q$  is the total optical pulse energy. An initial elastic stress is set up which is described by an elastic stress tensor with components

$$\begin{aligned} \sigma_{ij}(z, \tau = 0) &= -3B\beta\Delta T(z, \tau = 0)\delta_{ij} \\ &= -3B\beta\frac{(1-R)}{\rho C A \zeta} Q \exp(-z/\zeta)\delta_{ij} \end{aligned} \quad (2.3)$$

where  $\beta$  is the thermal expansion coefficient and  $B$  is the bulk modulus. Immediately after the light is absorbed the strain is zero. However the stress is inhomogeneous, and consequently, the material begins to relax. It is a straightforward initial condition

problem in elasticity to calculate how the material moves. Since the only nonzero component of the elastic strain tensor is  $\eta_{33}$  we have to solve the equations of elasticity in the form[2.4]:

$$\sigma_{33}(z, \tau) = 3 \frac{1-\mu}{1+\mu} B \eta_{33}(z, \tau) - 3B\beta\Delta T(z, \tau), \quad (2.4)$$

$$\rho \frac{\partial^2 u_3}{\partial \tau^2} = \frac{\partial \sigma_{33}}{\partial z}, \quad (2.5)$$

$$\text{and} \quad \eta_{33}(z, \tau) = \frac{\partial u_3}{\partial z} \quad (2.6)$$

where  $\mu$  is the Poisson's ratio,  $u_3$  is the displacement in the  $z$  direction, and  $\rho$  is the density. These equations have to be solved with the boundary condition that  $\sigma_{33}$  must be always zero at the free surface  $z = 0$ . The solution has the form[2.4]:

$$\eta_{33}(z, \tau) = \frac{\beta(1-R)Q}{\rho CA \zeta} \left( \frac{1-\mu}{1+\mu} \right) \left[ e^{-z/\zeta} \left( 1 - \frac{1}{2} e^{-c\tau/\zeta} \right) - \frac{1}{2} e^{-|z-c\tau|/\zeta} \text{sgn}(z - c\tau) \right] \quad (2.7)$$

where  $c$  is the longitudinal sound velocity given by

$$c^2 = 3 \left( \frac{1-\mu}{1+\mu} \right) \frac{B}{\rho} \quad (2.8)$$

The strain given by Eq. (2.7) is shown in Fig. 2-1. It consists of two parts: a bipolar strain pulse propagating within the sample at a sound velocity  $c$ , superposed on a smooth, slowly-varying background. The bipolar shape of the propagating pulse is a result of superposition of a forward-propagating wave and a backward propagating wave reflected at  $z = 0$ . Two interesting features can be seen from Eq. (2.7): First, the propagating bipolar pulse extends over a width of about  $2\zeta$ . Thus, the spatial resolution of the pulse echo technique for thickness measurement is in the nm range. The second feature of this

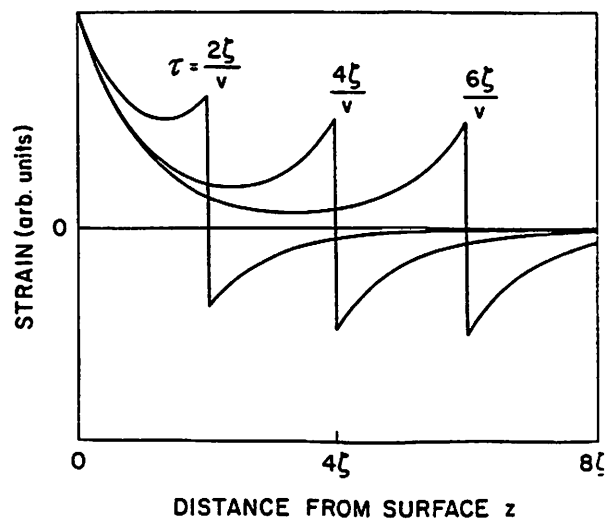


Figure 2-1 The spatial dependence of the elastic strain at different times after the pump pulse is absorbed.

strain pulse is its broad spectrum. The Fourier transform of  $\eta_{33}$  is proportional to :

$$\frac{2\pi\nu}{4\pi^2\nu^2 + (c/\zeta)^2} \quad (2.9)$$

which peaks at a frequency  $\nu_p = c/2\pi\zeta$ , with a FWHM bandwidth of  $2\sqrt{3}\nu_p$ . In aluminum, for example, this spectrum exhibits a maximum at  $\nu_p \sim 150$  GHz, and extends up to about 500 GHz. The strain pulse propagates in the film and is partially reflected at the film/substrate interface and at the free surface (film/air interface), giving rise to successive echoes. The reflection coefficient  $r$  is given by

$$r = \frac{Z_2 - Z_1}{Z_2 + Z_1} \quad (2.10)$$

where  $Z_1$  and  $Z_2$  are the acoustical impedances (product of the sound velocity  $c$  and the density  $\rho$ ) of the film and the substrate (or air), respectively.

### 2.1.2 Detection of acoustic pulses

Elastic strain slightly modifies the optical constants  $n$  and  $\kappa$  (the real and imaginary part of the complex refractive index) of the material, and thereby induce a change in the optical reflectance  $R$ . This provides a means to detect the strain pulses. By monitoring the reflected intensity of a “probe” light pulse, the reflectance change  $\Delta R$  associated with the elastic response generated by a “pump” light pulse is detected. Varying the relative delay time between the pump and the probe, one can obtain the temporal trace of  $\Delta R(\tau)$ , which shows the dynamic evolution of the acoustic response.

The measured change in reflectance can be expressed as

$$\Delta R(\tau) = \int_0^\infty f(z)\eta(z, \tau)dz \quad (2.11)$$

where the so-called “sensitivity function”  $f(z)$ [2.4] determines how strain at different

depths below the surface contributes to the change in the reflectance. It is straightforward to calculate  $f(z)$  from the optical properties of the sample (see Chapter 5 for details). The general form of  $f(z)$  is an exponentially damped oscillation with a nonzero phase at  $z = 0$ . The periodicity of  $f$  is half the wavelength of the light in the material. The range of  $f(z)$  is roughly equal to the optical absorption length  $\zeta$ . By combining Eq. (2.11) and the result (2.7) for the strain, one can calculate the expected shape of the echoes observed on  $\Delta R(\tau)$ . In Ref. [2.4], the calculation comes out in very good agreement with the measured trace on a a-As<sub>2</sub>Te<sub>3</sub> film. By fitting the measured  $\Delta R(\tau)$  to theory, Maris *et al.* claimed that the accuracy in thickness measurement can be less than an angstrom – far shorter than the ultrasound wavelength[2.5].

By comparison of the spectral content of two successive echoes, the ultrasonic attenuation in a material can be determined. The attenuation coefficient  $\alpha(\nu)$  is related to the Fourier transform of the reflectivity changes produced by the  $n$ th echo  $\Delta R^{(n)}(\nu)$  by

$$\alpha(\nu) = \ln \left| \frac{r \Delta R^{(n)}(\nu)}{\Delta R^{(n+1)}(\nu)} \right| / 2d \quad (2.12)$$

where  $d$  is the film thickness and  $r$  is given by (2.10). Owing to the wide ultrasonic spectrum, the ultrasonic attenuation over a broad frequency range can be obtained in a single measurement.

This technique can be applied to transparent materials as well. In a non-absorbing material, a metallic layer acting as a transducer is deposited onto the sample surface to generate acoustic pulses. When the thickness of this metal layer  $d_m$  is less than the absorption length, both shape and spectrum of the acoustic pulse are controlled by  $d_m$  instead of  $\zeta$ , and the spectral content is shifted towards higher frequencies, which is

advantageous in some applications.

It should be noticed that the description of the generation process given in this section is over-simplified. A more complete picture should include the following effects:

(1) The hot electrons also make a contribution to the initial elastic stress. The contribution is comparable in magnitude to the thermal expansion effect we have considered, but may have the opposite sign in some materials[2.4]. In addition, as the hot electrons relax this electronic stress changes with time.

(2) The spatial form of the strain pulse can be significantly modified by thermal diffusion. Initially, light energy is deposited over a distance  $\zeta$ . The time it takes the strain pulse to leave this region is  $\zeta / c$ . If the thermal diffusivity is  $D$ , in this time heat diffuses a distance  $\zeta^* = (D\zeta/c)^{1/2}$ . Thus, diffusion is important as a mechanism to change the pulse shape if  $\zeta^*$  is comparable to  $\zeta$ , which is usually true in metals.

(3) The hot electrons can also diffuse a significant distance before they lose their energy to the phonons. This effect is enhanced as the energy of the photons in the light pulse is increased, because this gives electrons a larger kinetic energy.

## **2.2 Theory of multilayer eigenmodes**

The periodic modulation of the acoustic properties in a superlattice or multilayer leads to profound modifications in the propagation of acoustic phonons. The dispersion curve is folded into a mini-Brillouin zone of dimension  $2\pi / d$ , where  $d$  is the modulation period, and gaps open at the zone boundaries and the zone center[2.6]-[2.7]. Direct evidence of the folding is found in the now routine observation of additional lines in the low-frequency Raman spectra[2.8]. Gaps in the phonon dispersion define frequencies for



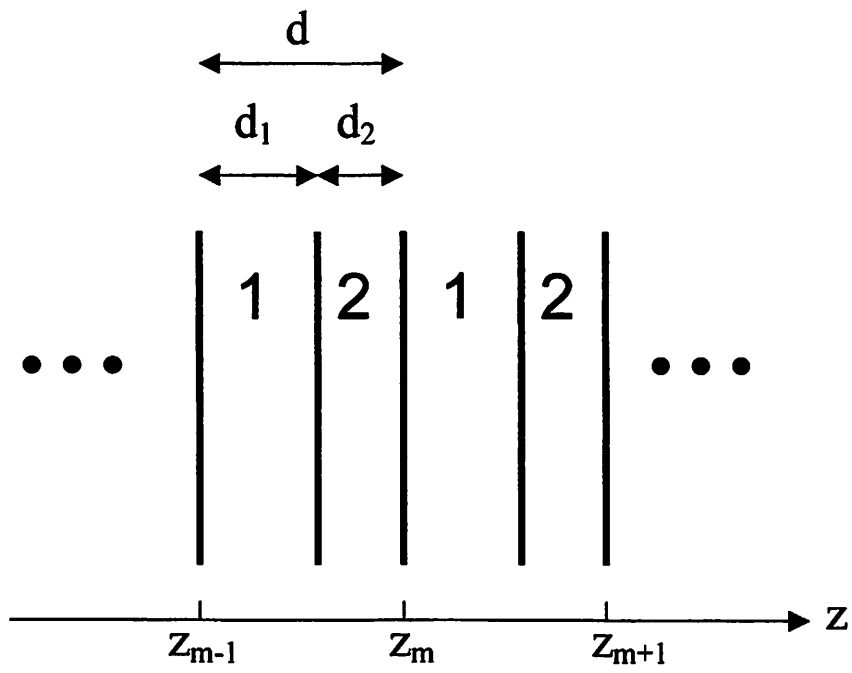


Figure 2-2 Geometry of an infinite 2-sublayer multilayer structure.

which propagating modes do not exist , but as usual there remains the possibility of exciting localized modes associated with the free surface, or with other local disturbances from periodicity. The frequency, and even the existence, of such an in-gap mode depends on the surface conditions. These modes have been predicted to occur[2.9]-[2.10], and evidences for them are found in time-resolved reflectivity with picosecond resolution[2.11]-[2.18] and in Raman scattering spectra[2.8]. In this section we study the normal modes (both bulk and surface modes) of a multilayer structure.

### 2.2.1 Bulk modes in an infinite multilayer

Consider a multilayer structure made up of infinite alternating layers of thicknesses  $d_1$  and  $d_2$  , densities  $\rho_1$  and  $\rho_2$ , and sound velocities  $c_1$  and  $c_2$ . The repeat distance  $d$  equals  $d_1 + d_2$ . The geometry is shown in Fig. 2-2. The equation of elasticity is

$$\rho \frac{\partial^2 u}{\partial \tau^2} = \frac{\partial \sigma}{\partial z} \quad (2.13)$$

where  $u$  is the displacement in the  $z$  direction, and  $\sigma$  is the  $zz$  component of the elastic stress tensor which is related to  $u$  by

$$\sigma (z, \tau) = \rho c^2 \eta (z, \tau) \quad (2.14)$$

where  $\eta = \partial u / \partial z$  is the  $zz$  component of the elastic strain tensor, and the values of the sound velocity  $c$  and the density  $\rho$  to be used depend on the particular layer. We look for a solution in the form

$$u(z, \tau) = w(z)e^{-i\omega\tau} \quad (2.15)$$

Let the  $m$ th bilayer of the superlattice begin at  $z = z_m$ . Then we can write the general solution of the wave equation in the sublayer composed of material 1 as

$$w(z) = A_{m,1} \sin[k_1(z - z_m)] + B_{m,1} \cos[k_1(z - z_m)] , \quad (2.16)$$

and in sublayer 2 as

$$w(z) = A_{m,2} \sin[k_2(z - z_m - d_1)] + B_{m,2} \cos[k_2(z - z_m - d_1)] \quad (2.17)$$

where  $k_1 = \omega / c_1$  and  $k_2 = \omega / c_2$ .  $A_{m,1}$ ,  $A_{m,2}$ ,  $B_{m,1}$ ,  $B_{m,2}$  are constant amplitudes. The boundary conditions are that  $u$  and  $\sigma$  must be continuous at any interface. These conditions related  $(A_{m,2}, B_{m,2})$  to  $(A_{m,1}, B_{m,1})$ ,  $(A_{m+1,1}, B_{m+1,1})$  to  $(A_{m,2}, B_{m,2})$ , and so on.

(i) Relation between  $(A_{m,2}, B_{m,2})$  and  $(A_{m,1}, B_{m,1})$

$$\begin{pmatrix} A_{m,2} \\ B_{m,2} \end{pmatrix} = M_{1 \rightarrow 2} \begin{pmatrix} A_{m,1} \\ B_{m,1} \end{pmatrix} \quad (2.18)$$

$$\text{The sublayer transfer matrix } M_{1 \rightarrow 2} = \begin{pmatrix} p_{12} \cos k_1 d_1 & -p_{12} \sin k_1 d_1 \\ \sin k_1 d_1 & \cos k_1 d_1 \end{pmatrix} \quad (2.19)$$

where  $p_{12} = Z_1 / Z_2$  or  $c_1 \rho_1 / c_2 \rho_2$ .

(ii) Relation between  $(A_{m+1,1}, B_{m+1,1})$  and  $(A_{m,2}, B_{m,2})$

$$\begin{pmatrix} A_{m+1,1} \\ B_{m+1,1} \end{pmatrix} = M_{2 \rightarrow 1} \begin{pmatrix} A_{m,2} \\ B_{m,2} \end{pmatrix} \quad (2.20)$$

$$\text{The sublayer transfer matrix } M_{2 \rightarrow 1} = \begin{pmatrix} p_{21} \cos k_2 d_2 & -p_{21} \sin k_2 d_2 \\ \sin k_2 d_2 & \cos k_2 d_2 \end{pmatrix} \quad (2.21)$$

where  $p_{21} = Z_2 / Z_1$  or  $c_2 \rho_2 / c_1 \rho_1$ .

Combine (i) and (ii), we have

$$\begin{pmatrix} A_{m+1,1} \\ B_{m+1,1} \end{pmatrix} = T \begin{pmatrix} A_{m,1} \\ B_{m,1} \end{pmatrix} \quad (2.22)$$

The bilayer transfer matrix  $T = M_{2 \rightarrow 1} M_{1 \rightarrow 2}$ . The elements of  $T$  are

$$T_{11} = \cos(k_1 d_1) \cos(k_2 d_2) - p_{21} \sin(k_1 d_1) \sin(k_2 d_2) \quad (2.23)$$

$$T_{22} = \cos(k_1 d_1) \cos(k_2 d_2) - p_{12} \sin(k_1 d_1) \sin(k_2 d_2) \quad (2.24)$$

$$T_{12} = -\sin(k_1 d_1) \cos(k_2 d_2) - p_{21} \cos(k_1 d_1) \sin(k_2 d_2) \quad (2.25)$$

$$T_{21} = \sin(k_1 d_1) \cos(k_2 d_2) + p_{12} \cos(k_1 d_1) \sin(k_2 d_2) \quad (2.26)$$

From (2.19) and (2.21), we find that  $\det(M_{1 \rightarrow 2}) = p_{12}$  and  $\det(M_{2 \rightarrow 1}) = p_{21}$ .

Therefore, the determinant of  $T$  is equal to  $p_{12}^* p_{21} = 1$ , and hence the eigenvalues of  $T$  must be expressible in the form  $(e^{i\theta}, e^{-i\theta})$ . Then it is natural to define the wave number  $q$  by the relation  $\theta = q d$ . Another way to understand this with a better physical insight is based on Bloch's theorem: For an infinite periodic structure, the solution of the wave equation has the special property

$$\begin{pmatrix} A_{m+1,1} \\ B_{m+1,1} \end{pmatrix} = \lambda \begin{pmatrix} A_{m,1} \\ B_{m,1} \end{pmatrix} \quad (2.27)$$

with  $\lambda = e^{iqd}$ , where  $q$  is the wave number. Thus  $\lambda$  must be an eigenvalue of  $T$ , so

$$\det | T - \lambda I | = 0 \quad (2.28)$$

Hence we obtain the following dispersion relation for propagating modes:

$$\begin{aligned} \cos(qd) &= \cos(\omega d_1 / c_1) \cos(\omega d_2 / c_2) \\ &\quad - \frac{(p_{12} + p_{21})}{2} \sin(\omega d_1 / c_1) \sin(\omega d_2 / c_2) \end{aligned} \quad (2.29)$$

This determines  $q$  (and thus  $\lambda$ ) for a given  $\omega$ . Once  $\lambda$  is determined, the ratio of the amplitudes  $A_{m,1}$  and  $B_{m,1}$  can be found from Eqs.(2.22) and (2.27). The calculated dispersion curve for a Mo/Si multilayer, with  $\Gamma = 0.4$  and  $d = 6.8$  nm, is shown in Fig. 2-3. The parameters are taken to be the bulk values, i.e.,  $\rho_1(\text{Si}) = 2.33$  g/cm<sup>3</sup>,  $c_1 = 6.9 \times 10^3$  m/sec,  $\rho_2(\text{Mo}) = 10.22$  g/cm<sup>3</sup>, and  $c_2 = 6.2 \times 10^3$  m/sec. Note that the dispersion relation

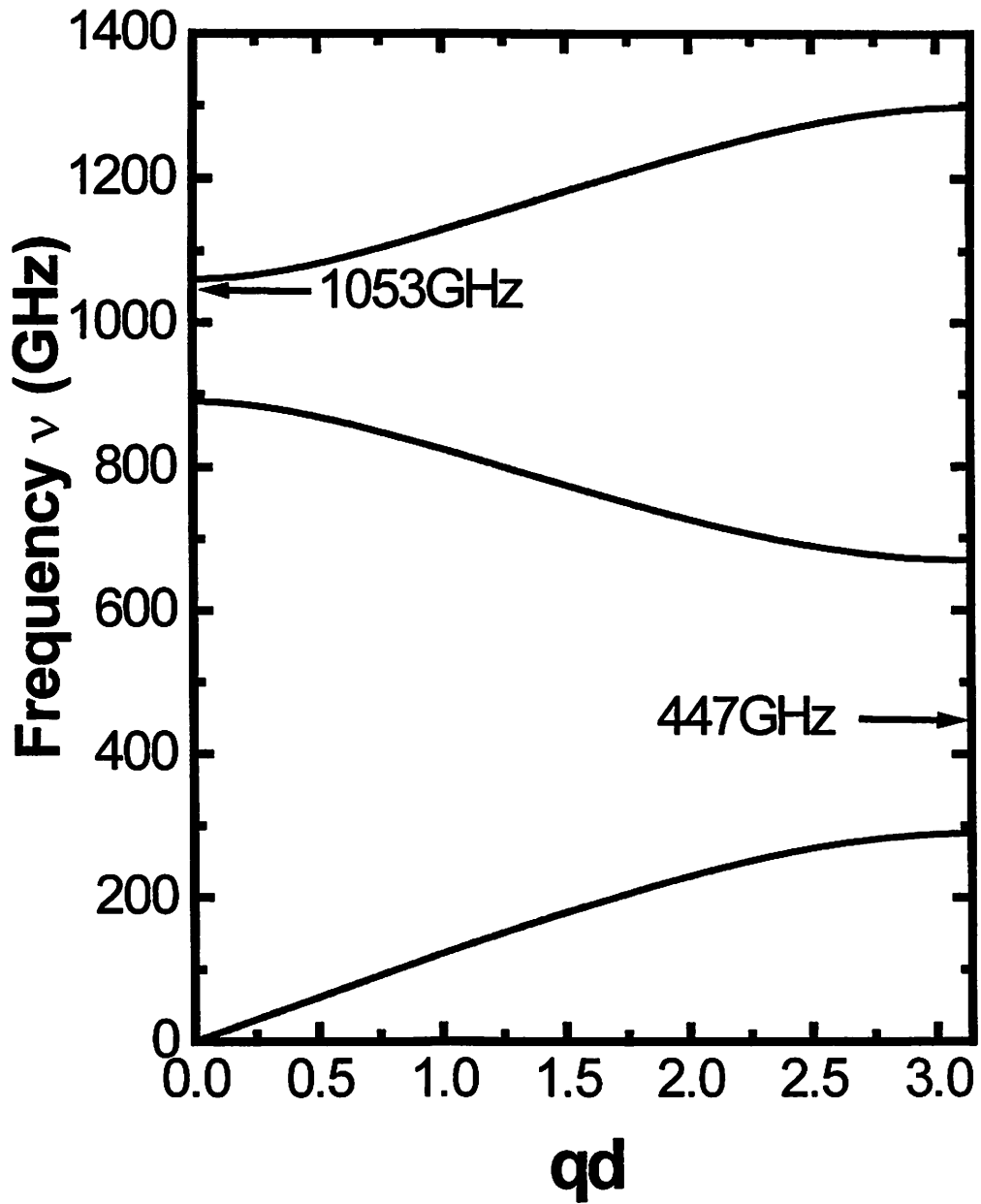


Figure 2-3 Calculated dispersion relation for longitudinal acoustic phonons in a Mo/Si multilayer with  $d = 6.8$  nm and  $\Gamma = 0.4$ . ( $\rho_{\text{Si}} = 2.33$  g/cm<sup>3</sup>,  $c_{\text{Si}} = 6.9 \times 10^3$  m/sec,  $\rho_{\text{Mo}} = 10.22$  g/cm<sup>3</sup>, and  $c_{\text{Mo}} = 6.2 \times 10^3$  m/sec.)

consists of a series of minibranches  $n$ ,  $\omega_n(q)$ , where  $q$  is real and the acoustic displacement is a propagating Bloch wave. These branches are separated by frequency gaps for which  $q$  becomes complex, representing an exponentially damped acoustic wave. No propagating modes are allowed within these gaps.

The frequency gaps are induced by the difference between the acoustic properties of the two constituents. To show this we rewrite Eq. (2.29) as

$$\begin{aligned} \cos( qd ) = \cos \omega \left( \frac{d_1}{c_1} + \frac{d_2}{c_2} \right) \\ - \frac{\varepsilon^2}{2} \sin( \omega d_1 / c_1 ) \sin( \omega d_2 / c_2 ) \end{aligned} \quad (2.30)$$

where

$$\varepsilon = \frac{Z_1 - Z_2}{\sqrt{Z_1 Z_2}} \quad (2.31)$$

The quantity  $\varepsilon$  measures the acoustic impedance mismatch between the two materials[2.19]. If the two materials are well matched, i.e.  $Z_1 \approx Z_2$ , then the last term can be neglected. Eq. (2.30) then becomes

$$\omega = \pm \langle c \rangle \left( q + \frac{2\pi n}{d} \right), \quad n = \text{integer}, \quad \omega > 0, \quad 0 \leq q \leq \frac{\pi}{d} \quad (2.32)$$

where  $\langle c \rangle$  is the harmonic mean of sound velocities  $c_1$  and  $c_2$ , namely:

$$\frac{d}{\langle c \rangle} = \frac{d_1}{c_1} + \frac{d_2}{c_2} \quad (2.33)$$

Equation (2.32) simply corresponds to the folding of an effective bulk dispersion curve  $\omega = \langle c \rangle q$  into the reduced first Brillouin zone. The frequencies at the zone center are given by

$$\omega_n = n \frac{\pi \langle c \rangle}{d}, \quad n = 0, 2, 4, 6, \dots \quad (2.34)$$

whereas the frequencies at the zone edge are given by

$$\omega_n = n \frac{\pi \langle c \rangle}{d}, \quad n = 1, 3, 5, 7, \dots \quad (2.35)$$

The frequency splitting at the zone center and at the zone edge can be calculated by expanding the exact frequency  $\omega$  to second order in  $\Delta\omega_n = \omega - \omega_n$ . The widths of the frequency gaps  $2\Delta\omega_n$  are found to be[2.7]:

$$2\Delta\omega_n \cong 2 \frac{Z_1 - Z_2}{\sqrt{Z_1 Z_2}} \frac{\langle c \rangle}{d} \sin\left(\frac{n\pi}{2} \frac{d_1/c_1 - d_2/c_2}{d_1/c_1 + d_2/c_2}\right), \quad n \text{ even}, \quad (2.36a)$$

$$2\Delta\omega_n \cong 2 \frac{Z_1 - Z_2}{\sqrt{Z_1 Z_2}} \frac{\langle c \rangle}{d} \cos\left(\frac{n\pi}{2} \frac{d_1/c_1 - d_2/c_2}{d_1/c_1 + d_2/c_2}\right), \quad n \text{ odd}, \quad (2.36b)$$

It should be noted that the group velocity of bulk modes at gap edges is equal to zero.

## 2.2.2 Local modes at a free surface

Consider now a semi-infinite multilayer with a free surface at  $z = 0$ . The first layer is composed of material 1. In this situation, besides the bulk modes described above, localized surface modes may exist and be excited. The existence of such modes was first predicted theoretically by B. Djafari-Rouhani *et al.* [2.9]-[2.10] in 1983 and observed experimentally by H.T. Grahn *et al.* [2.11] in 1988. For these modes Eqs. (2.22)-(2.28) still hold, and we can apply Eq. (2.27)  $(m-1)$  times to obtain the relation between the amplitudes  $(A_{1,1}, B_{1,1})$  in the topmost layer and  $(A_{m,1}, B_{m,1})$  in the  $m$ th layer:

$$\begin{pmatrix} A_{m,1} \\ B_{m,1} \end{pmatrix} = \lambda^{m-1} \begin{pmatrix} A_{1,1} \\ B_{1,1} \end{pmatrix} \quad (2.37)$$

To have a solution that decreases in amplitude from the surface into the bulk, it is

necessary that  $|\lambda| < 1$ . An extra boundary condition imposed on the semi-infinite structure is that the stress  $\sigma$  must vanish at the free surface, which implies that  $A_{1,1}=0$ . Therefore from Eq. (2.37), we see that all  $A_{m,1}$ 's vanished. In addition, from Eq. (2.22)  $T_{12}$  has to be zero, which gives

$$p_{12} \tan(\omega d_1 / c_1) + \tan(\omega d_2 / c_2) = 0 \quad (2.38)$$

and 
$$\lambda = \frac{\cos(\omega d_1 / c_1)}{\cos(\omega d_2 / c_2)} \quad (2.39)$$

It is straightforward to show that for all frequencies which are solution of Eq. (2.38),  $|\lambda|$  is less than 1 if  $p_{12} < 1$ . On the other hand, if  $p_{12} > 1$ ,  $|\lambda|$  is always greater than 1. Thus, surface modes only exist if the topmost sublayer of the multilayer has a smaller acoustic impedance  $Z_1 = \rho_1 c_1$  (e.g. Si in Mo/Si and Be in Mo/Be multilayers) than the other. The eigenvalue is related to the exponential decay length  $l$  of the mode by

$$l = -d / \ln(|\lambda|) \quad (2.40)$$

The arrows in Fig. 2-3 indicate the surface mode frequencies for a Mo/Si multilayer calculated from Eq. (2.38). In Fig. 2-4, the spatial dependence of the stress and strain associated with the surface modes in the lowest two band gaps is shown. For the surface mode in the lowest zone-boundary gap the stress and strain change sign after each bilayer. In the first zone-center gap, the stress and strain of the surface mode have the same sign after each bilayer.

### 2.3 $n$ -sublayer structure with cap layers

The analytical model derived in the previous section can be further generalized to deal with more complex structures, such as superlattices with more than two sublayers or



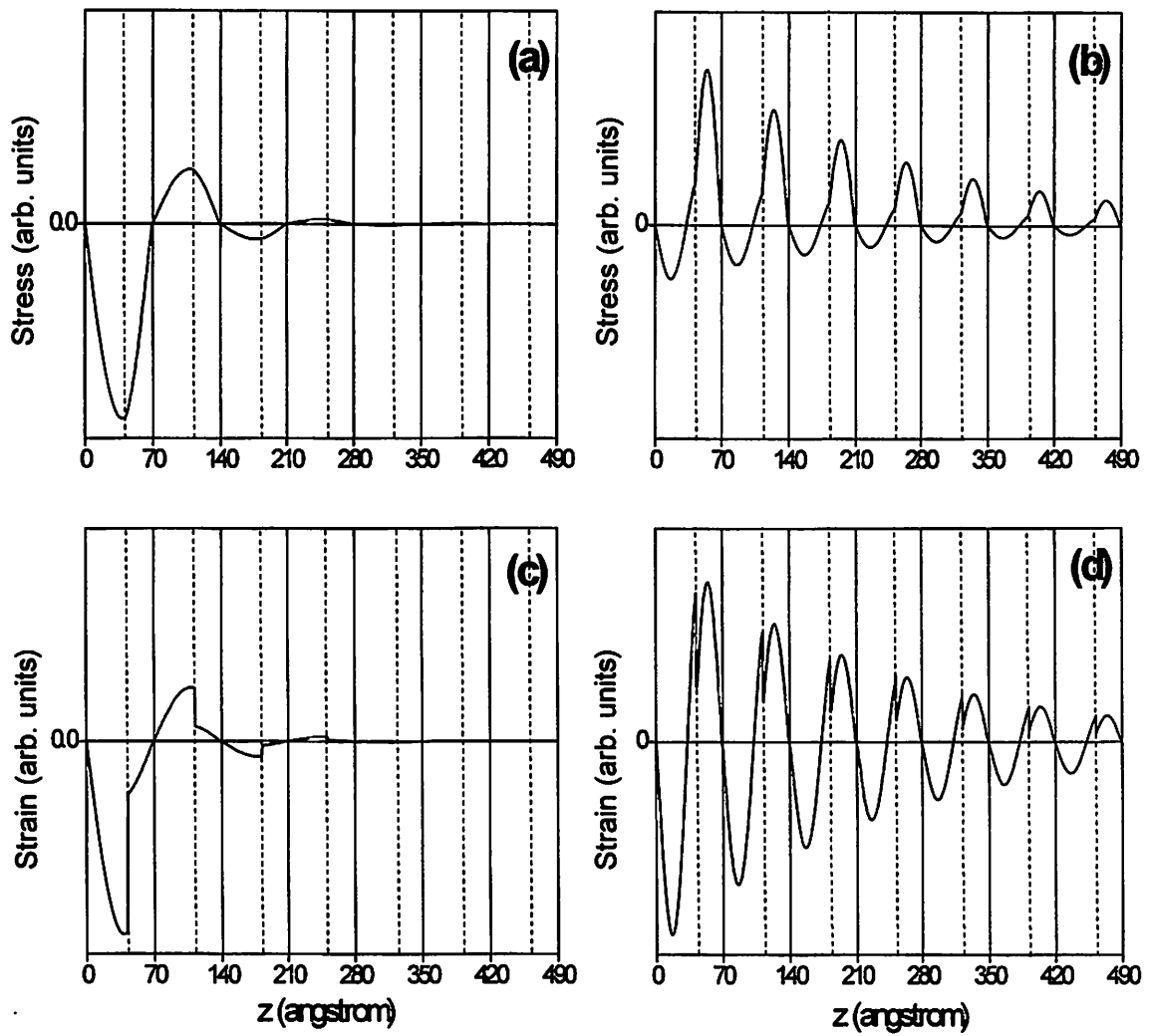


Figure 2-4 Spatial dependence of the stress and strain for the surface modes in (a)(c) the first (lowest zone-boundary) gap and (b)(d) the second (lowest zone-center) gap for a Mo/Si multilayer beginning with a Si layer ( $d = 70$  angstrom and  $\Gamma = 0.4$ ).

with arbitrary cap layers. This is useful in calculating surface mode frequencies for a non-ideal multilayer with strong inter-diffusion between sublayers, or a multilayer with deliberately or unintentionally (e.g. native oxide) deposited cap layers.

### 2.3.1 General solution for a capped $n$ -sublayer structure

The geometry of the multilayer is shown in Fig. 2-5. The structure begins with  $n_c$  capping layers of materials  $i$  of thicknesses  $d_i^{(c)}$  ( $i = 1, 2, \dots, n_c$ ). Each coating period of the multilayer consists of  $n$  sublayers of thicknesses  $d_j$  ( $j = 1, 2, \dots, n$ ). The Eqs. (2.13)-(2.15) and the boundary conditions at the surface and all interfaces still hold. The spatial part  $w(z)$  of the solution  $u(z, \tau)$  in the  $j$ th sublayer of the  $m$ th period can be written as

$$w(z) = A_{m,j} \sin[k_j(z - z_m - \sum_{l=1}^{j-1} d_l)] + B_{m,j} \cos[k_j(z - z_m - \sum_{l=1}^{j-1} d_l)] \quad (2.41)$$

$$(m = 1, 2, 3, \dots, \infty; j = 1, 2, \dots, n)$$

Where  $A_{m,j}$ 's and  $B_{m,j}$ 's are amplitudes, and  $k_j = \omega/c_j$ . The boundary conditions relate the amplitudes of adjacent sublayers:

$$\begin{pmatrix} A_{m,j+1} \\ B_{m,j+1} \end{pmatrix} = M_{j \rightarrow j+1} \begin{pmatrix} A_{m,j} \\ B_{m,j} \end{pmatrix} \quad (2.42)$$

$$\text{The sublayer transfer matrix } M_{j \rightarrow j+1} = \begin{pmatrix} p_{j,j+1} \cos k_j d_j & -p_{j,j+1} \sin k_j d_j \\ \sin k_j d_j & \cos k_j d_j \end{pmatrix} \quad (2.43)$$

where  $p_{j,j+1} = Z_j / Z_{j+1}$ .

The transfer matrix for the whole period is

$$T = M_{n \rightarrow 1} M_{n-1 \rightarrow n} M_{n-2 \rightarrow n-1} \cdots M_{j \rightarrow j+1} \cdots M_{1 \rightarrow 2} \quad (2.44)$$

And Eqs. (2.22) and (2.27) remain unchanged

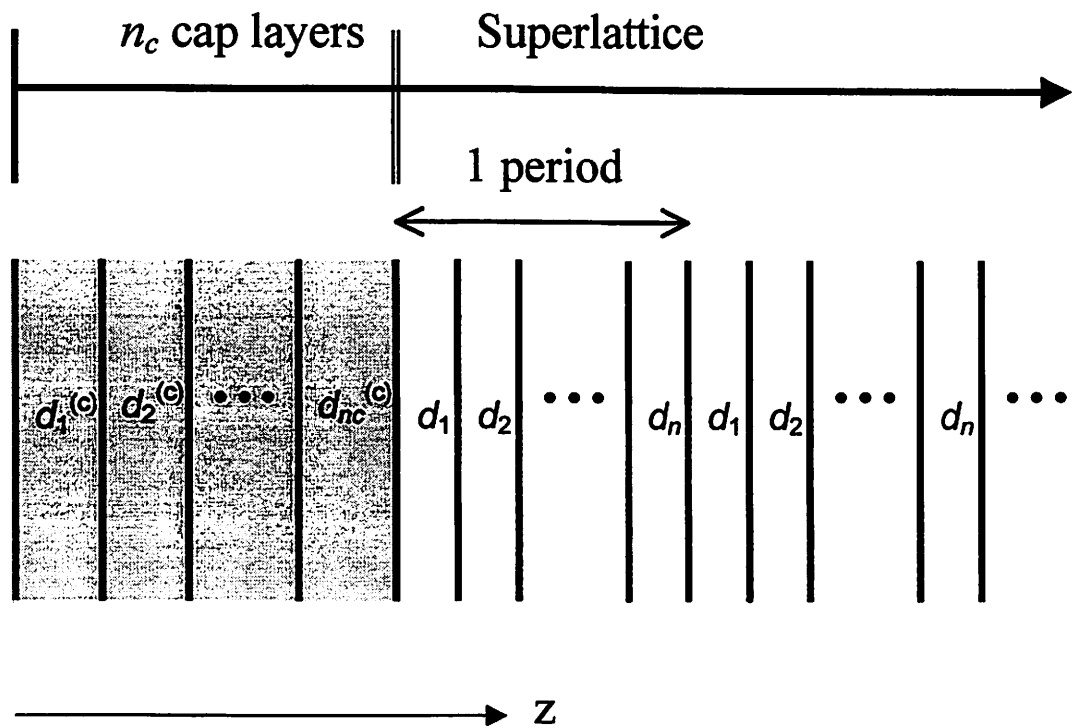


Figure 2-5 Geometry of an  $n$ -sublayer structure with  $n_c$  cap layers

$$\begin{pmatrix} A_{m+1,1} \\ B_{m+1,1} \end{pmatrix} = T \begin{pmatrix} A_{m,1} \\ B_{m,1} \end{pmatrix} = \lambda \begin{pmatrix} A_{m,1} \\ B_{m,1} \end{pmatrix}$$

Thus the dispersion relation for propagating modes can be obtained by solving the characteristic equation (2.28).

The cap layers play an important role in deciding the surface-mode frequencies. We define the transfer matrix for the cap layers in the same way as we did above

$$\begin{pmatrix} A_{i+1}^{(c)} \\ B_{i+1}^{(c)} \end{pmatrix} = M_{i \rightarrow i+1}^{(c)} \begin{pmatrix} A_i^{(c)} \\ B_i^{(c)} \end{pmatrix} \quad (2.45)$$

where  $A_i^{(c)}$  and  $B_i^{(c)}$  are the amplitudes in layer  $i$  of the cap layers ( $i = 1, 2, \dots, n_c$ ). The elements of  $M_{i \rightarrow i+1}^{(c)}$  are given by equations analogous to Eq. (2.43), allowing for arbitrary materials with various thicknesses. We can then define a matrix  $T^{(c)}$  which relates the amplitudes  $A_1^{(c)}, B_1^{(c)}$  in the first cap layer to the amplitudes  $A_{1,1}, B_{1,1}$  in the first layer of the main part of the multilayer.

$$\begin{pmatrix} A_{1,1} \\ B_{1,1} \end{pmatrix} = T^{(c)} \begin{pmatrix} A_1^{(c)} \\ B_1^{(c)} \end{pmatrix} \quad (2.46)$$

It follows that

$$T^{(c)} = \prod_i M_{i \rightarrow i+1}^{(c)} \quad (2.47)$$

where the product starts with  $i = n_c$  and ends with  $i = 1$ , and the first factor  $M_{n_c \rightarrow n_c+1}^{(c)}$  represents the transfer matrix from the last cap layer ( $i = n_c$ ) to the first superlattice sublayer ( $m = 1, j = 1$ ). The condition that the stress be zero at the free surface of the multilayer requires that  $A_1^{(c)}$  be zero. Therefore, from Eq. (2.46), we have

$$\frac{A_{1,1}}{B_{1,1}} = \frac{T_{12}^{(e)}}{T_{22}^{(e)}} \equiv C \quad (2.48)$$

Substituting into Eqs. (2.22) and (2.27), we obtain the equations for determining the eigenfrequencies and mode patterns of the surface modes:

$$\lambda = T_{21}C + T_{22} \quad (2.49)$$

$$T_{21}C^2 + (T_{22} - T_{11})C - T_{12} = 0 \quad (2.50)$$

where  $|\lambda|$  must be less than 1 just as in the simple 2-sublayer case. The attenuation length  $l$  for the surface mode is given by Eq. (2.40). These results can be incorporated into a computer program to calculate the normal modes of a capped  $n$ -sublayer superlattice.

### 2.3.2 Solution for a 4-sublayer system

Although we have arrived at the final results (2.49) and (2.50) for a general case, the expression of each element of the transfer matrix  $T$  may still be too complicated to write down explicitly. In the case of Mo/Si multilayers, the interdiffusion regions between Mo and Si layers are too thick to be neglected ( $\sim 20\%$  of the total thickness for  $d = 7$  nm), and the chemical composition of the mixture may vary gradually with distance. In this case, a rigorous solution calls for a large number of sublayers in the calculation and the problem becomes very difficult to handle. However, as a first-order approximation, we can consider the interdiffusion region as another sublayer of uniform molybdenum silicide compound. Then the problem is reduced to a 4-sublayer system: Si - silicide 1 - Mo - silicide 2.

The analytical expressions of the elements of  $T$  for a 4-sublayer structure are given as follows:

$$\begin{aligned}
T_{11} = & p_{12} (\cos k_1 d_1) \{ (\sin k_2 d_2) [-p_{34} p_{41} (\cos k_4 d_4) (\sin k_3 d_3) - p_{41} (\cos k_3 d_3) (\sin k_4 d_4)] \\
& + p_{23} (\cos k_2 d_2) [p_{34} p_{41} (\cos k_3 d_3) (\cos k_4 d_4) - p_{41} (\sin k_3 d_3) (\sin k_4 d_4)] \} \\
& + (\sin k_1 d_1) \{ (\cos k_2 d_2) [-p_{34} p_{41} (\cos k_4 d_4) (\sin k_3 d_3) - p_{41} (\cos k_3 d_3) (\sin k_4 d_4)] \\
& - p_{23} (\sin k_2 d_2) [p_{34} p_{41} (\cos k_3 d_3) (\cos k_4 d_4) - p_{41} (\sin k_3 d_3) (\sin k_4 d_4)] \}
\end{aligned} \tag{2.51}$$

$$\begin{aligned}
T_{12} = & -p_{12} (\sin k_1 d_1) \{ (\sin k_2 d_2) [-p_{34} p_{41} (\cos k_4 d_4) (\sin k_3 d_3) - p_{41} (\cos k_3 d_3) (\sin k_4 d_4)] \\
& + p_{23} (\cos k_2 d_2) [p_{34} p_{41} (\cos k_3 d_3) (\cos k_4 d_4) - p_{41} (\sin k_3 d_3) (\sin k_4 d_4)] \} \\
& + (\cos k_1 d_1) \{ (\cos k_2 d_2) [-p_{34} p_{41} (\cos k_4 d_4) (\sin k_3 d_3) - p_{41} (\cos k_3 d_3) (\sin k_4 d_4)] \\
& - p_{23} (\sin k_2 d_2) [p_{34} p_{41} (\cos k_3 d_3) (\cos k_4 d_4) - p_{41} (\sin k_3 d_3) (\sin k_4 d_4)] \}
\end{aligned} \tag{2.52}$$

$$\begin{aligned}
T_{21} = & (\sin k_1 d_1) \{ -p_{23} (\sin k_2 d_2) [(\cos k_4 d_4) (\sin k_3 d_3) + p_{34} (\cos k_3 d_3) (\sin k_4 d_4)] \\
& + (\cos k_2 d_2) [(\cos k_3 d_3) (\cos k_4 d_4) - p_{34} (\sin k_3 d_3) (\sin k_4 d_4)] \} \\
& + p_{12} (\cos k_1 d_1) \{ p_{23} (\cos k_2 d_2) [(\cos k_4 d_4) (\sin k_3 d_3) + p_{34} (\cos k_3 d_3) (\sin k_4 d_4)] \\
& + (\sin k_2 d_2) [(\cos k_3 d_3) (\cos k_4 d_4) - p_{34} (\sin k_3 d_3) (\sin k_4 d_4)] \}
\end{aligned} \tag{2.53}$$

$$\begin{aligned}
T_{22} = & (\cos k_1 d_1) \{ -p_{23} (\sin k_2 d_2) [(\cos k_4 d_4) (\sin k_3 d_3) + p_{34} (\cos k_3 d_3) (\sin k_4 d_4)] \\
& + (\cos k_2 d_2) [(\cos k_3 d_3) (\cos k_4 d_4) - p_{34} (\sin k_3 d_3) (\sin k_4 d_4)] \} \\
& - p_{12} (\sin k_1 d_1) \{ p_{23} (\cos k_2 d_2) [(\cos k_4 d_4) (\sin k_3 d_3) + p_{34} (\cos k_3 d_3) (\sin k_4 d_4)] \\
& + (\sin k_2 d_2) [(\cos k_3 d_3) (\cos k_4 d_4) - p_{34} (\sin k_3 d_3) (\sin k_4 d_4)] \}
\end{aligned} \tag{2.54}$$

Following the same procedures described in previous sections, we can easily calculate the dispersion curve and the surface-mode frequencies once the material parameters are known.

### 2.3.3 Surface oxide treated as a cap layer

Silicon is chemically more stable in the air than molybdenum and thus is usually chosen as the top layer material in a Mo/Si multilayer for EUVL. Nevertheless, the surface of the first Si layer will still oxidize and form a thin layer of native oxide SiO<sub>2</sub>. Suppose that it has a thickness  $d_{ox}$  and density  $\rho_{ox}$ , and that the thickness of the first Si layer changes from  $d_{Si}$  to  $d_{Si}'$ . The conservation of Si atoms gives

$$\frac{(d_{Si} - d_{Si}')\rho_{Si}}{w_{Si}} = \frac{d_{ox}\rho_{ox}}{w_{ox}} \quad (2.55)$$

where  $w_{Si}$  and  $w_{ox}$  are the weights for a Si atom and a SiO<sub>2</sub> molecule, respectively. Then we find

$$d_{Si}' = d_{Si} - 0.46d_{ox} \quad (2.56)$$

So the cap layers in this case consist of an oxide layer of thickness  $d_{ox}$  and a Si layer of thickness  $d_{Si}'$ . And the superlattice underneath started with Mo instead of Si.

Figure 2-6 shows the calculated frequencies for the lowest two surface modes as functions of  $d_{ox}$ . Periodicity  $d$  is equal to 6.84 nm and 30.0 nm in (a) and (b), respectively, and  $\Gamma$  is 0.4 in both cases. Material parameters  $\rho_{ox} = 2.2 \text{ g/cm}^3$  and  $c_{ox} = 5 \times 10^3 \text{ m/s}$  were assumed. The dashed lines in Fig. 2-6 are the edges of the frequency gaps. Note that the surface-mode frequencies can be any value within each gap when  $d_{ox}$  is varied. The curve in each gap consists of a number of branches, and each branch appears from the top of the gap (except the first branch) and decreases smoothly until it merges with the lower

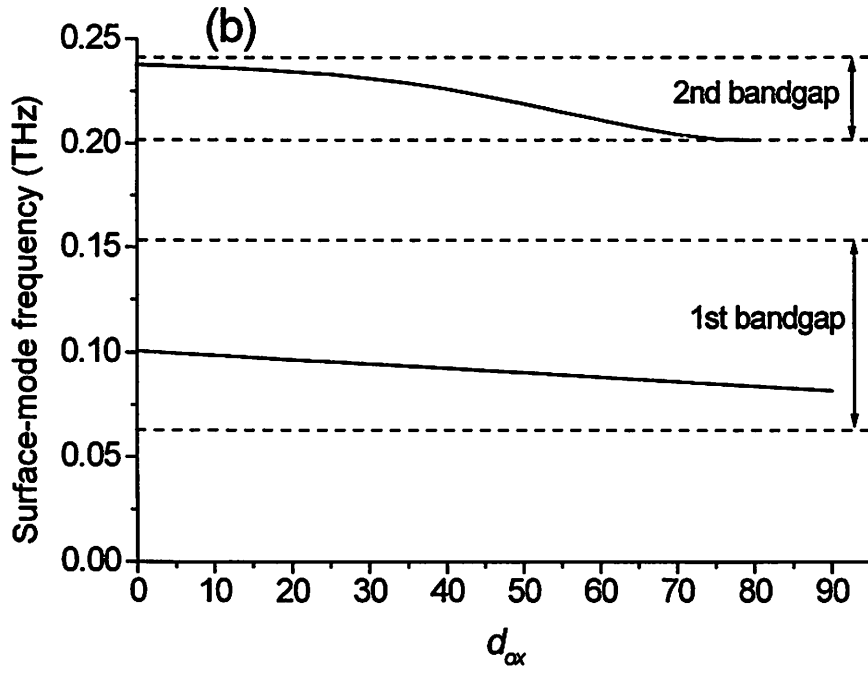
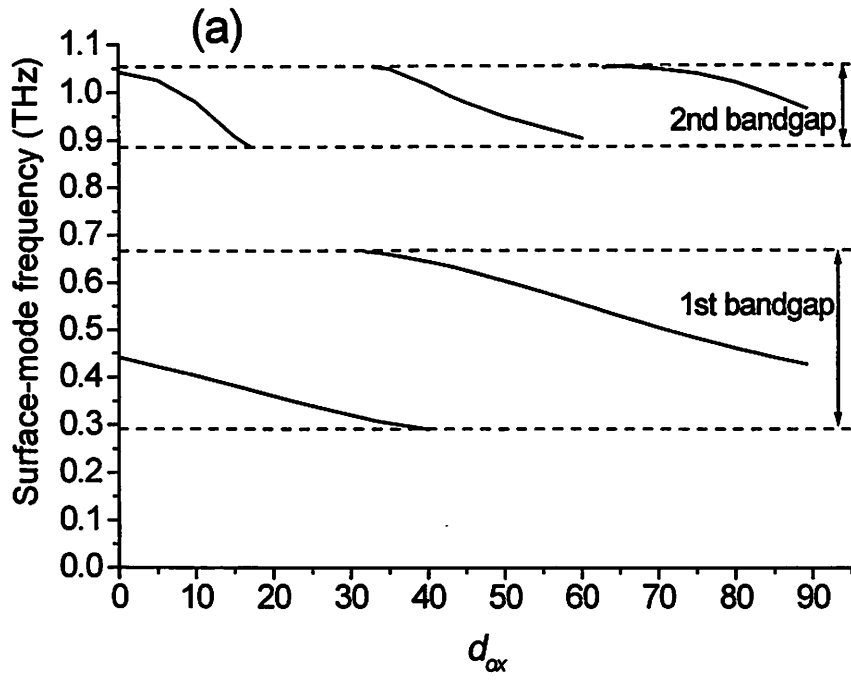


Figure 2-6 Calculated frequencies for the lowest two surface modes as a function of  $d_{ox}$ .

$\Gamma = 0.4$ .  $d = 6.84$  nm in (a) and 30.0 nm in (b).



edge of the gap. Assuming  $d_{ox} = 10 \text{ \AA}$ , the surface-mode frequencies  $\nu_1$  and  $\nu_2$  in Fig. 2-6 (a) will decrease by 1% and 1.2%, respectively, per  $\text{\AA}$  of oxide growth. The impact of surface oxide is greatly reduced in multilayers with thicker  $d$ . For example, in 2-6 (b) the changes of  $\nu_1$  and  $\nu_2$  per  $\text{\AA}$  of oxide growth are only 0.2% and 0.07%, respectively.

## References

- [2.1] J.G. Fujimoto, J.M. Liu, E.P. Ippen, and N. Bloembergen, *Physical Review Letters*, **53**, 1837 (1984).
- [2.2] R.W. Shoenlein, W.Z. Lin, J.G. Fujimoto, and G.L. Eesley, *Physical Review Letters*, **58**, 1680 (1987).
- [2.3] S.D. Brorson, J.G. Fujimoto, and E.P. Ippen, *Physical Review Letters*, **59**, 1962 (1987).
- [2.4] C. Thomsen, H.T. Grahn, H.J. Maris, and J. Tauc, *Physical Review*, **B 34**, 4129 (1986).
- [2.5] H.J. Maris, *Scientific American*, Jan. 1998, p.86.
- [2.6] C. Colvard, R. Merlin, M.V. Klein, and A.C. Gossard, *Physical Review Letters*, **45**, 298 (1980).
- [2.7] B. Jusserand and M. Cardona, in *Light Scattering in Solids V*, edited by M. Cardona and G. Guntherodt, Springer-Verlag, Heidelberg, 1989.
- [2.8] H.J. Trodahl, P.V. Santos, G.V.M. Williams, A. Bittar, *Physical Review*, **B 40**, 8577 (1989).
- [2.9] R.E. Camley, B.Djafari-Rouhani, L. Dobrzynski, and A.A. Maradudin, *Physical Review*, **B 27**, 7318 (1983).
- [2.10] B.Djafari-Rouhani, L. Dobrzynski, O Hardouin Duparc, R.E. Camley, and A.A. Maradudin, *Physical Review*, **B 28**, 1711 (1983).
- [2.11] H.T. Grahn, H.J. Maris, J. Tauc, and B. Abeles, *Physics Review*, **B 38**, 6066 (1986).
- [2.12] H.T.Grahn, H.J.Maris, and J.Tauc, *IEEE J. Quantum Electron.*, **25**, 2562 (1989).

- [2.13] W. Chen, Y. Lu, H.J. Maris and G. Xiao, *Physical Review*, **B 50**, 14506 (1994).
- [2.14] B.Perrin, B.Bonello, J.C.Jeannet and E.Romatet, *Physica*, **B 219&220**, 681 (1996).
- [2.15] B.Bonello, B.Perrin, E.Romatet and J.C.Jeannet, *Ultrasonics*, **35**, 223 (1997).
- [2.16] N-W.Pu, S.Jeong, R-A.Zhao, and J.Bokor, *Applied Physics Letters.*, **74**, 320 (1999).
- [2.17] N-W.Pu, S.Jeong, R-A.Zhao, and J.Bokor, *Proceedings of SPIE on Emerging Lithographic Technologies III*, vol.**3676**, p.627, 1999.
- [2.18] N-W.Pu, J. Bokor, S. Jeong, and R-A. Zhao, *Journal of Vacuum Science and Technology*, **B 17**, 3014 (1999).
- [2.19] P. Basseras, S.M. Gracewski, G.W. Wicks, and R.J.D. Miller, *Journal of Applied Physics*, **75**, 2761 (1994).

# Chapter 3. Experimental Setup

This chapter contains a detailed description of the experimental setup for picosecond ultrasonics using a time-resolved transient reflectivity technique. A novel alternating-pump technique has been proposed and successfully demonstrated to separate the purely vibrational response of interest from the slowly-varying non-vibrational response, and to enhance the signal-to-noise ratio by up to 20 dB. The measured results on a Mo/Si multilayer with  $d = 6.84$  nm and  $\Gamma \approx 0.5$  are shown to demonstrate the advantages of this technique. The surface modes lying within the lowest two frequency gaps were simultaneously observed in this sample.

## 3.1 Experimental setup

The picosecond ultrasonic technique involves excitation of the sample by a first optical pulse (the pump pulse) and monitoring of the subsequent relaxation processes by a weaker pulse (the probe pulse) delayed with respect to the pump by means of a variable optical path. There are various detection schemes proposed: monitoring the intensity of the reflected probe beam[3.1], measuring the angular deflection of the probe beam[3.2]-[3.3], or detecting the displacement of the surface of the sample by an interferometric method[3.4]. In all cases, the signal of interest is very weak and generally, the relative variations of the measured quantity are in the range of  $10^{-5} \sim 10^{-7}$ .

The schematic diagram of our experimental setup is shown in Fig. 3-1. This is a typical setup for optical pump and probe transient reflectivity measurement, except for

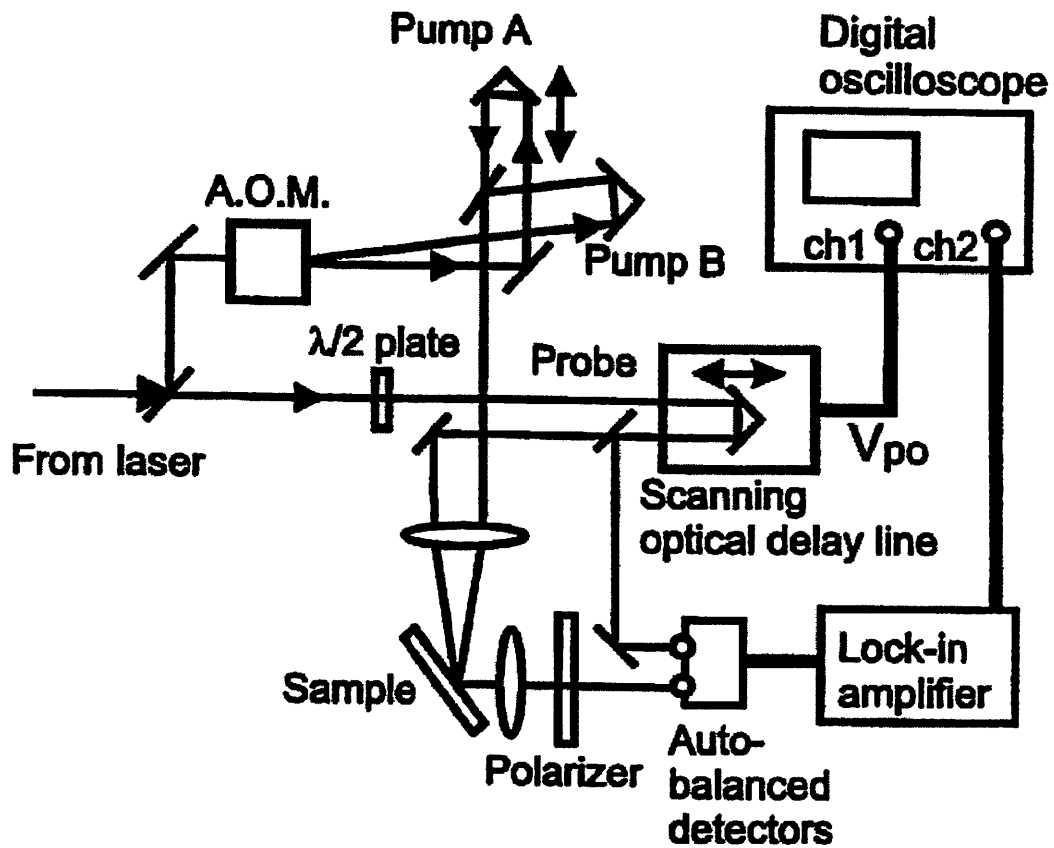


Figure 3-1 Experimental setup (A.O.M.: acousto-optic modulator). Pumps A and B are, respectively, the zeroth- and the first-order diffracted beams from the A.O.M.  $\lambda/2$  plate: half-wave plate.  $V_{po}$ : the position output of the scanning optical delay line.

a slight modification in the pump arm to improve the signal-to-noise ratio: two pump beams A and B, instead of one, were used to excite the sample. The purpose and effect of this arrangement are to be discussed in the next section. For now, let's consider that one of the pump beams is blocked, and it becomes a conventional pump-probe setup. The light pulses were produced by an ultrafast Ti:sapphire laser oscillator (Clark-MXR, NJA-4) pumped by an argon ion laser (Spectra-Physics, Beamlok 2060-075) with a pumping power of 4.5 W. The self-modelocked[3.5] Ti:sapphire laser was operated at 800 nm, with a FWHM pulse duration of  $\sim 130$  fs and a repetition rate of 100 MHz. The average output of the oscillator is about 300 mW, which corresponds to a pulse energy of 3 nJ per pulse. The laser output was split into pump and probe beams. To obtain a high signal-to-noise ratio, a lock-in detection technique was employed. And so the pump arm was chopped by an acousto-optic (AO) modulator, which is amplitude-modulated by a 100 kHz square wave. The laser pulses were broadened to  $\sim 190$  fs after passing through the 6-cm-thick AO modulator (IntraAction, AOM-40N) due to dispersion. Fig. 3-2 shows the autocorrelation traces of a laser pulse measured before and after the AO modulator, using second harmonic generation (SHG). The FWHM widths of these traces are 180 and 270 fs, which is  $\sqrt{2}$  times the real pulsewidths assuming a Gaussian pulse shape[3.6]. The AO modulator is driven by an RF power amplifier at 40MHz carrier frequency, and has a diffraction efficiency (into the first order) of  $\sim 90\%$ .

The pulses were focused onto the sample by a 10X objective with a numerical aperture (NA) of 0.25. The spot sizes were approximately 10  $\mu\text{m}$  and 6  $\mu\text{m}$  (diameter) for pump and probe beams, respectively. The spot size of the pump beam was

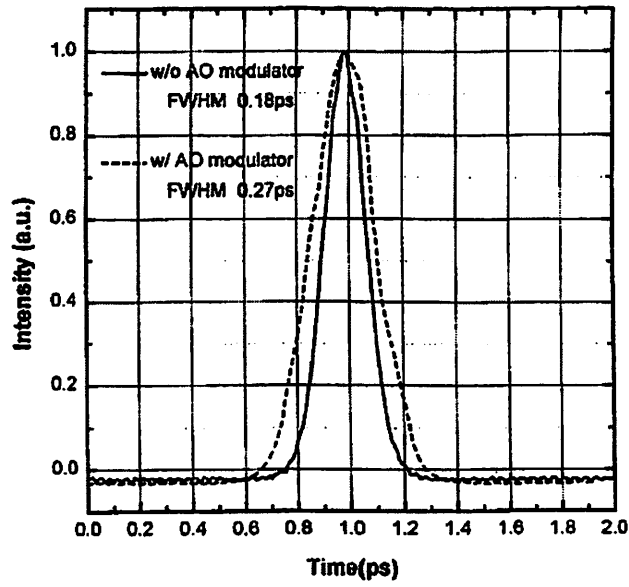


Figure 3-2 The SHG autocorrelation traces of a laser pulse measured before and after the AO modulator.

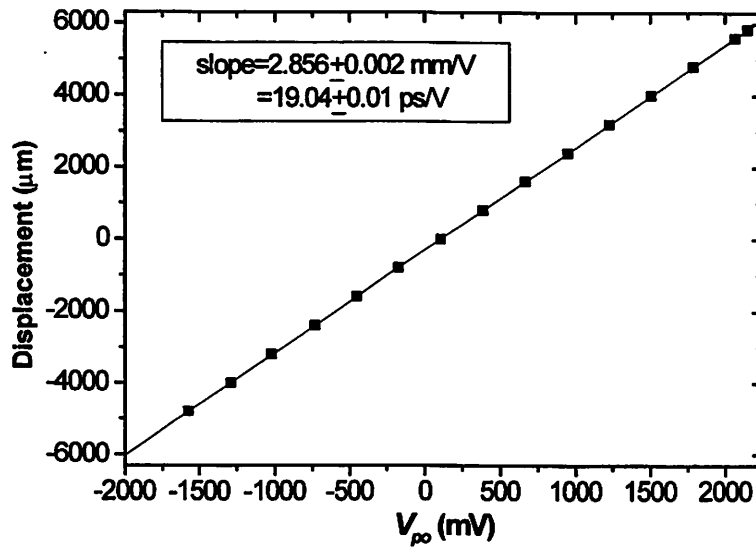


Figure 3-3 The measured dependence of stage displacement on  $V_{po}$ .

deliberately made bigger so that the probe beam sees a more uniformly excited area. The pump pulses deposit optical energy in the multilayer and impulsively excite acoustic waves in the structure. The optical absorption occurs predominantly in Mo layers with an absorption length of  $\sim 20$  nm[3.7]. An initial stress field is set up in the mechanical structure by the heat, and the relaxation of this stress field then launches strain waves in the multilayer. A slight change of the optical reflectivity (on the order of 0.001%) is induced by these strain waves, and is then detected by a time-delayed probe pulse. The light intensity of the probe arm is attenuated to 10 times lower than the pump arm in order to avoid strong disturbance on the material response induced by the pump.

Several methods were used to enhance the signal-to-noise ratio because of the low signal level: (1) An RF lock-in amplifier (Stanford Research Systems, SR844) was used for noise rejection. It provides the 100 kHz reference frequency for the AO modulator and detects only the component of signal within a narrow bandwidth centered at this frequency[3.8]. The integration time constant  $T_0$  was set to be 300  $\mu$ s, which corresponds to a bandwidth  $B = \frac{1}{2\pi T_0} = 530$  Hz. Since the pump light is chopped by the AO modulator, the optical reflectivity change induced by the pump pulses is also modulated at the same frequency, and can be selectively picked out among all unwanted signals and noise by the lock-in amplifier. (2) A half-wave plate was used to rotate the polarization of the probe beam by 90 degrees (from s-polarization to p-polarization). A polarizer placed in front of the detector then helped to block any s-polarized light (extinction ratio =  $10^{-5}$ ) and thereby minimize the noise due to scattered pump light, which is modulated at 100 kHz and will be picked up by the lock-in amplifier as a false signal and swamp the real signal. (3) An auto-balanced detector circuit (New Focus, Nirvana 2007), which



compares and balances the two inputs with an adjustable feedback-loop time constant, is used to help suppress low frequency laser noise.

The delay time between pump and probe beams was varied by a scanning optical delay line (Clark-MXR, ODL-150) driven by a sinusoidal wave at a frequency around 2 Hz. The controller of this optical delay scanner has a position output whose voltage ( $V_{po}$ ) is proportional to the stage displacement (or optical delay  $\tau$ ). Fig. 3-3 shows the measured dependence of its displacement on  $V_{po}$ . The measured slope is  $2.856 \pm 0.002$  mm/V or  $19.04 \pm 0.01$  ps/V. This position output  $V_{po}$  and the detected signal were taken simultaneously as we scanned the delay line, and were recorded and averaged 256 times by a digital oscilloscope (Tektronix, TDS 320) in  $\sim 2$  minutes. Thus we can acquire and plot the traces of the induced reflectance change,  $\Delta R$ , vs. delay time  $\tau$ . An example of measured trace  $\Delta R(\tau)$  for a Mo/Si multilayer ( $d = 6.84$  nm,  $\Gamma \approx 0.5$ ) is shown in Fig. 3-4(a). The acoustic vibrations appear as a weak oscillatory part on the curve, which is superimposed on a much larger non-vibrational response. Fig. 3-4(b) shows a magnified view of the vibrational response. One can see the beating between two surface modes. Note that the signal measured at negative delay time (i.e., time before the excitation by the pump) is not zero. This offset of the  $\Delta R$  trace originates from the accumulation of residual heat deposited by each pump pulse, and has been analyzed by B. Bonello *et al.*[3.9].

### 3.2 The alternating-pump technique

The technical difficulty for probing the surface modes is that the vibrational response

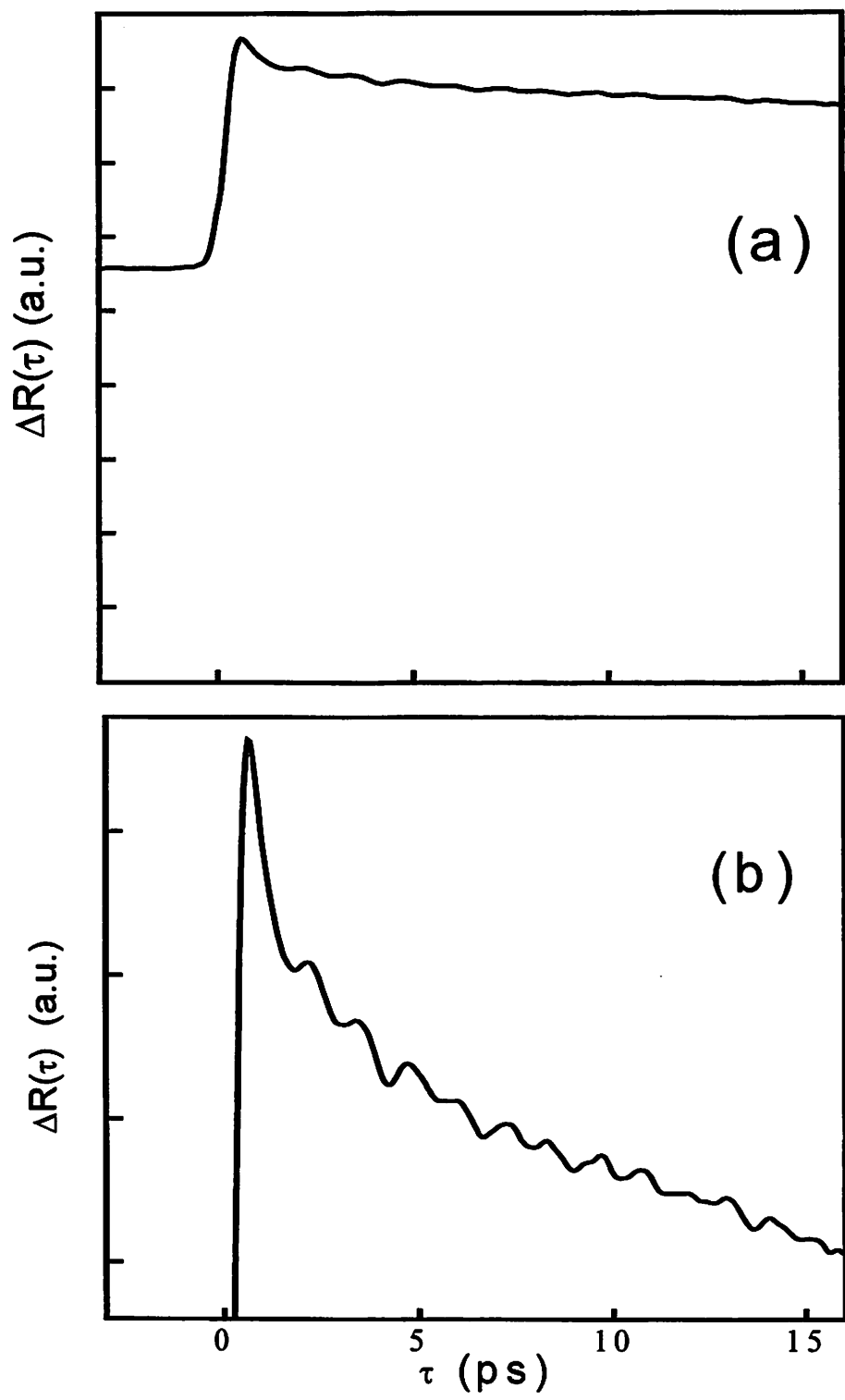


Figure 3-4 (a) A measured trace  $\Delta R(\tau)$  for a Mo/Si multilayer ( $d = 6.84$  nm,  $\Gamma \approx 0.5$ ).

(b) A magnified view of (a) to zoom in on the vibrational response.

of interest is typically 1 to 2 orders of magnitude weaker than an interfering non-vibrational response of the materials, which itself is not large ( $\Delta R_{nonvib}/R_0$  is usually on the order of  $10^{-2}\sim 10^{-5}$ ). Several problems arise because of the existence of this unwanted non-vibrational response: (1) It seriously deteriorates the signal-to-noise ratio. Note that the noise of laser power fluctuation is proportional to the total signal. The non-vibrational part of the signal is much larger than the vibrational part, and thus contributes a significant amount to laser fluctuation noise. (2) It causes an overloading problem to the lock-in amplifier when we try to zoom in on the much weaker vibrational signal by increasing the detection sensitivity. (3) Sometimes, even the total change on the non-vibrational signal is much bigger than the wiggles (see Fig. 3-4(b) for example). So even if one could successfully increase the gain without overloading the amplifier, our detection sensitivity is still limited by the dynamic range of the signal.

To solve these problems, a novel alternating-pump technique has been proposed and implemented as shown in Fig. 3-1. The idea of this 2-pump-beam arrangement is to suppress the non-vibrational signal by a smart detection scheme. Pump beams A and B are respectively the zeroth- and the first-order diffracted beams from the acousto-optic modulator. . Figure 3-5 shows the timing of the incident pump and probe pulses in the conventional and the new schemes. We see that the pump beams A and B come alternately onto the sample at a frequency of 100 kHz, and the lock-in amplifier detects the modulated signal, which is proportional to the difference of the individual responses excited by the two pumps. Figure 3-6 illustrates the scenario: we are basically detecting the difference between the solid and the dashed curves, and so by slightly delaying pump A with respect to pump B, it is possible to cancel out the slowly-varying part of the non-

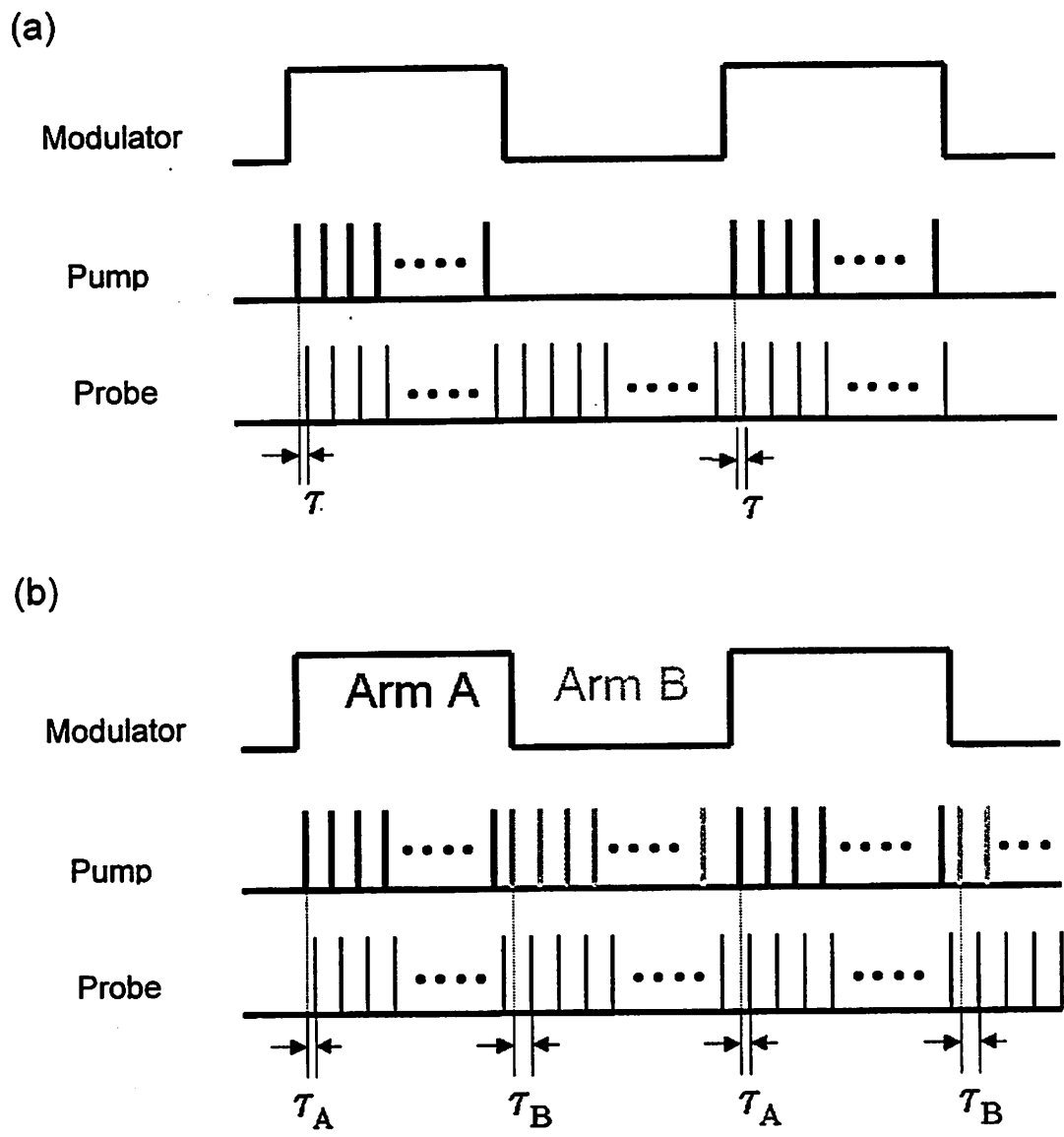


Figure 3-5 Timing of the pump and probe laser pulses in (a) the conventional scheme, (b) the alternating-pump scheme.

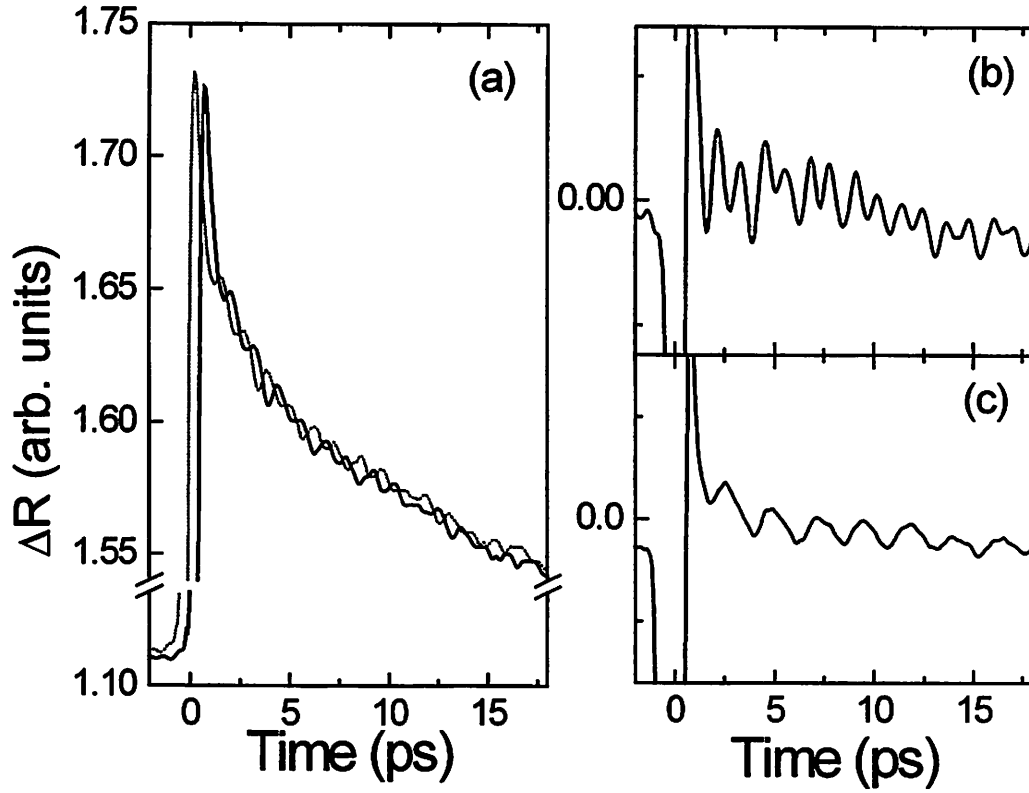


Figure 3-6 (a)  $\Delta R(\tau)$  measured by conventional pump-probe technique (dotted line : with pump A only; solid line : with pump B only). (b) Same result obtained using the 2-pump scheme with  $\tau_{AB} = 0.57$  ps (2nd-gap mode fully revealed). (c) 2-pump scheme with  $\tau_{AB} = 1.14$  ps (2nd-gap mode cancelled).

vibrational response while the faster vibrational response is preserved. Fig. 3-6 (b) and (c) show examples of near-perfect cancellation of the non-vibrational response. It can be very clearly seen that at least two vibration modes were simultaneously excited in this sample ( $d = 6.84$  nm,  $\Gamma \approx 0.5$ ). The difference between the traces in (b) and (c) is due to the different delay time between pump A and B,  $\tau_{AB}$ . In Fig. 3-6 (b),  $\tau_{AB}$  was set as one half of the period (0.57 ps) of the higher-frequency mode ( $\sim 1/4$  that of the lower-frequency mode), and thus the higher-frequency mode was preferably revealed while the lower-frequency mode was slightly suppressed by a factor of  $\sqrt{2}$ . However, beating between these two modes is readily seen. By properly adjusting  $\tau_{AB}$  to exactly one period (1.14 ps) of the higher-frequency mode, we successfully cancelled this mode and clearly unveiled the other mode (Fig. 3-6 (c)).

The primary advantage of this scheme is that the low frequency noise of laser power fluctuations can be significantly suppressed. Consider a conventional single pump setup with only pump arm A. The reflected probe signal received by the detector is

$$P_{sig}^A(t; \tau) = P_{probe}(t) [ R_0 + \Delta R(t; \tau) ] \quad (3.1)$$

where  $P_{probe}(t)$  is the probe beam power (averaged over a time interval much longer than the pulse repetition time), which varies with time  $t$  as the laser power fluctuates.  $R_0$  is the unperturbed reflectance, and  $\Delta R$  is the reflectance change induced by the pump, which depends on the delay time  $\tau$  between pump and probe and on the average laser power at time  $t$ .  $\Delta R(t; \tau)$  can be related to the pump power by  $\Delta R(t; \tau) = P_{pump}(t) [\eta_{nonvib}(\tau) + \eta_{vib}(\tau)]$ , where  $\eta_{nonvib}(\tau)$  and  $\eta_{vib}(\tau)$  are respectively the non-vibrational and vibrational responses of the sample at a delay time  $\tau$ . Considering the power fluctuation noise,  $n(t)$ , of a laser with average power  $\langle P_{laser} \rangle$ ,  $P_{probe}(t)$  can be written as  $P_{probe}(t) = \alpha [\langle P_{laser} \rangle +$

$n(t)$ ]. The pump power is proportional to  $P_{probe}(t)$ , but modulated with a square wave form  $sw(\omega_c t)$ :

$$P_{pump}(t) = \beta [<P_{laser}> + n(t)] \times sw(\omega_c t) \quad (3.2)$$

where  $\omega_c$  is the chopping frequency.  $\alpha$  and  $\beta$  are constants. Thus we can rewrite Eq. (3.1) as

$$\begin{aligned} P_{sig}^A(t; \tau) = & \alpha [<P_{laser}> + n(t)] R_0 \\ & + \alpha \beta [<P_{laser}> + n(t)]^2 sw(\omega_c t) \eta_{nonvib}(\tau) \\ & + \alpha \beta [<P_{laser}> + n(t)]^2 sw(\omega_c t) \eta_{vib}(\tau) \end{aligned} \quad (3.3)$$

The only term which contains the surface mode information is the third term on the right hand side of (3.3). The first term is the unperturbed reflected probe beam when the pump is absent. It is not modulated by  $sw(\omega_c t)$ , and thus is rejected by the lock-in amplifier (except the frequency component of  $n(t)$  at  $\omega_c$ ). However, in the conventional pump-probe scheme, the second term, which manifests itself as the sharp rising edge and the slowly-decaying tail in Fig. 3-4 (a), passes through the balanced detectors and is amplified by the lock-in amplifier. Thus the laser fluctuation in this term (within the bandwidth of the low-pass filter in the lock-in amplifier) stays and contributes to the total noise. In the lock-in amplifier, this  $P_{sig}^A$  is multiplied by a reference at  $\omega_c$  and filtered by a low-pass filter  $\tilde{H}_L(j\omega)$ [3.8]. In the frequency domain, omitting high-order terms, the signal becomes

$$\begin{aligned} \tilde{P}(\omega) = & F\{P_{sig}^A(t; \tau) \cos(\omega_c t)\} \tilde{H}_L(j\omega) \\ \cong & \alpha \beta <P_{laser}>^2 [\eta_{nonvib}(\tau) + \eta_{vib}(\tau)] \mathcal{X}(\omega) \tilde{H}_L(0) \\ & + \alpha R_0 \tilde{N}(\omega - \omega_c) \tilde{H}_L(j\omega) \end{aligned}$$

$$\begin{aligned}
& + 2\alpha \beta \langle P_{laser} \rangle \eta_{nonvib}(\tau) \tilde{N}(\omega) \tilde{H}_L(j\omega) \\
& + 2\alpha \beta \langle P_{laser} \rangle \eta_{vib}(\tau) \tilde{N}(\omega) \tilde{H}_L(j\omega)
\end{aligned} \tag{3.4}$$

where  $F\{\}$  represents the Fourier transform operator,  $\tilde{N}(\omega)$  is the Fourier transform of  $n(t)$ . The first term on the right is the clean signal, and the second to the fourth terms are the noise. For our samples,  $R_0 \sim 100 \beta \langle P_{laser} \rangle \eta_{nonvib}$ . But the fluctuation noise  $\tilde{N}(\omega)$  shows a  $(1/\omega)^x$  roll-off (usually,  $x > 1$ ) in typical cw mode-locked lasers[3.10]-[3.12]. So the noise term centered at  $\omega_c$  (i.e., the second term on the right of Eq. (3.4)) can be efficiently suppressed by modulating at high frequencies. Therefore the third term,  $2\alpha \beta \langle P_{laser} \rangle \eta_{nonvib}(\tau) \tilde{N}(\omega) \tilde{H}_L(j\omega)$ , becomes the dominant noise.

To see how the two-pump scheme works, let's write down the expression for the signal generated by a delayed pump B:

$$\begin{aligned}
P_{sig}^B(t; \tau + \tau_{AB}) &= \alpha [\langle P_{laser} \rangle + n(t)] R_0 \\
&+ \alpha \beta [\langle P_{laser} \rangle + n(t)]^2 sW(\omega_c t + \pi) \eta_{nonvib}(\tau + \tau_{AB}) \\
&+ \alpha \beta [\langle P_{laser} \rangle + n(t)]^2 sW(\omega_c t + \pi) \eta_{vib}(\tau + \tau_{AB})
\end{aligned} \tag{3.5}$$

Note that the phase of modulation is shifted by  $180^\circ$ . The total signal is the sum of  $P_{sig}^A(t; \tau)$  and  $P_{sig}^B(t; \tau + \tau_{AB})$

$$\begin{aligned}
P_{total} &= P_{sig}^A(t; \tau) + P_{sig}^B(t; \tau + \tau_{AB}) \\
&= 2\alpha [\langle P_{laser} \rangle + n(t)] R_0 \\
&+ \alpha \beta [\langle P_{laser} \rangle + n(t)]^2 [\eta_{nonvib}(\tau) + \eta_{vib}(\tau)] sW(\omega_c t) \\
&+ \alpha \beta [\langle P_{laser} \rangle + n(t)]^2 [\eta_{nonvib}(\tau + \tau_{AB}) + \eta_{vib}(\tau + \tau_{AB})] sW(\omega_c t + \pi)
\end{aligned} \tag{3.6}$$

Analogous to Eq. (3.4), the output signal of the lock-in amplifier in the frequency domain



is

$$\begin{aligned}
\tilde{P}(\omega) &= F\{P_{total} \cos(\omega_c t)\} \tilde{H}_L(j\omega) \\
&\cong \alpha \beta \langle P_{laser} \rangle^2 [\Delta\eta_{nonvib}(\tau) + \Delta\eta_{vib}(\tau)] \delta(\omega) \tilde{H}_L(0) \\
&\quad + 2\alpha R_0 \tilde{N}(\omega - \omega_c) \tilde{H}_L(j\omega) \\
&\quad + 2\alpha \beta \langle P_{laser} \rangle \Delta\eta_{nonvib}(\tau) \tilde{N}(\omega) \tilde{H}_L(j\omega) \\
&\quad + 2\alpha \beta \langle P_{laser} \rangle \Delta\eta_{vib}(\tau) \tilde{N}(\omega) \tilde{H}_L(j\omega)
\end{aligned} \tag{3.7}$$

where  $\Delta\eta(\tau)$  is the difference between  $\eta(\tau)$  and  $\eta(\tau + \tau_{AB})$ . Similar to Eq. (3.4), the last three terms are the noise. For a small  $\tau_{AB}$ ,  $\Delta\eta$  is the finite-difference approximation to  $\left(\frac{d\eta}{d\tau}\right)\tau_{AB}$ . Since the non-vibrational response  $\eta_{nonvib}(\tau)$  is a slowly varying function (for  $\tau$  greater than a few hundred femtoseconds),  $d\eta_{nonvib}/d\tau$  is very small and so  $\Delta\eta_{nonvib}$  is almost zero. The third term on the right of Eq. (3.7) (corresponding to the dominant noise in the single-pump scheme) is thus greatly suppressed and no longer dominates. Figure 3-7 shows the noise power spectrum of the lock-in amplifier output (at a fixed delay time  $\tau \sim 7$  ps) spanning from 0.1 to 500 Hz. A 10 to 20 dB noise suppression throughout this frequency range was obtained by using the alternating-pump technique.

An extra advantage of our alternating-pump technique is that we can selectively reveal the weaker lower-frequency mode (the 1<sup>st</sup> gap) by canceling the higher-frequency mode (the 2<sup>nd</sup> gap), and thus attain a higher measurement accuracy of the lower-mode frequency,  $\nu_1$ . To demonstrate this, we compare the Fourier transform of the derivatives of  $\Delta R(\tau)$  acquired using the two different methods (see Fig. 3-8). The ultrafast transient

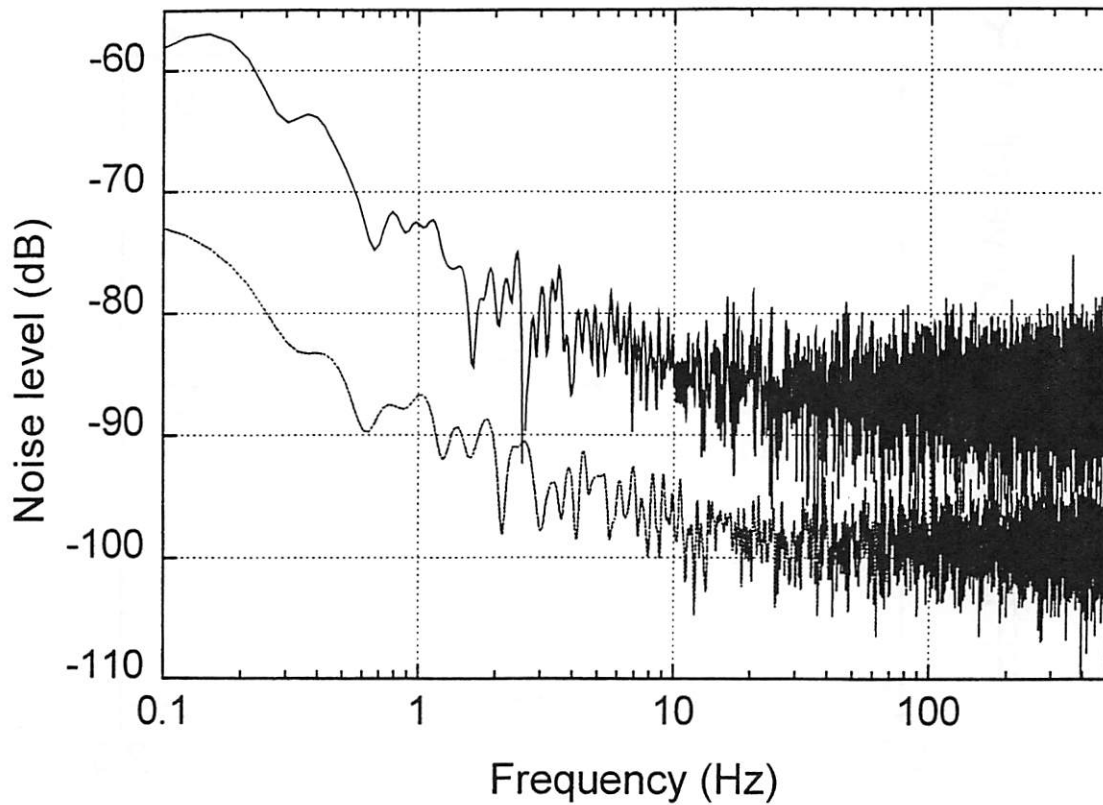


Figure 3-7 Noise power spectra of the lock-in amplifier output at a fixed time delay  $\tau \sim 7$  ps using the conventional scheme (solid line) and the 2-pump scheme (dotted line).

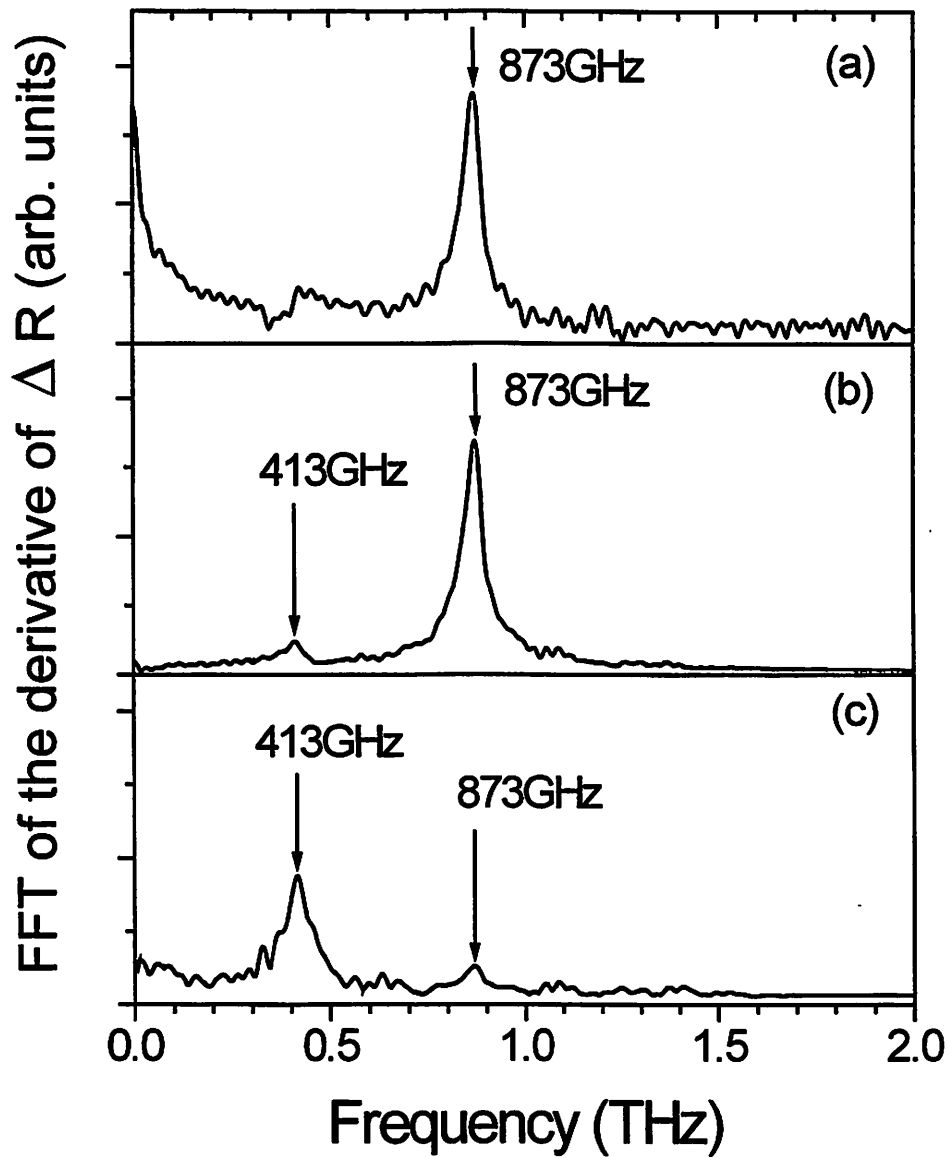


Figure 3-8 Comparison of the Fourier transform of  $d\Delta R(\tau)/d\tau$  using (a) the conventional scheme, (b) the alternating-pump scheme with  $\tau_{AB} = 0.57$  ps and (c)  $\tau_{AB} = 1.14$  ps. ( $d = 6.84$  nm,  $\Gamma \approx 0.5$ ).

behavior in the first 2 ps was trimmed off before taking a Fourier transform to avoid a broad-band background on the spectrum. It is evident that the spectra in Fig. 3-8 (b) and (c) (two-pump scheme) are much cleaner than that in Fig. 3-8(a) (conventional scheme) and have a much lower dc component. In particular, the lower-frequency mode cannot be clearly discerned in 3-8(a), while in 3-8(b), it is undoubtedly observed, and in 3-8(c), by canceling the other mode, it is more explicitly revealed. These two vibration modes of frequencies at 413 and 873 GHz are the localized surface modes in the first (zone-boundary), and the second (zone-center) gaps, respectively. All of our samples show simultaneous presence of these two surface modes. The reason why the second-gap mode is stronger than the first-gap mode might be that, due to the spatial form of the initial stress or the sensitivity function, the latter is less strongly excited and/or detected[3.13]-[3.14]. It is worth mentioning that, besides the benefits that have been pointed out, this technique is also more efficient in laser power utilization. Because both the zeroth- and the first-order diffracted beams from the AO modulator are used, whereas in the conventional scheme only the first-order beam is used, which is less than 50% of the total laser power.

The principle of this technique can be applied in general to other multilayer thin-film structures, to improve the sensitivity for probing surface modes. In the next chapter, more experimental results obtained using this alternating-pump technique will be described in detail and compared to the theory in Chapter 2.

## References

- [3.1] C. Thomsen, H.T. Grahn, H.J. Maris, and J. Tauc, *Physical Review*, **B 34**, 4129 (1986).
- [3.2] J.E. Rothenberg, *Optics Letters*, **13**, 713 (1988).
- [3.3] O.B. Wright and K. Kawashima, *Physical Review Letters*, **69**, 1668 (1992).
- [3.4] B. Perrin, B. Bonello, J.-C. Jeannet, and E. Romantet, *Progress in Natural Science*, **6**, S-444 (1996).
- [3.5] D.E. Spence, P.N. Kean, W. Sibbet, *Optics Letters*, **16**, 42 (1991).
- [3.6] A. Yariv, *Optical Electronics*, 4<sup>th</sup> ed., Saunders College Publishing, Philadelphia, 1991, p. 204.
- [3.7] Derived from the data in *Landolt-Bornstein Numerical Data and Functional Relationships in Science and Technology*, Springer-Verlag, Berlin-Heidelberg, 1985, New Series, **III/15b**, p. 252. For Mo,  $n = 3.46$ ,  $\kappa = 3.65$  at 1.55 eV. Absorption length =  $\lambda_0 / 4\pi\kappa$ , where  $\lambda_0$  is the optical wavelength in vacuum.
- [3.8] M.L. Meade, *Lock-in Amplifiers: Principles and Applications*, Peter Peregrinus Ltd., London UK, 1983.
- [3.9] B. Bonello, B. Perrin, and C. Rossignol, *Journal of Applied Physics*, **83**, 3081 (1998).
- [3.10] M.C. Nuss, U. Keller, G.T. Harvey, M.S. Heutmaker, and P.R. Smith, *Optics Letters*, **15**, 1026 (1990).
- [3.11] U. Keller, C.E. Socolich, G. Sucha, M.N. Islam, and M. Wegener, *Optics Letters*, **15**, 974 (1990).
- [3.12] L. Hollberg, M. Long-Sheng, M. Hohenstatt, and J.L. Hall, *Proceedings of SPIE*,

vol. **426**, p.91, 1983.

[3.13] W. Chen, Y. Lu, H.J. Maris and G. Xiao, *Physical Review*, **B 50**, 14506 (1994).

[3.14] B.Perrin, B.Bonello, J.C.Jeannet and E.Romatet, *Physica*, **B 219&220**, 681 (1996).

# Chapter 4. Experimental Results

Picosecond ultrasonics has the potential of being a useful noncontact, nondestructive evaluation (NDE) tool for EUV multilayer characterization. Using our alternating-pump technique described in chapter 3, we successfully excited and detected at least two surface modes lying within the lowest two frequency gaps. The frequencies of these surface modes depend both on  $d$  and  $\Gamma$  as described in Chapter 2, and can be used to extract these two parameters. In this chapter, we demonstrate several practical examples of applying this technique to nondestructive characterization of Mo/Si multilayers. The non-vibrational part of the material response will also be discussed in detail. In addition, the issue of laser damage to coatings caused by the pump and probe laser beams was also studied, and found to be negligible given our data-acquisition time.

## 4.1 Study of the thickness dependence of surface modes

### 4.1.1 $d$ -dependence of vibration frequencies

It is easy to see the relationship between surface-mode frequencies  $\nu_n$  ( $n$  is the index for a frequency gap.  $n = 1, 2, 3, \dots$ ) and the coating period  $d$  if we rewrite Eq. (2.38) as

$$\frac{\rho_1 c_1}{\rho_2 c_2} \tan\left(\frac{2\pi\nu_n d(1-\Gamma)}{c_1}\right) + \tan\left(\frac{2\pi\nu_n d\Gamma}{c_2}\right) = 0 \quad (4.1)$$

For a fixed  $\Gamma$  ratio,  $\nu_n d$  is a constant for each mode  $n$ . And so surface-mode frequencies  $\nu_n$  are inversely proportional to the bilayer thickness  $d$ , assuming an ideal 2-sublayer system. Figure 4-1 displays the derivative of  $\Delta R(\tau)$  traces measured by our alternating-

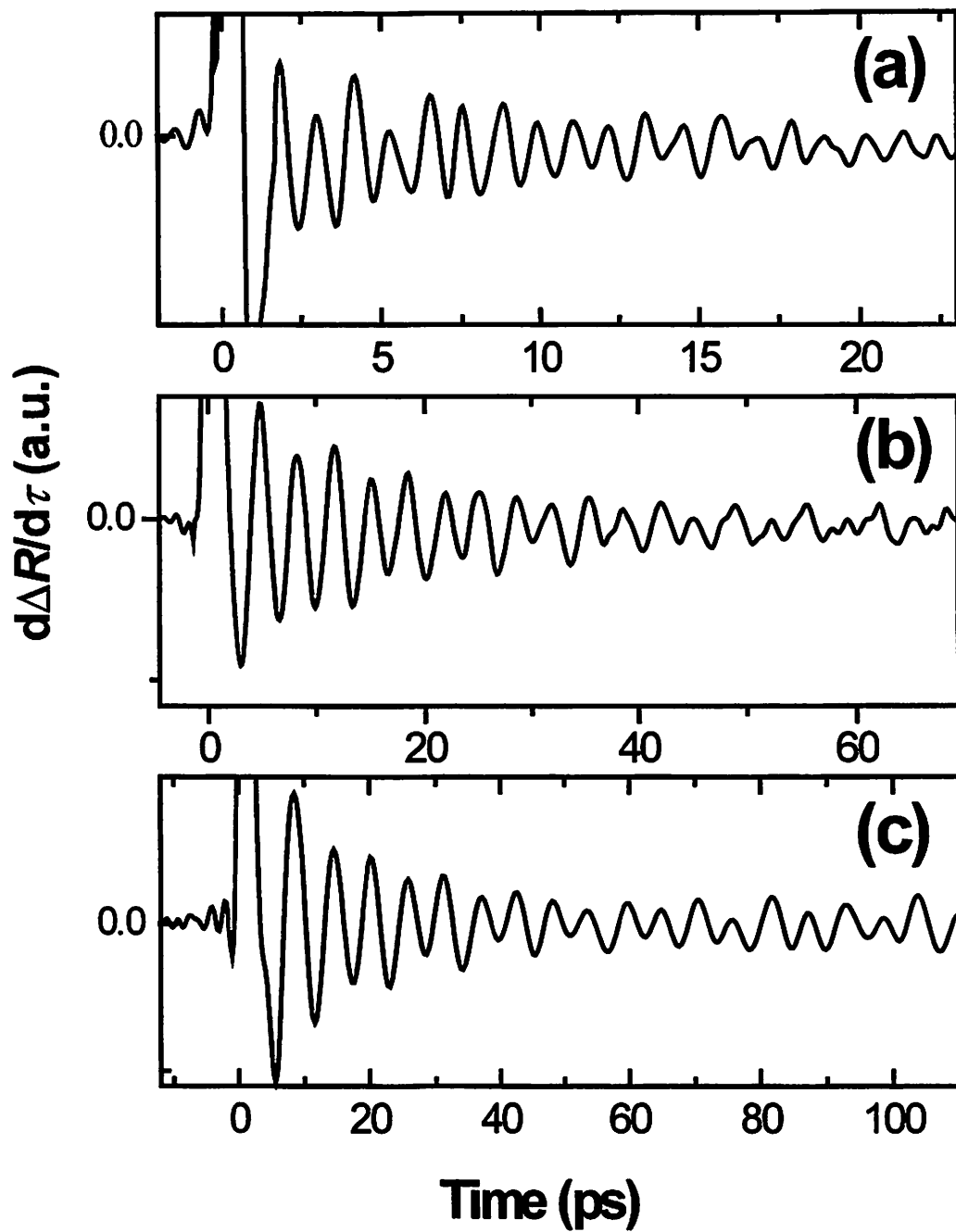


Figure 4-1 The derivative of  $\Delta R(\tau)$  measured by the alternating-pump technique for  $d =$   
(a) 6.84, (b) 19.55, and (c) 32.56 nm.



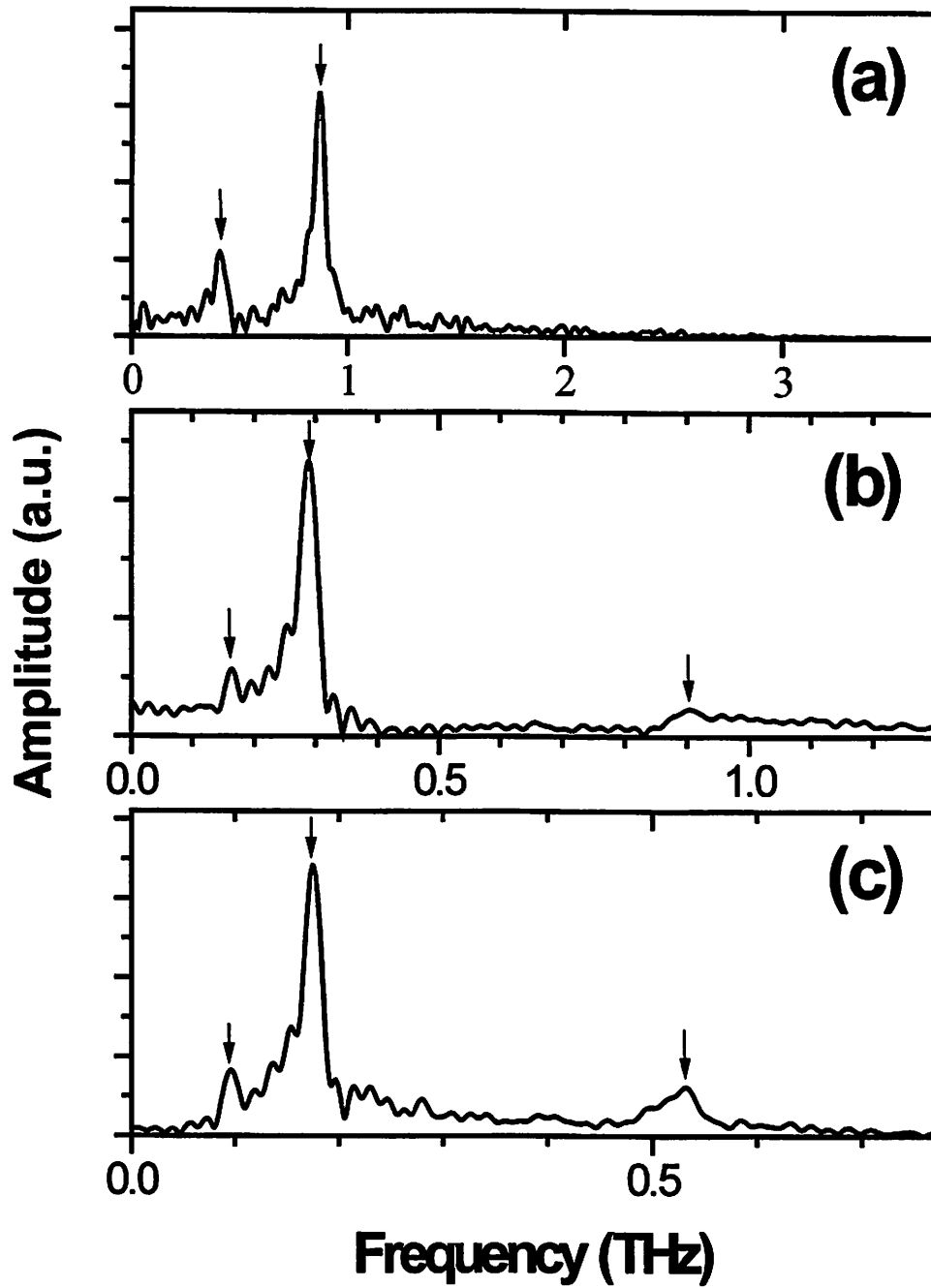


Figure 4-2 Fourier transform of  $d\Delta R(\tau)/d\tau$  for  $d =$  (a) 6.84, (b) 19.55, and (c) 32.56 nm.

pump technique for samples with various  $d$ : 6.84, 19.55 and 32.56 nm. (We took derivative of  $\Delta R$  to remove the residual non-vibrational signal.) These  $d$  values were determined by grazing incidence x-ray diffraction with an accuracy within 0.1%. Fig. 4-2 shows their corresponding vibration spectra. In all of these samples, we observed the 1<sup>st</sup>-gap and 2<sup>nd</sup>-gap surface modes. In addition to these two modes, a higher-order surface mode was clearly seen in samples with  $d = 32.56$  and 19.55 nm. The amplitude of this mode decreases rapidly as  $d$  is reduced from 32.56 nm to 19.55 nm and it becomes unobservable in the thinnest sample ( $d = 6.84$  nm) within our detection sensitivity. Theoretical calculation indicates that it is the surface mode in the 6<sup>th</sup> gap of the longitudinal acoustic (LA) phonon dispersion curve.

The theoretical and measured values of the surface-mode frequencies  $\nu_1$ ,  $\nu_2$ , and  $\nu_6$

**Table 4-1** List of surface-mode frequencies in the 1<sup>st</sup>, 2<sup>nd</sup>, and 6<sup>th</sup> gaps determined by both theory ( $\nu_{1th}$ ,  $\nu_{2th}$ , and  $\nu_{6th}$ ) and experiment ( $\nu_{1exp}$ ,  $\nu_{2exp}$ , and  $\nu_{6exp}$ ) for samples with  $\Gamma = 0.5$ . Also listed is the relative strength of the 2<sup>nd</sup>-gap mode ( $\Delta R_{\nu_2}/R_0$ ).

$d$ (nm)	$\nu_{1th}$ (GHz)	$\nu_{2th}$ (GHz)	$\nu_{6th}$ (GHz)	$\nu_{1exp}$ (GHz)	$\nu_{2exp}$ (GHz)	$\nu_{6exp}$ (GHz)	$\Delta R_{\nu_2}/R_0$ ( $\times 10^{-5}$ )
32.56	103	194	584	94	179	532	1.94
19.55	172	323	972	158	298	904	1.86
6.84	491	923	2780	413	873	–	0.66

for all of our samples are listed in Table 4-1. The measured frequencies of surface modes are inversely proportional to the bilayer thickness with an error of less than 5%. The theoretical and experimental frequencies agree to within 16% in all of the samples. There are many possible explanations for this discrepancy: (1) The uncertainty of the density and sound velocity in the materials. For the moment, we take the values for bulk, crystalline Si and Mo:  $\rho_{Si} = 2.33 \text{ g/cm}^3$ ,  $c_{Si} = 6.9 \times 10^5 \text{ cm/sec}$ ,  $\rho_{Mo} = 10.22 \text{ g/cm}^3$ , and  $c_{Mo} = 6.2 \times 10^5 \text{ cm/sec}$ . Transmission electron microscopy indicates that the Si layers are amorphous and the Mo layers are polycrystalline[4.1]-[4.2]. Thus they might have different properties from crystalline materials. In addition, it is known that the elastic properties in a thin multilayer film might deviate from the bulk values[4.3]-[4.4]. (2) The silicide interlayers formed at Mo/Si interfaces smear the originally abrupt interfaces[4.2] and thus the assumption of perfectly abrupt interfaces in our calculation is unrealistic. (3) Surface silicon dioxide can also modify the surface-mode frequencies, as discussed in §2.3. (4) During deposition of Mo/Si multilayers, a compressive stress arises in Si layers, and a tensile stress is found in Mo layers[4.5]. These stresses can affect the elastic properties of each layers.

#### **4.1.2 Vibration amplitudes of surface modes**

Also shown in Table 4-1 is the ratio of the initial reflectance change due to the second-gap surface mode ( $\Delta R_{\nu_2}$ ) to the unperturbed reflectance ( $R_0$ ), which shows a rapid drop as the bilayer thickness reduces to 6.84 nm. There are several possible explanations for this trend: (1) The light energy first absorbed by carriers takes a certain time to be transferred to phonons, so the generation of high-frequency vibrations will be suppressed. (2) In a multilayer with a smaller layer thickness, some carriers can diffuse relatively

farther from Mo into Si. Hence the difference in the energy deposition and in the stress between adjacent Mo and Si layers will be reduced. (3) For the thinnest sample, the silicide interlayers fill ~22% of the bilayer thickness (the silicide thickness is ~ 1.0 nm for Mo-on-Si interfaces, and ~ 0.5 nm for Si-on-Mo interfaces[4.2]) and severely soften the acoustic impedance mismatch between Si and Mo layers. Thus the reflectance of sound waves at the interfaces is reduced.

For a given sample, the amplitude for each surface mode is related to the spatial form of the initial stress  $\sigma(z, \tau = 0)$  and the shape of the “sensitivity function”  $f(z)$  (the contribution to  $\Delta R$  due to a strain at a depth  $z$ ). The former determines the relative strength of excitation for each mode, and the latter determines how strongly a mode will be detected optically. Using a computational simulation to be discussed in the next chapter, we can calculate the excited and optically-detectable vibration amplitude of each surface mode. But actually a simple argument suffices to interpret the observed results. The initial stress  $\sigma(z, \tau = 0)$  is proportional to the amount of absorbed optical energy  $U(z)$ . Since Mo layers have a much higher absorption coefficient than Si layers, we can neglect the absorption in Si and write the optically deposited energy  $U(z)$  (see Fig. 5-2) as

$$U(z) = \begin{cases} A \cdot sw(d, \Gamma) \cdot \exp(-\Gamma z / \zeta) & z \geq 0 \\ 0 & z < 0 \end{cases}$$

where  $A$  is a constant,  $\zeta$  is the absorption length in Mo, and  $sw(d, \Gamma)$  is a periodic square wave which equals 1 in Mo layers and 0 in Si layers. The sensitivity function  $f(z)$  in general also has a similar spatial form

$$f(z) = \begin{cases} B \cdot [sw(d, \Gamma) + C] \cdot g(z) & z \geq 0 \\ 0 & z < 0 \end{cases}$$

where  $B$  and  $C$  are constants.  $g(z)$  is the envelope for the square wave and looks like an exponentially damped oscillation (see Fig. 5-3 for example). Now,  $sw(d, \Gamma)$  can be expanded into Fourier series:

$$sw(d, \Gamma) = c_0 + \sum_{m=1}^{\infty} c_m \sin\left(\frac{2\pi mz}{d}\right)$$

with coefficients

$$c_m = \frac{2}{d} \int_0^d sw(d, \Gamma) \sin\left(\frac{2\pi mz}{d}\right) dz \quad m = 1, 2, 3, \dots$$

Note that all of the even order (except  $m = 0$ ) coefficients vanish for  $\Gamma = 0.5$  due to symmetry of the problem. So the Fourier transforms of  $\sigma(z, \tau = 0)$  and  $f(z)$  have peaks at certain spatial frequencies  $k_m = m(2\pi/d)$  with  $m = 0, 1, 3, 5, \dots$ , and the spectral width of each peak is determined by the envelope functions. An inspection of the stress distribution in Fig. 2-4 suggests that the stress profile of each surface mode  $n$  is approximately a damped oscillation with a period of  $2d/n$  and a decay length  $l_n$ :

$$\sigma_n(z) \approx s \cdot \sin\left(\frac{\pi nz}{d}\right) \exp(-z/l_n) \quad n = 1, 2, 3, \dots$$

where  $s$  is a constant. Note that the periodicity of  $\sigma_n(z)$  corresponds to the boundary of the  $n$ th Brillouin zone:  $k_n = n\pi/d$ . In order to be significantly excited and detected, this spatial frequency  $k_n$  has to be equal to one of the  $k_m$ 's. Therefore,  $n$  should be 2, 6, 10, ... ( $m = 1, 3, 5, \dots$ ). However,  $|c_m|$  is roughly proportional to  $(1/m)$ , so the 2<sup>nd</sup>-gap mode is the strongest, and higher order modes with  $n \geq 10$  have less chance of being excited. Also, higher frequency modes in general have higher damping rate [4.6] and thus

are more difficult to be observed. Another reason why we did not observe modes  $n > 6$  is probably because of the limited temporal resolution of our detection system. Large damping and limited resolution at higher frequencies, together with the three reasons that cause  $\Delta R_{1/2}/R_0$  to decrease (on page 64) in thinner samples also explain the gradual disappearance of the  $n = 6$  mode when  $d$  becomes smaller.

According to our simple argument, the surface mode  $n = 1$  could hardly be excited if the spectral widths of the peaks in  $\sigma(z, \tau = 0)$ ,  $f(z)$ , and  $\sigma_n(z)$  were narrow. However, these functions all have finite-width envelopes which broaden the peaks. In particular, the decay length for this mode is very short:  $l_1 \sim d$  (see Fig. 2-4(a)), which gives a very wide width in the  $k$ -space:  $\Delta k_z \sim 2\pi/d$ , and thus the convolution of  $\sigma_1(z)$  with  $\sigma(z, \tau = 0)$  or with  $f(z)$  yields a moderate number. In addition, the damping rate of this mode is the lowest among all surface modes, and so it is easier to be detected.

## 4.2 Thickness profile measurement

In a series of test measurements for reproducibility, the standard deviation of the measured vibration frequencies (for  $d \sim 6.9$  nm and,  $\Gamma \sim 0.5$ ) was found to be 0.16%. With this precision, we then successfully mapped the thickness variation profile of a linearly graded Mo/Si multilayer sample with a 2%  $d$ -variation from two edges to the center. The geometry of the sample is shown on the top of Fig. 4-3. A visible defective region on the sample is shown as the shaded area. The peak frequency of the 2<sup>nd</sup>-gap mode,  $\nu_2$ , as a function of position ( $z$ ) on the sample is shown on the bottom of Fig. 4-3. Figure 4-4 displays the normalized vibration spectra around  $\nu_2$  measured at different

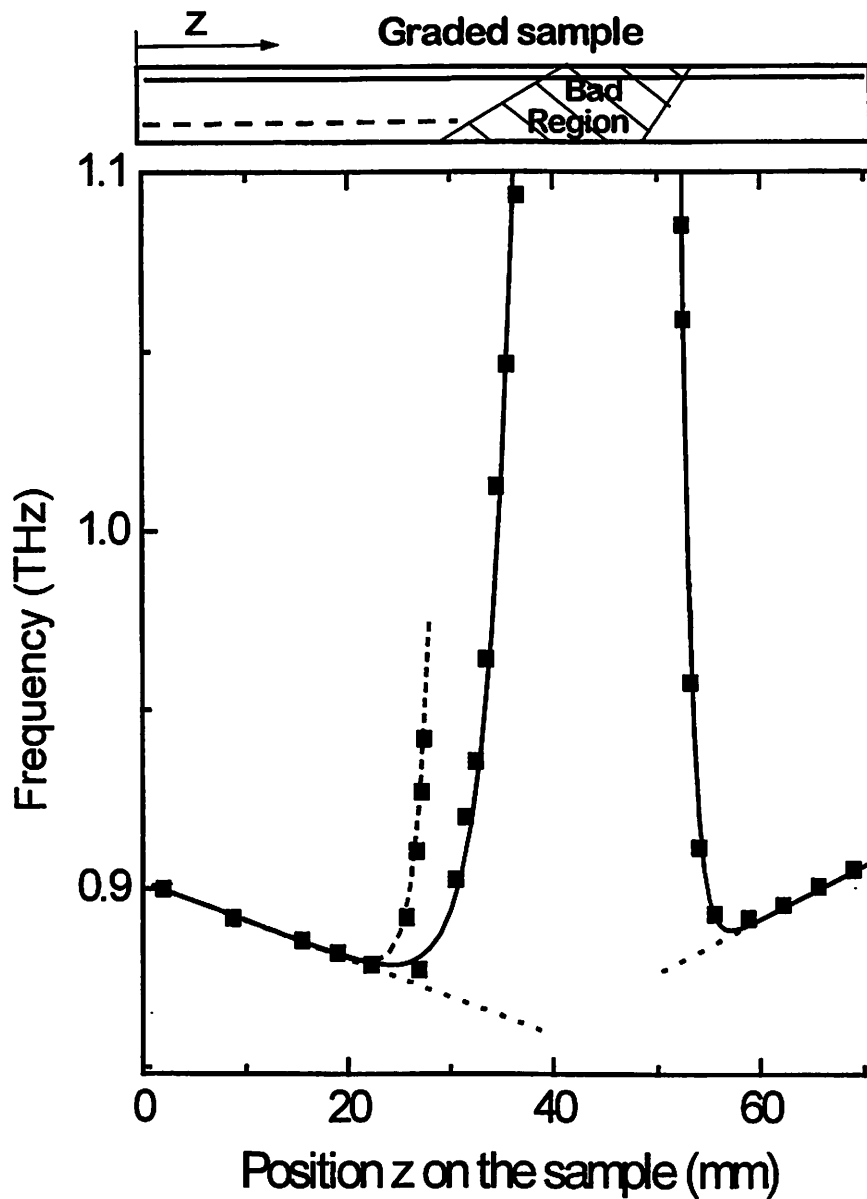


Figure 4-3 Top: The geometry of the graded sample. Bottom: peak frequency  $\nu_2$  as a function of position. (Solid/dashed lines: data measured along the solid/dashed lines on the sample.) The shaded area on the sample is a defective region where no vibrations were detected. Away from this region,  $\nu_2$  varies linearly with  $z$ , as expected for a linearly graded multilayer.

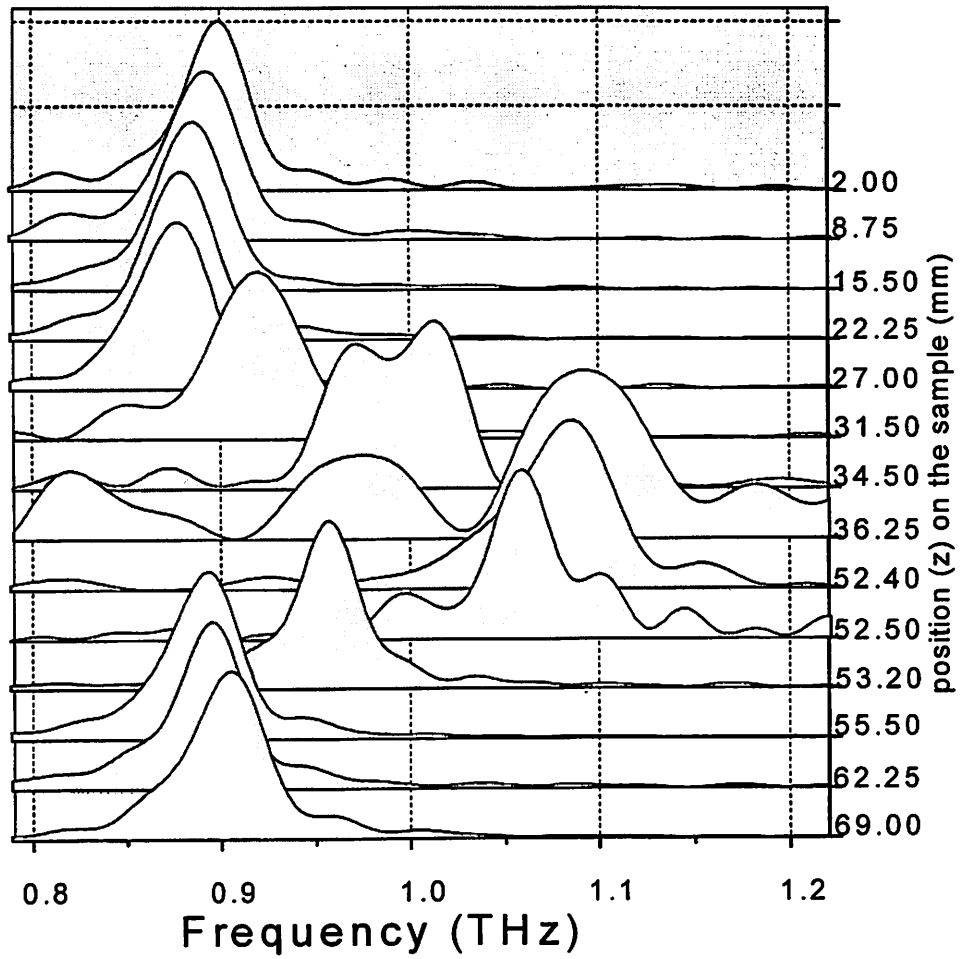


Figure 4-4 The spectra (amplitude) of the surface modes at different z positions on a graded sample.



spots on the sample (along the solid line on Fig. 4-3). Since we know that  $d$  is the dominating variable, and that  $\nu_n$  is inversely proportional to  $d$  for each mode, we only need to measure either  $\nu_1$  or  $\nu_2$ . In Fig. 4-3,  $\nu_2$  decreases (i.e.  $d$  increases) linearly from two edges toward the center except near the boundary of a defective region around the center, where  $\nu_2$  increases drastically, indicating an abrupt drop in the coating thickness. In Fig. 4-4, we can see that, near the defective region, the signal-to-noise ratio decreases, which is a result of a weaker excitation of the surface modes. In addition, the peaks are wider, indicating a shorter decay time of vibrations. These features imply some kind of imperfection on the surface or interfaces. No vibrations were detected within the defective region.

### 4.3 $\Gamma$ -dependence of the surface-mode frequencies

Apparently, in order to simultaneously extract the two parameters  $d$  and  $\Gamma$ , we need the data of at least two surface modes. It is evident from Eq.(4.1) that, for each mode  $n$ , the product  $\nu_n d$  is a constant for a fixed  $\Gamma$ . Therefore,  $\nu_n$  can be written as:

$$\nu_n = d^{-1} f_n(\Gamma) \quad (4.2)$$

where  $f_n(\Gamma)$  is the functional dependence of  $\nu_n$  on  $\Gamma$ , and is apparently different for each mode. The ratio of the frequencies of any two modes is thus given by:

$$\frac{\nu_m}{\nu_n} = \frac{f_m(\Gamma)}{f_n(\Gamma)} \equiv g_{mn}(\Gamma) \quad (4.3)$$

where  $g_{mn}$  is another function of  $\Gamma$  only, independent of  $d$ . Consequently, small  $\Gamma$ -variation can be mapped if we simultaneously measure the frequencies of any two surface

modes across the sample and plot the ratio of them. In this way, we can separate the effects of  $d$ - and  $\Gamma$ -variation if we simultaneously detect two surface modes in a multilayer. For all of our Mo/Si multilayer samples, modes  $n = 1$  and 2 were always observed. So by carefully studying the  $\Gamma$ -dependence of their frequencies, we should be able to extract the  $\Gamma$  value for arbitrary samples.

The dependence of functions  $f_1$ ,  $f_2$ , and  $g_{21}$  on  $\Gamma$  was studied both theoretically and experimentally. Multilayer samples with  $d = 6.9$  nm and  $\Gamma$  varying from 0.3 to 0.7 were investigated. These  $\Gamma$  values were determined by the product of deposition time and calibrated deposition rate for both materials, and so the effect of contraction due to silicide formation[4.2] was not included. The measured surface mode frequencies  $\nu_1$  and  $\nu_2$  as a function of  $\Gamma$  are shown in figure 4-5(a) (solid squares), in comparison with theoretical curves (solid lines) predicted by Eq.(4.1). These curves show the functional dependence on  $\Gamma$ ,  $f_n(\Gamma)$ , given that  $d$  is fixed. Note that  $f_1(\Gamma)$  and  $f_2(\Gamma)$  have opposite trends, which is advantageous since it enhances the slope for  $g_{21}(\Gamma)$ , and thus facilitates the characterization of  $\Gamma$ -variation. Theoretical and measured values of  $g_{21}$  are plotted as a function of  $\Gamma$  in Fig. 4-5(b). Although there is a slight mismatch between the two curves, they show the same tendency to descend as  $\Gamma$  increases. This mismatch between the theory and the real data might be due to the same factors mentioned in §4.1, such as the uncertainty of the material parameters, the formation of silicide interlayers, and surface oxidation. Despite this mismatch, for characterization purposes, we can use the empirical data points measured from these 5 samples as our reference, and read out the  $\Gamma$  value by interpolation between points.

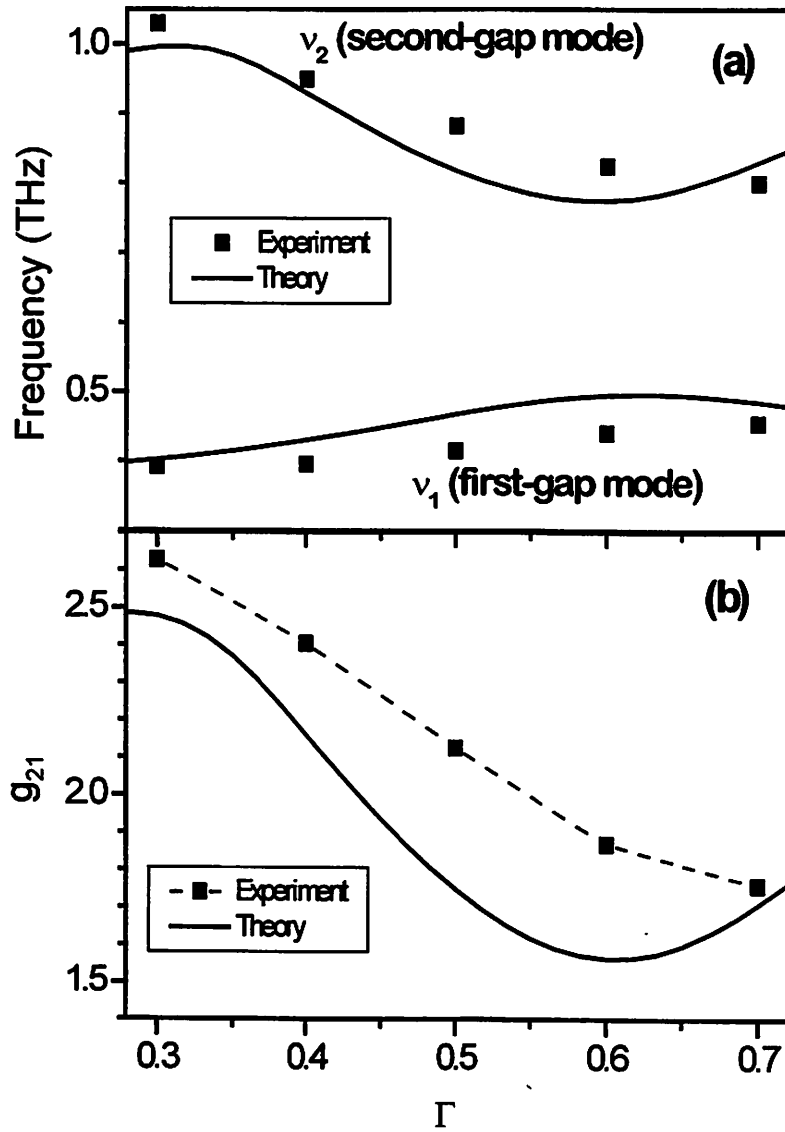


Figure 4-5 (a) The vibration frequencies of the two surface modes vs.  $\Gamma$  ( $d = 6.9$  nm). (b)

$g_{21}$  (the ratio  $\nu_2/\nu_1$ ) as a function of  $\Gamma$ . The solid lines are the theoretical predictions, and the filled squares are the measured values.

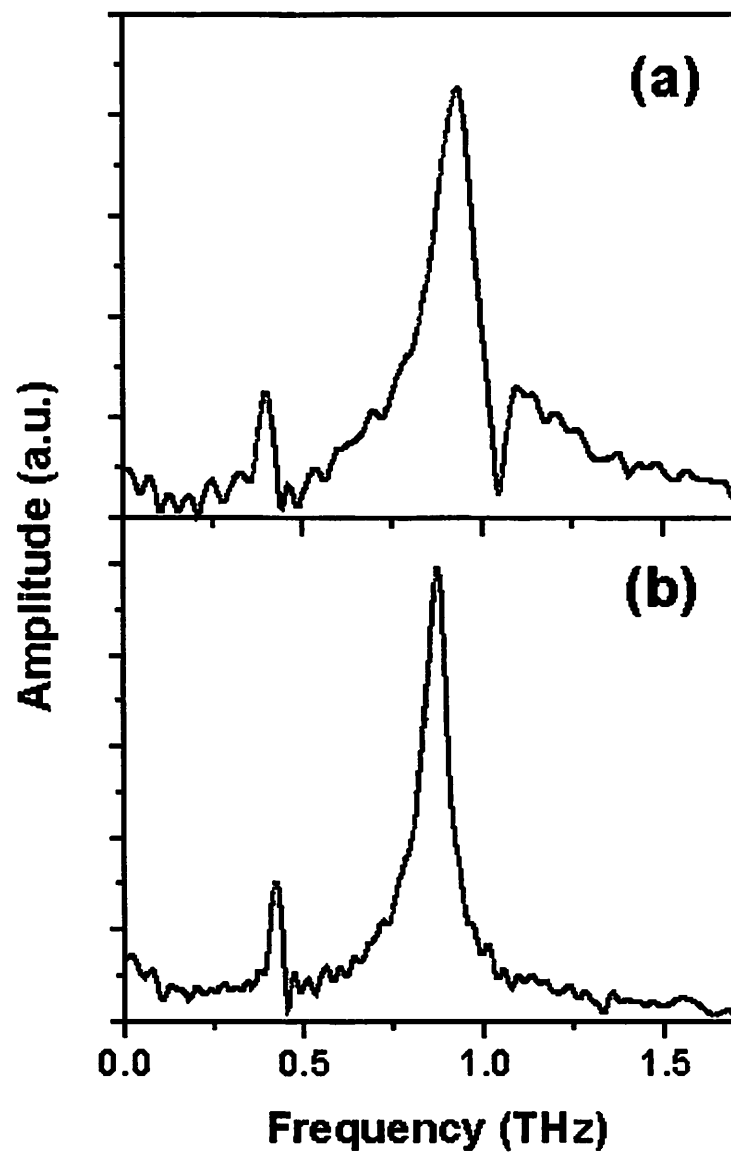


Figure 4-6 Comparison of the vibration spectra for (a)  $\Gamma = 0.4$  and (b)  $\Gamma = 0.5$ .

#### 4.4 Simultaneous extraction of $d$ and $\Gamma$

We have shown in §4.3 that the frequency ratio  $g_{21}$  is a function of  $\Gamma$  only, independent of  $d$ . Thus  $\Gamma$  can be uniquely determined by  $g_{21}$  if they have one-to-one correspondence. Although the theoretical curve on Fig. 4-5(b) is not one-to-one, fortunately the experimental curve (dashed line) seems to be, at least for  $\Gamma$  near 0.4. The precision of  $\Gamma$  extraction depends on the measurement reproducibility of the peak frequencies  $\nu_1$  and  $\nu_2$ , which is related to the spectral line widths of these modes. Figure 4-6 (a) and (b) compare the measured vibration spectra for samples with  $\Gamma = 0.4$  and  $\Gamma = 0.5$  (both have  $d = 6.9\text{nm}$ ), respectively. Clearly the one with  $\Gamma = 0.4$  has a broader peak and a more complicated line shape for the second mode. The physical reason for this complex line shape will be discussed later. But for the characterization purpose, we are more concerned about the wider linewidth, which deteriorates the measurement precision for the peak frequency  $\nu_2$ . For this sample, the standard deviation for peak frequencies  $\nu_1$  and  $\nu_2$  is found to be 0.15% and 0.39%, respectively. The combined error for  $g_{21}$  is  $\pm 0.54\%$ , which corresponds to an absolute error of  $\Delta\Gamma \sim \pm 0.005$  at  $\Gamma = 0.4$ , according to the experimental data in Fig. 4-5(b). Currently, there is no other non-destructive method that offers this precision for  $\Gamma$ -measurement.

Once  $\Gamma$  is obtained,  $d$  can be found using a simple relationship

$$d / d_{ref} = \nu_n(d_{ref}, \Gamma) / \nu_n \quad (4.4)$$

where  $n = 1$  or  $2$ ,  $d_{ref}$  is the bilayer thickness of the reference wafers in Fig. 4-5, and

$\nu_n(d_{ref}, \Gamma)$  is the interpolated surface-mode frequency at the determined  $\Gamma$  value for  $d = d_{ref}$  (using the reference data points in Fig. 4-5(a)). Five data points are too sparse indeed for an accurate estimate using interpolation, but it suffices for our preliminary trial for evaluation purposes.

To evaluate the utility of our technique, the coating team at Lawrence Livermore National Laboratory provided seven sample coatings deposited on silicon wafers for us to test, and later compared our results with the at-wavelength EUV reflectance measurements done at the Advanced Light Source (ALS) synchrotron radiation facility at Lawrence Berkeley National Laboratory. We performed picosecond ultrasonic measurement on five points around the center of each wafer (see the inset in Fig. 4-7(a) for the geometry). One of the wafers was found defective because no vibration signals were detected, which was confirmed by the EUV reflectance measurement. Figure 4-7 (a) and (b) show the measured vibration frequencies  $\nu_1$  and  $\nu_2$ , respectively, for the other 6 wafers. The values of  $\Gamma$  and  $d$  extracted from  $\nu_1$  and  $\nu_2$  are shown in Fig. 4-7 (c) and (d), respectively (solid squares).  $d$  was calculated and plotted relative to  $d_{ref}$ , the period of the reference samples of Fig. 4-5. For comparison, the peak wavelength of EUV reflectance ( $\lambda_{euv}$ ) for each wafer is also shown in Fig. 4-7 (d) (open triangles), plotted relative to  $\lambda_{euv\_ref}$ , the peak EUV reflectance wavelength for the reference samples ( $d_{ref} = 6.90$  nm and  $\lambda_{euv\_ref} = 13.44$  nm). All of these wavelengths were measured somewhere near the center of each wafer. From Bragg's law, the period  $d$  is proportional to  $\lambda_{euv}$ . Therefore,  $d/d_{ref}$  and  $\lambda_{euv}/\lambda_{euv\_ref}$  can be directly compared.

We observed a systematic offset of the two data sets in Fig. 4-7 (d). A 0.6 % relative

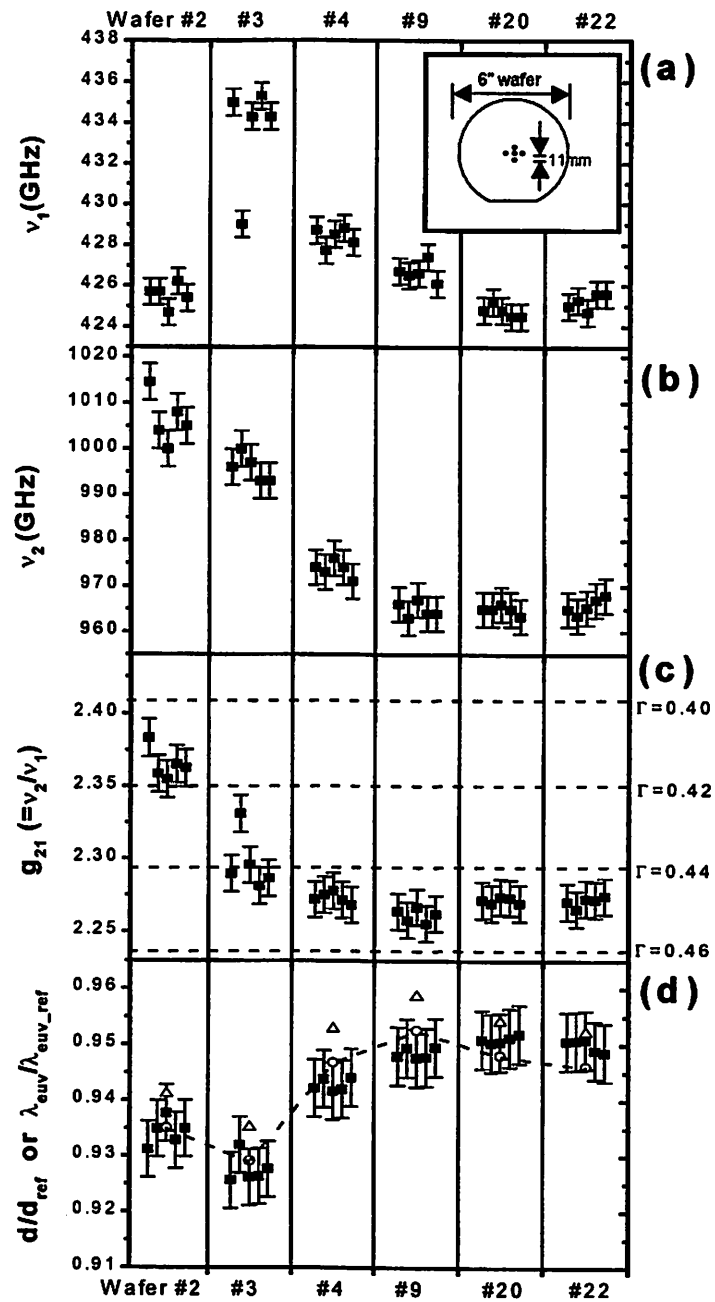


Figure 4-7 (a), (b) and (c): measured  $\nu_1$ ,  $\nu_2$  and  $g_{21}$  for test wafers. The inset in (a) shows the measurement geometry. (d): Comparison of  $d/d_{ref}$  (solid squares) extracted from  $\nu_1$  and  $\nu_2$ , and  $\lambda_{euv}/\lambda_{euv\_ref}$  (triangles) measured by EUV reflectometry. A 0.6% relative shift between them (open circles) makes them agree to within the error bar.

shift of either set of data (the open circles, for example) will make them agree to within the measurement error bar. The most likely cause for this offset is calibration drift of our measurement system, and in particular, the optical delay scanner, because of its mechanical nature. To verify this, we recalibrated it and found that indeed, the proportionality constant between the position output voltage  $V_{po}$  and the delay time  $\tau$  (see Fig. 3-3) had already shifted by  $\sim 1\%$  in 12 months. This can easily explain the offset because the reference wafers were measured 5 months before the test wafers, and the measured frequencies need to be corrected by the amount of miscalibration. Thus, the measurement accuracy of our current experimental setup is probably limited by this device. Frequent calibration can solve this problem, but a better solution is to use a more reliable way of real-time position detection such as optical interferometry, which is a mature technology and offers sub-micron precision. Besides this, there is still some room for us to improve our measurement precision and accuracy. For example, a better signal filtering/processing algorithm might improve the accuracy of the extraction of  $v_1$  and  $v_2$ . Also, more reference data points around  $\Gamma = 0.4$  can give a more accurate interpolation estimate of  $\Gamma$ . However, our preliminary results already demonstrate the viability of sample characterization using this new technique.

We believe this technique can be a very useful tool for diagnostic purposes or feedback measurements for the deposition process. It might also be a promising technique for in-situ real-time monitoring of the deposition process.

#### **4.5 Study of the non-vibrational response**

Up to now, we have focused our attention only on the vibrational signals of the  $\Delta R(\tau)$



curve and tried to answer questions like: “How many surface modes can be excited and detected?” , “How are their frequencies related to the multilayer structure?” , and “How to extract  $d$  and  $\Gamma$  from surface-mode frequencies for characterization purpose?” ,...etc.. We have not discussed anything about the non-vibrational response to the optical excitation although it’s much stronger in amplitude (1~2 orders of magnitude larger). In chapter 3, we mentioned several problems with signal detection inflicted by this response. It was treated as a troublemaker and needs to be suppressed deliberately. In fact, the essence of our alternating-pump technique is to reject this signal and the accompanying noise without affecting the vibrational signal. However, it contains the information about energy transport dynamics, and is useful in exploring time-resolved thermal properties of materials. Also, in the first few picoseconds after excitation, the detailed features of the sharp rising edge and the subsequent relaxation on the  $\Delta R(\tau)$  trace can reveal the dynamics of the interactions of hot electrons among themselves and with the lattice. All these aspects can be explored by studying the non-vibrational signal.

It is well known that a non-thermal distribution of carriers, or “hot” carriers in thermal equilibrium at a temperature higher than the one of the lattice can be produced when a light pulse is incident on the surface of an absorbing material. The delay necessary for the subsequent thermalization processes to be completed is roughly 1 ps[4.7]-[4.8]. After the lattice reaches thermal equilibrium with electrons, information about the temperature evolution can be deduced from the time-resolved reflectivity change of the sample. Similar to the strain-induced reflectance change in Eq. (2.11),  $\Delta R(\tau)$  can be related to the transient temperature distribution  $T(z, \tau)$  through a *temperature sensitivity function*  $f_T(z)$ :

$$\Delta R(\tau) = \int_0^{\infty} dz T(z, \tau) f_T(z) \quad (4.5)$$

Figure 4-8 (a) shows the normalized reflectance change as a function of time up to 120 ps in the Mo/Si multilayers with  $d = 6.9$  nm and  $\Gamma = 0.3, 0.4,$  and  $0.7$ . These curves show a very slowly decaying photothermal signal superimposed on a dc background with varying levels. B. Bonello *et al.*[4.9] attributed this dc offset to the accumulated heat deposited by the pump pulse train: each pump pulse produces a small temperature rise, and it piles up if the cooling is not completed before the next pulse enters. They found that this dc offset is a function of the chopping frequency  $\omega_c$ . At a not very high chopping frequency ( $< 10$  GHz), this dc offset is proportional to  $\omega_c^{-1/2}$ . Our chopping frequency is 100 kHz. Increasing  $\omega_c$  to 1 MHz can reduce this offset by a factor of 3, but, limited by the bandwidth of the auto-balanced detector circuit in our setup, it can not be higher than 125 kHz. Clearly this dc offset depends very strongly on  $\Gamma$ : in the sample with  $\Gamma = 0.3$  (thicker Si), it is twice as high as that in the sample with  $\Gamma = 0.7$  (thicker Mo). This suggests that amorphous Si has significantly lower thermal conductivity than Mo, which agrees with the results from theoretical[4.10] and experimental[4.11] study of amorphous Si. In fact, the thermal conductivity of a-Si is about 100 times lower than crystalline Si or Mo.

The decay of the photothermal response in these Mo/Si multilayers is remarkably slow compared to many other thin films[4.9], [4.12]-[4.13] and superlattices[4.6], [4.14]-[4.15]. In order to understand this behavior, we have studied also the photothermal responses of a Mo film and a Si film (see Fig. 4-8 (b)). Both films under study were deposited on Si wafers by rf-sputtering at 300 K. The film thicknesses are both greater

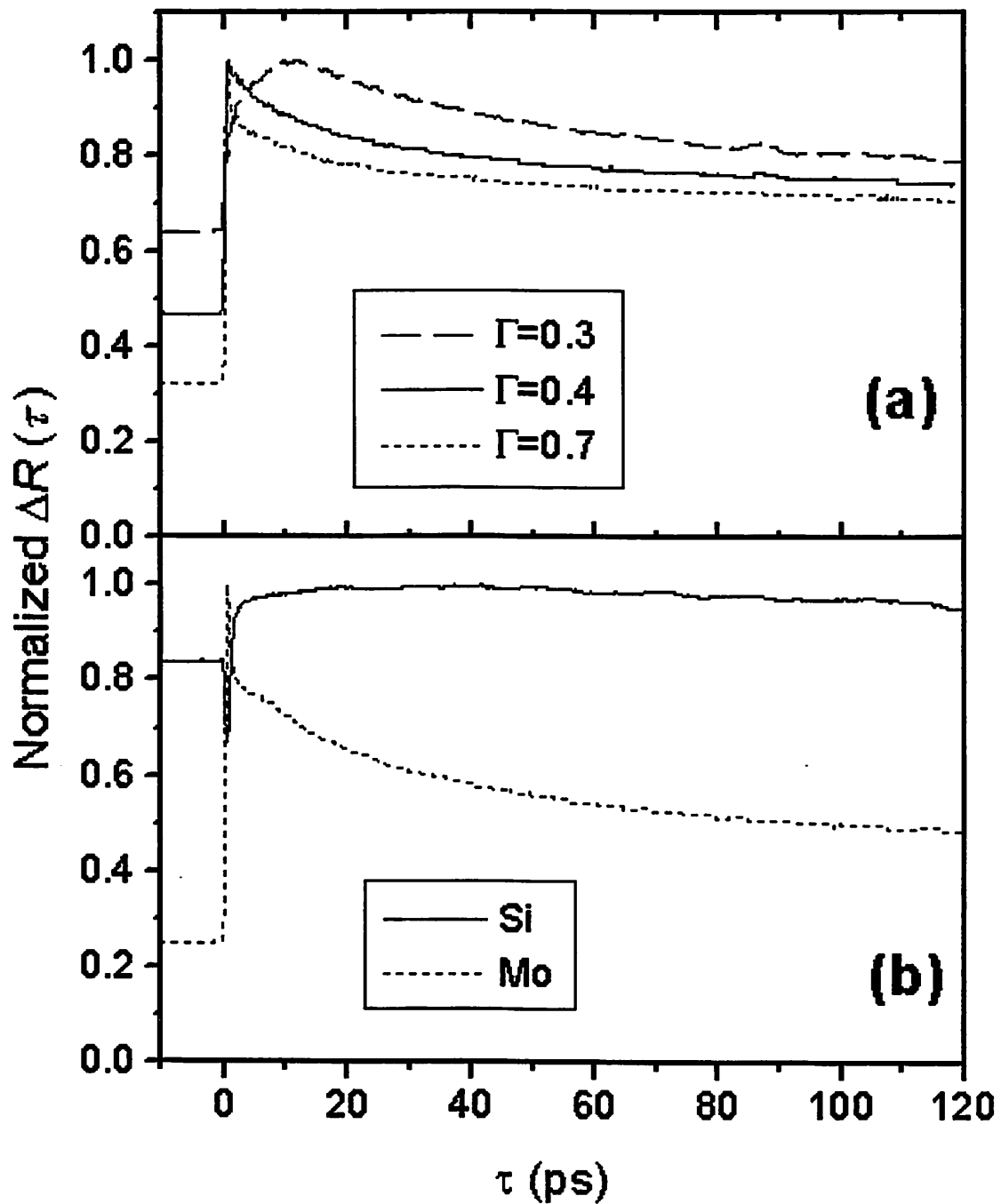


Figure 4-8 (a) Normalized  $\Delta R(\tau)$  traces (measured with conventional pump-probe scheme) for  $\Gamma = 0.3$  (dashed line), 0.4 (solid line), and 0.5 (dotted line). (b) Same traces for thick Mo (dotted line) and Si (solid line) films.

than 300 nm. The sharp spike on the Mo curve and the dip on the Si curve occurred within the first 1 ps are attributed to ultrafast carrier responses, which are also responsible for the initial sharp rising edge on the curves for Mo/Si multilayers. The subsequent behavior of  $\Delta R$  is completely different between the two materials: In Si, it rapidly increases and levels off in  $\sim 5$  ps, and then stays almost constant in our time scale. Whereas in Mo, it decays monotonically (slower than exponential) with a characteristic time (50% drop from the peak) of  $\sim 100$  ps, a typical value in metal films[4.9], [4.12]-[4.13]. The time dependence of the photothermal response in an absorbing medium has been studied by other researchers[4.9], [4.14]. The analysis is very straightforward: Assuming a Dirac  $\delta$  – function heat source(i.e., ignoring the 190-fs pulse duration and the  $\sim 1$ -ps electron-phonon thermalization time), the heat diffusion process is described by the 1-D Fourier equation

$$\frac{\partial^2 T}{\partial z^2} + S(z, \tau) = \frac{1}{D} \frac{\partial T}{\partial \tau} \quad (4.6)$$

with

$$S(z, \tau) = S_0 \exp\left(-\frac{z}{\zeta_e}\right) \delta(\tau)$$

where  $\zeta_e$  is the penetration depth of the heat source from the surface, and  $D$  is the thermal diffusivity of the sample. Ignoring the heat flowing out of surface, the boundary

condition at  $z = 0$  is :  $k \frac{\partial T}{\partial z} = 0$ , where  $k$  is the thermal conductivity of the material. The

solution to Eq. (4.6) is given by

$$T(z, \tau) = \frac{k}{D} \frac{S_0}{\sqrt{4\pi D \tau}} \int_{-\infty}^{\infty} dz' \exp\left[-\frac{(z - z')^2}{4 D \tau}\right] \exp\left(-\frac{|z'|}{\zeta_e}\right) \quad (4.7)$$

Considering the solution at a large delay time  $\tau \gg z^2 / 4D$ , the exponential term in Eq. (4.7) approaches 1, and  $T$  is proportional to  $\tau^{-1/2}$ . In a metal, the depth probed by the light pulses being the optical absorption length  $\zeta$ , the condition becomes:  $\tau \gg \zeta^2 / 4D$ , which corresponds to only a few picoseconds. So the decay of  $\Delta R$  curve in a bulk metal should be proportional to  $\tau^{-1/2}$  for  $\tau$  greater than a few tens of ps. This relation is also valid for a metal film provided  $\tau$  is shorter than the time for the heat to diffuse into the substrate ( $\sim 2$  ns in a 300-nm-thick Mo film). The reflectance change  $\Delta R(\tau)$  in our Mo film is replotted in a log-log scale to verify this  $\tau^{-1/2}$  time dependence (Fig. 4-9). The scan range was extended to 1.3 ns by using a 20 cm long translation stage. The dashed line depicts the expected  $\tau^{-1/2}$  dependence and has a slope of  $-0.5$ . The agreement between experiment and  $\tau^{-1/2}$  law is excellent for a time greater than 100 ps. Deviation from the straight line becomes greater towards shorter delay times because the exponential term in the integral of Eq. (4.7) can no longer be treated as a constant, and the  $\tau^{-1/2}$  law fails.

Apparently the  $\Delta R$  curve in the a-Si film does not follow this simple  $\tau^{-1/2}$  rule. The reason is again because amorphous Si has a very small thermal conductivity ( $k \sim 1.4$  W/mK), which is 2 orders of magnitude lower than crystalline Si or Mo. Since  $D$  is proportional to  $k$ , the condition  $\tau \gg \zeta^2 / 4D$  can never be satisfied in a-Si in our time scale, and we need to evaluate the integral in Eq. (4.7) to find out the time dependence. In fact, for  $\tau = 100$  ps, the deposited heat only diffuses by a distance  $l = \sqrt{D\tau} = 90 \text{ \AA}$ , much shorter than the penetration depth  $\zeta$ . That explains why  $\Delta R$  remains almost constant in a-Si for over 100 ps. The long-term behavior of  $\Delta R(\tau)$  in

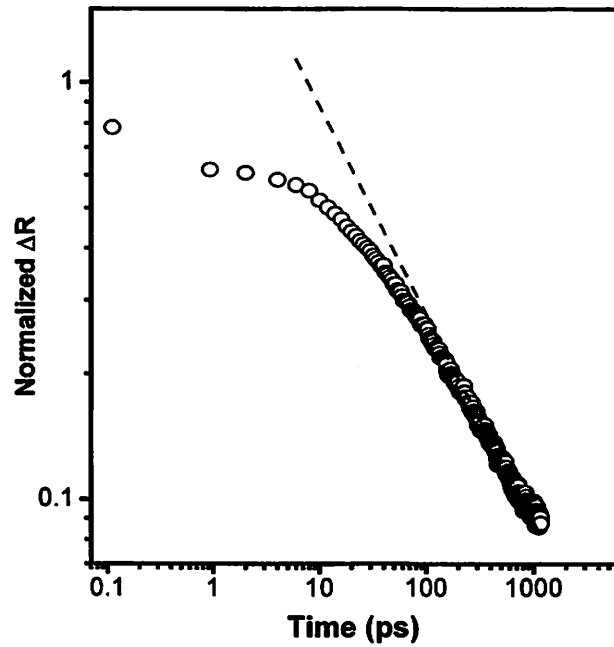


Figure 4-9 Logarithmic plot of  $\Delta R(\tau)$  in a Mo film. The dashed line corresponds to a decay proportional to  $\tau^{-1/2}$

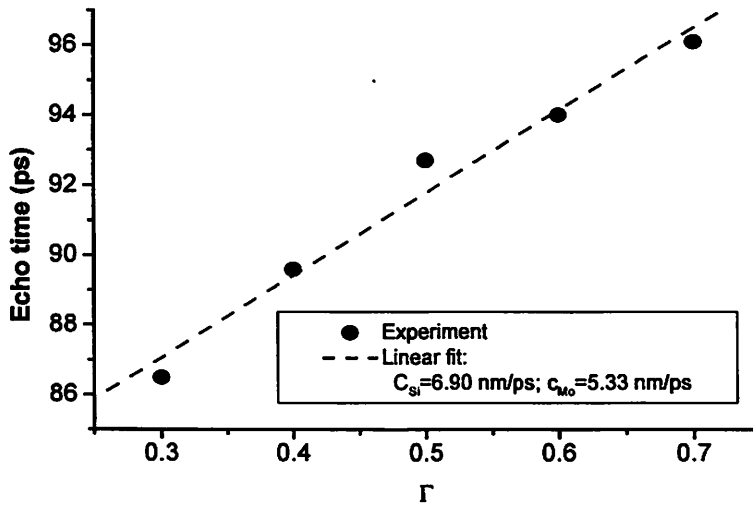


Figure 4-10 The echo time of the initial acoustic pulse for samples with various  $\Gamma$  (solid dots). The dashed line is a linear fit corresponding to:  $c_{Si} = 6.90 \times 10^3 \text{ m/s}$  and  $c_{Mo} = 5.33 \times 10^3 \text{ m/s}$ .

Mo/Si multilayers are dominated by this slow thermal diffusion through a-Si layers, which block the most efficient path for heat dissipation, viz. into the substrate. Consequently the three curves on Fig. 4-8(a) all show more or less the same slow decay behavior. Incidentally, the curve for  $\Gamma = 0.3$  looks unexpectedly different from the one for  $\Gamma = 0.4$  in the first 10 ps. This is not so surprising if we recall that the number “ $\Gamma$ ” used here does not reflect the real Mo thickness after silicide formation. The real thickness of Mo layers for “ $\Gamma = 0.3$ ” is considerably less than  $0.3 \times 69 = 20.7 \text{ \AA}$ . In fact, it is comparable to or even less than the combined thickness of silicide interlayers ( $\sim 10 \text{ \AA}$  for Mo-on-Si interfaces;  $\sim 5 \text{ \AA}$  for Si-on-Mo interfaces[4.2] ). Therefore, the thermal diffusion property in this sample can be quite different from the others.

The echo of the initial acoustic pulse as mentioned in §2.1.1 emerges as a small bump on the  $\Delta R$  curve near  $\tau = 90$  ps (Fig. 4-8(a)). By measuring the delay time  $\tau_{echo}$  of this bump, the longitudinal sound velocity in Mo and a-Si layers can be determined. Fig. 4.10 shows the measured  $\tau_{echo}$  versus  $\Gamma$ . Assuming a 2-sublayer structure, the linear fit (dashed line) yields :  $c_{Si} = 6.90 \times 10^3$  m/s and  $c_{Mo} = 5.33 \times 10^3$  m/s. These numbers were actually used in calculating the theoretical curves of  $v_1$  and  $v_2$  in Fig. 4-5, and the results agreed better to the experiment than using the values for bulk, crystalline Mo and Si. (not shown).

#### 4.6 Laser damage to the Mo/Si multilayers

During the pump-probe measurements, a damage to the multilayer coatings due to laser heating was observed. A 1.9% drop of vibration frequency  $v_1$  was detected under 1

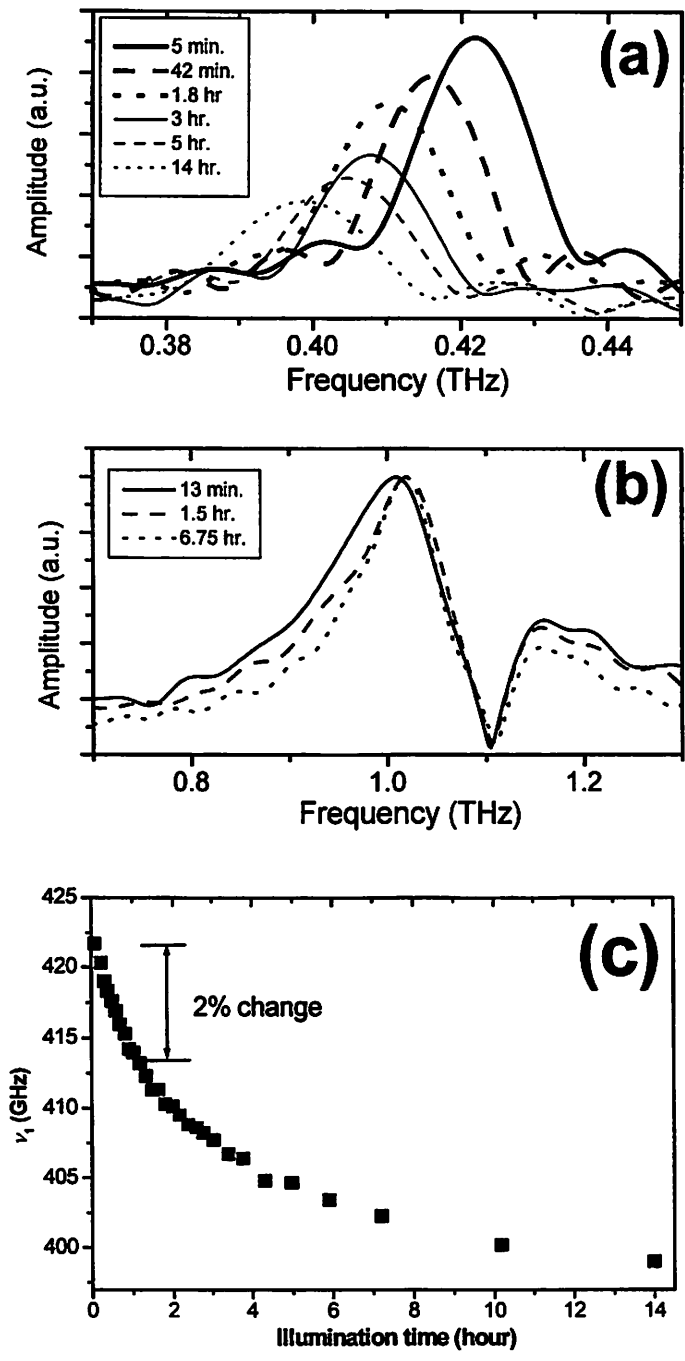


Figure 4-11 (a) and (b): the vibration spectra of the 1<sup>st</sup>- and 2<sup>nd</sup>-gap mode after various amount of laser illumination time. (c):  $\nu_1$  as a function of illumination time.



hour of continuous laser illumination with an intensity of 32 kW/cm<sup>2</sup>. Fig. 4-11(a) and (b) show the vibration spectra of the 1<sup>st</sup>- and 2<sup>nd</sup>-gap surface modes after varying amount of illumination time ( $d = 6.9$  nm,  $\Gamma = 0.4$ ). The peak frequency of the 1<sup>st</sup> mode  $\nu_1$  was plotted as a function of illumination time on Fig. 4-11 (c). After about 14 hours, it decreases by  $\sim 5.4\%$  and reaches an asymptote. The vibration strength of this mode also decays monotonically with time. In contrast to the decrease in  $\nu_1$ , the peak frequency of the 2<sup>nd</sup>-gap mode remains almost unchanged ( $\sim 0.8\%$  increase after 7 hours). We also found that the laser damage effect is localized within the spot size of the pump laser beam, as evidenced by a negligible frequency shift at a distance of 10  $\mu\text{m}$  from the center of the spot.

The effect of laser damage on the peak wavelength and reflectance of EUV radiation was investigated with EUV reflectometry done at the ALS by Dr. Seongtae Jeong. We burned a 4 by 4 array of damaged spots near the center of a 6" multilayer reflector with various laser illumination times. The spacing between spots is 100  $\mu\text{m}$ , and the illumination time varies from 1 to 2.5 hours (at a higher laser intensity to accelerate damaging). The areal scan result by an EUV beam is shown in Figure 4-12. In spite of the presence of particulates or defects, the 4 x 4 array of damaged spots is clearly seen. To find out the effect on EUV reflectance and peak frequency, wavelength scans are done at both damaged (solid arrow) and clear (dashed arrow) regions. The measured spectra were shown in Fig. 4-13(a), and for comparison, we show the ultrasonic spectra in Fig. 4-13(b). Surprisingly, the EUV spectrum barely changed after laser damage, while the ultrasonic spectrum suffered drastic change. The surface mode frequency  $\nu_1$  decreased by 6%, its amplitude dropped by 50%, and the linewidth broadened by 130%. In

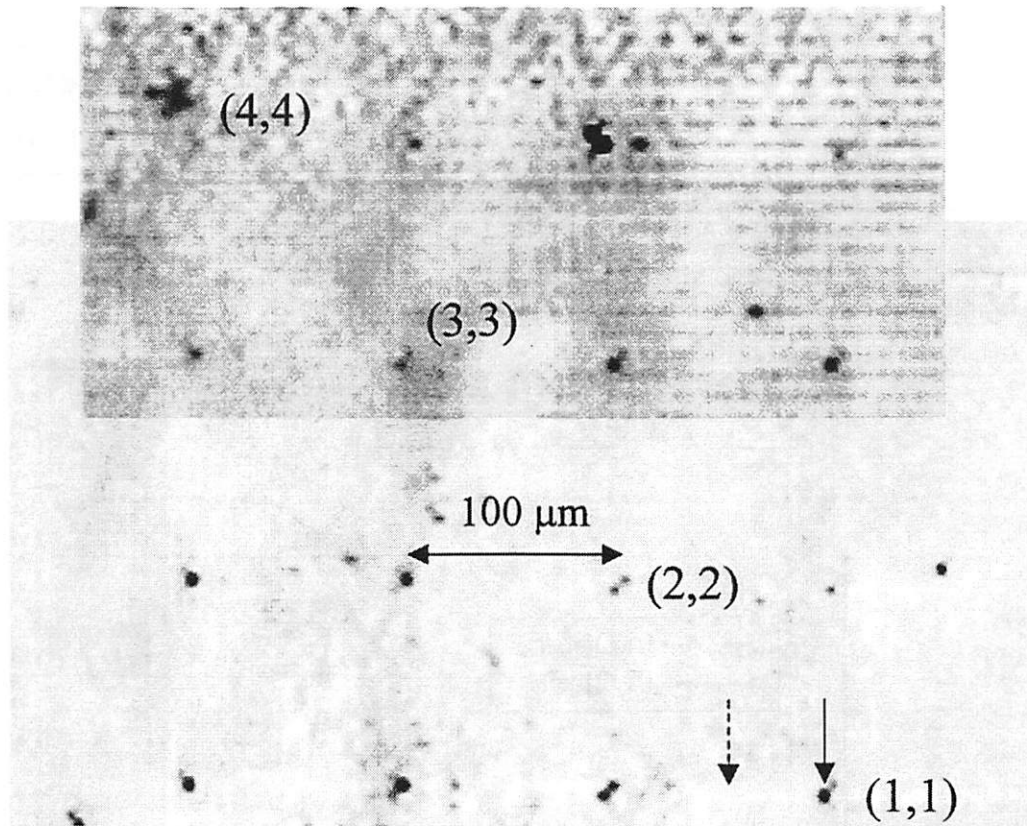


Figure 4-12 An areal EUV-beam scan (bright field) of the sample with a 4 x 4 array of laser-damaged spots. EUV reflectance spectra and ultrasonic spectra were taken in damaged (solid arrow) and clear (dashed arrow) regions

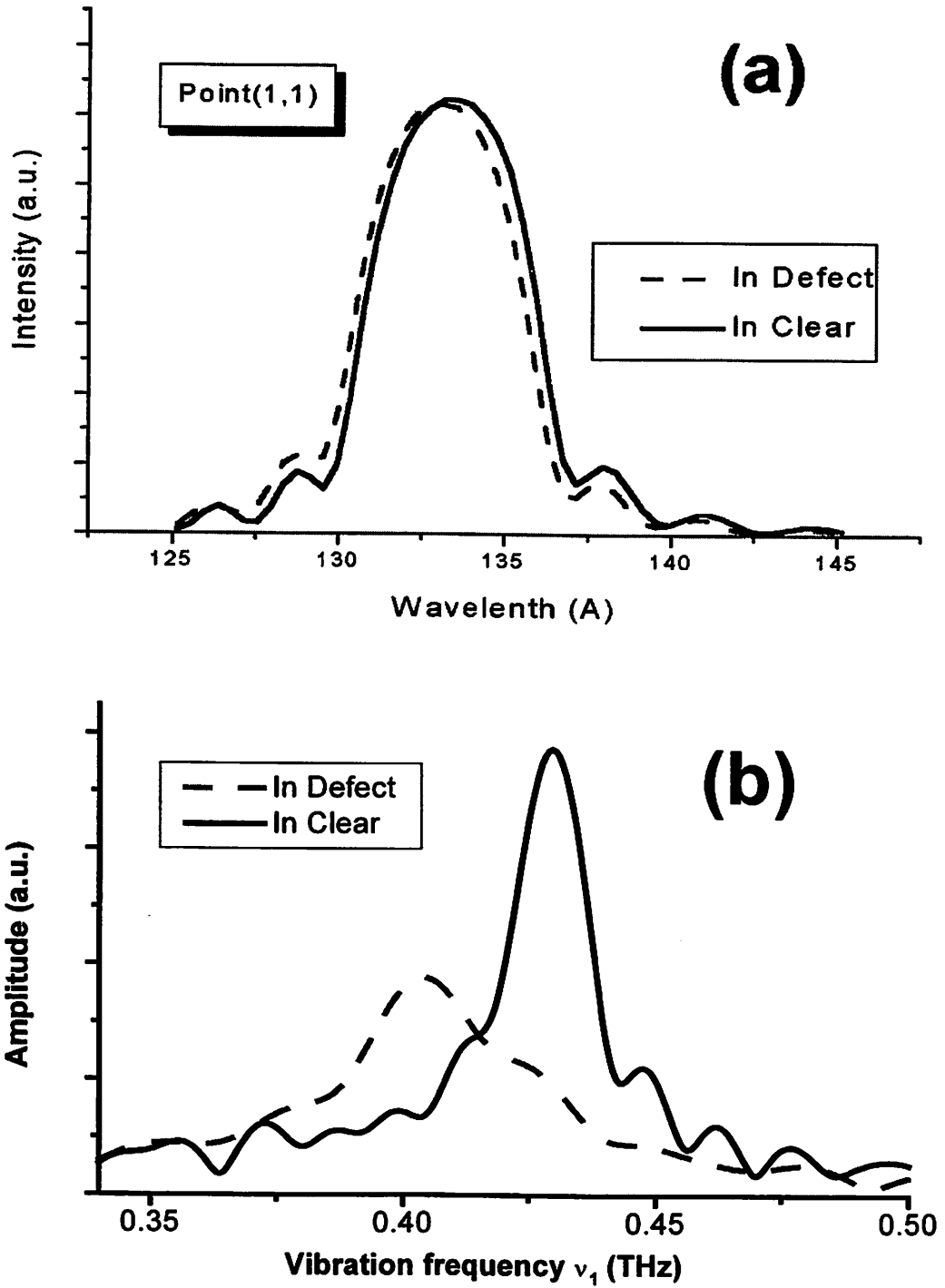


Figure 4-13 (a) The EUV reflectance spectra measured in laser-damaged (dashed line) and clear (solid line) regions. (b) The corresponding vibration spectra.

contrast, the peak EUV wavelength shifted by only 0.3% and the reflectivity only dropped by 1%. This dramatic difference between the two might indicate that the laser damage is very shallow in nature, affecting only one or two layers under the surface. As discussed in Chapter 2, the surface modes are localized near the surface and their frequencies depend very strongly on the property of shallow layers, whereas EUV radiation can penetrate much deeper into the multilayer stack and its reflectance is not so sensitive to the surface conditions. This hypothesis of shallow damage is consistent with the fact that the heat deposited into multilayers is a fast decaying exponential function. (See Fig. 5-2)

Another piece of evidence supporting our hypothesis of shallow damage is provided by an annealing experiment. Several pieces of Mo/Si multilayer samples were annealed at 200 or 300 °C in Ar or O<sub>2</sub> ambient gases. The vibration spectra near  $\nu_1$  for annealed samples are shown in Fig. 4-14. Also shown is the curve for an unannealed sample (solid line) for comparison. Contrary to the laser damage case, the peak frequency  $\nu_1$  shifted *up* after annealing, and the amount of shift depends strongly on temperature. At 300 °C,  $\nu_1$  increased by as much as 4% in 35 minutes, while at 200 °C it only increased by 0.8% in 1 hour. Annealing in Ar or in O<sub>2</sub> yields no obvious difference in the results. The opposite shifts of  $\nu_1$  in laser and thermal annealing are surprising, assuming that the damage caused by laser pulses is purely thermal at our intensity level. Unless there is an unknown photon-assisted chemical process, the main difference between the two cases is the temperature gradient, which is huge (of the order of 10 K/layer) in laser heating and negligible in annealing furnaces. In other words, thermal annealing is more or less uniform while laser damaging is very shallow and might only occur in the top few layers.

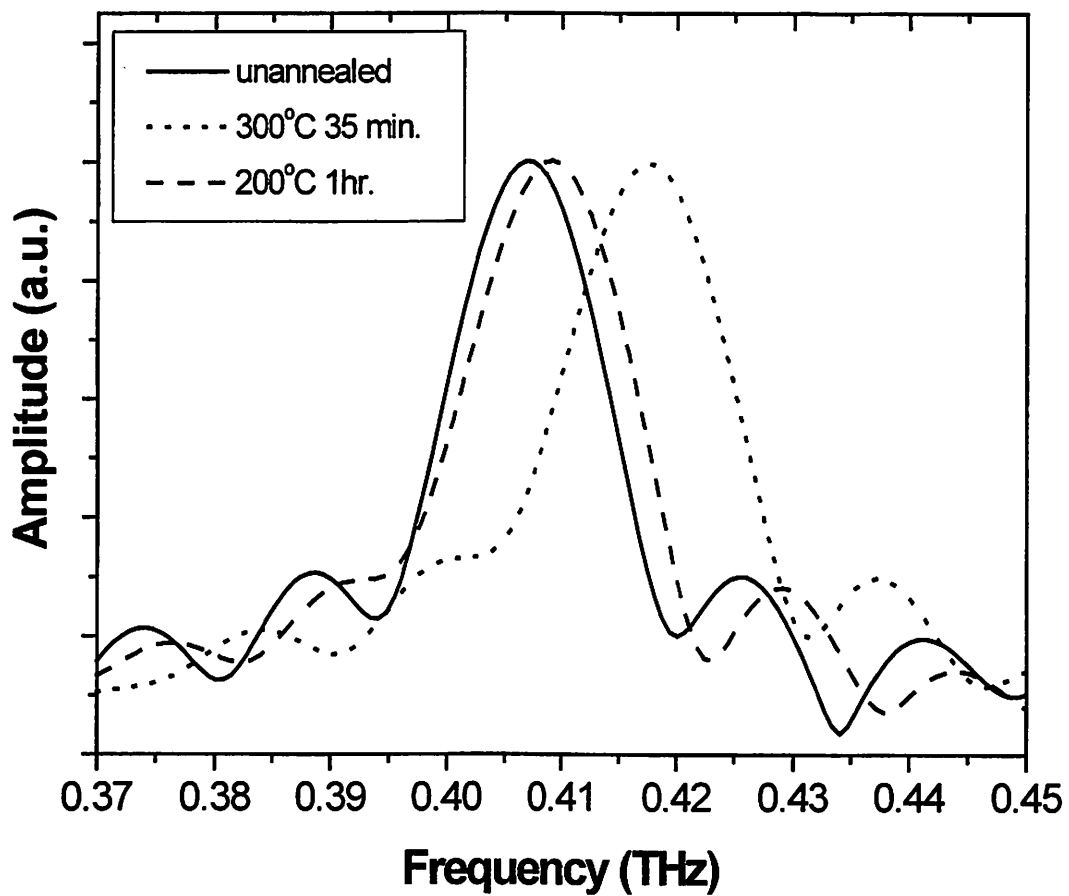


Figure 4-14 The vibration spectra near  $\nu_1$  for annealed (dotted and dashed lines) and unannealed samples (solid line).

Possible mechanisms for this laser damage effect are (1) growth of silicide interdiffusion layers, (2) growth of the surface oxide layer, or (3) change of material properties induced by laser heating. All of them can change the surface-mode frequencies  $\nu_1$  and  $\nu_2$ . The effect of oxide growth on these frequencies was discussed in §2.3.3, which does not resemble the observed tendency ( $\nu_1$  decreases and  $\nu_2$  remains unchanged). The frequency shift due to silicide growth can be approximately calculated by the 4-sublayer model in §2.3.2, provided we know the sound velocity and density of the silicide. Our calculation results indicate that the impact on these frequencies due to either oxide or silicide growths should scale with  $(1/d)$ . Because the thicker the Mo/Si layers, the less the thickness percentage of oxide or silicide layers. However, this does not agree with our experimental observations. Figure 4-15 (a) and (b) shows the frequency  $\nu_1$  as a function of illumination time in samples with  $d = 19.55$  and  $32.56$  nm, respectively. (As before,  $\nu_2$  stays almost constant.) There is very little change in the damage rate as we vary  $d$ . Intuitively, this fact points to change of material properties as the most possible mechanism, because it does not scale with  $d$ .

Based on our hypothesis of shallow damaging, we can assume, to the 1<sup>st</sup> approximation, that any change in material parameters occurs in the 1<sup>st</sup> bilayer only. Then we treat the first bilayer as a cap layer, and calculate  $\nu_1$  and  $\nu_2$  following the analysis in §2.3.1. The only material parameters involved in the calculation are density  $\rho$  and sound velocity  $c$ . But it turns out that they always lump together in the equations (in the tangents of Eq. (4.1), layer thickness is proportional to  $(1/\rho)$ ), and so only the product  $\rho c$  ( $= Z$ , the acoustic impedance) matters. Figure 4-16 shows one possible

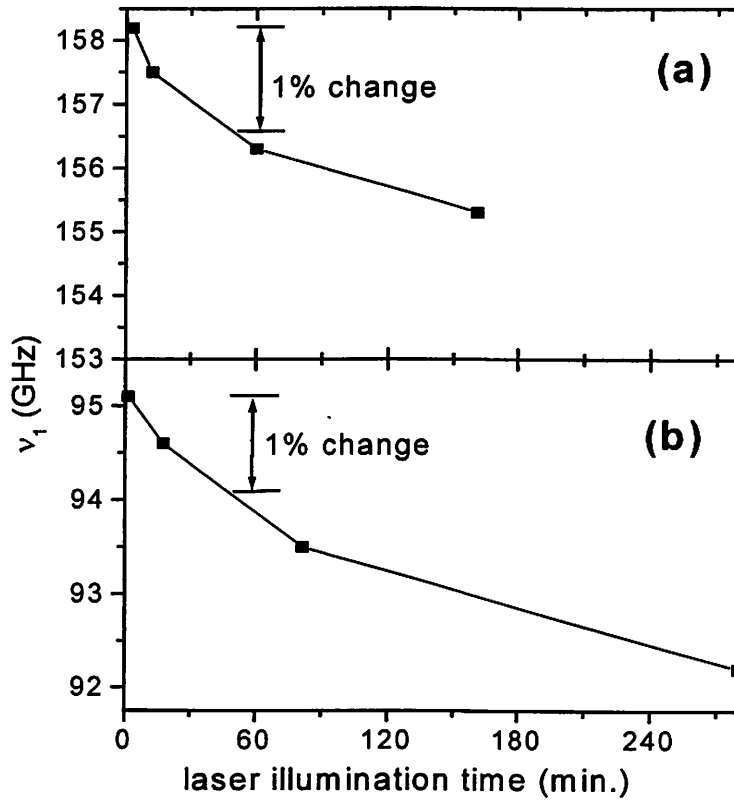


Figure 4-15  $\nu_1$  as a function of illumination time in samples with  $d =$  (a) 19.55 and (b) 32.56 nm,

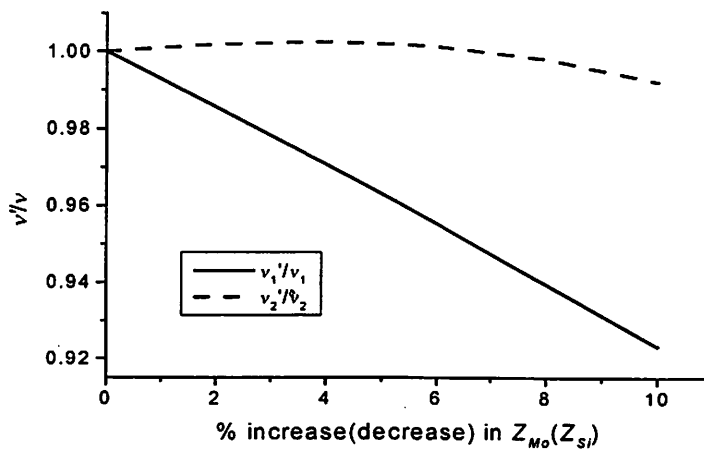


Figure 4-16 Frequency shifts induced by changes in acoustic impedance  $Z$ . ( $Z_{Mo}$  increases and  $Z_{Si}$  decreases by the same percentage).

combination of the changes in  $Z_{Mo}$  and  $Z_{Si}$  (in the 1<sup>st</sup> bilayer):  $Z_{Mo}$  increases and  $Z_{Si}$  decreases by the same percentage. These curves nicely reproduce the observed tendency of laser damaging :  $v_1$  decreases and  $v_2$  remains unchanged. In addition, they are insensitive to the value of  $d$ . Although the physical origin for this change in material properties is unascertained, we speculate that it is related to relaxation of film stress. It is well known that Mo/Si multilayers develop large compressive stress during growth, typically  $-450$  to  $-350$  MPa, which causes distortion of the extremely precise optical element figure[4.17]-[4.18]. Post-deposition annealing can reduce this residual stress efficiently at temperatures less than  $200$  °C[4.19]. ( Note that silicide hardly grows at such low temperatures[4.2]). Interestingly enough, in-situ stress measurements during growth of Mo/Si multilayers directly show that Mo layers are tensile, while Si is compressive[4.5]. Therefore, stress relaxation induced by laser heating might cause Mo and Si properties (such as  $Z_{Mo}$  and  $Z_{Si}$ ) to change in opposite directions, which justifies our choice of opposite signs for  $\Delta Z_{Mo}$  and  $\Delta Z_{Si}$  in Fig. 4-16.

Although this damage effect is a potential disadvantage of our technique, we believe that it is not of significant concern. The data acquisition time required to measure at a single point on the multilayer is only  $\sim 3$  minutes, which leads to a  $\Delta v_1 \sim 0.1\%$ . In terms of EUV reflectivity, this damage is unperceivable ( $\Delta R_{EUV} \sim 0.02\%$ ). Also, the damage is localized within a very small region of only 10 microns in diameter. In applications where even this could not be tolerated, measurements could be made in points outside the critical area.

## 4.7 Summary



In this chapter, we have discussed various experimental results of picosecond ultrasonic study on Mo/Si multilayers. The 1st and the 2nd acoustic-phonon surface modes were observed in all Mo/Si multilayers using the alternating-pump technique. A higher-gap mode ( the 6<sup>th</sup> gap) was observed in some of the samples with thicker coating periods. The dependence of these frequencies on  $d$  and  $\Gamma$  was studied both theoretically and experimentally. The frequencies  $\nu_n$  were found to be inversely proportional to  $d$ , and the ratio of two frequencies  $\nu_m/\nu_n$  is a function of  $\Gamma$  only.

We have also demonstrated the utility of our picosecond ultrasonic technique for characterizing Mo/Si EUV multilayer coatings. The thickness profile of a 2% graded sample was successfully mapped by measuring  $\nu_2$  with a 0.16% precision. By measuring  $\nu_1$  and  $\nu_2$  simultaneously, we successfully extracted  $d$  and  $\Gamma$  in Mo/Si multilayers. Apart from a systematic offset, probably due to calibration drift, our results are in agreement with EUV reflectance measurements.

The non-vibrational component of  $\Delta R$  signal was also studied and was attributed to the photothermal response of the constituent materials. The slow decay of  $\Delta R(\tau)$  curves was due to the small thermal conductivity in a-Si layers. Finally, we discussed the damage to multilayers caused by laser illumination. We found that the damage is localized laterally and shallow in depth, and its mechanism is changes in material properties, most likely due to stress relaxation. Its effect on EUV reflectometry was negligible given our data-acquisition time.

## References

- [4.1] T.D. Nguyen, *Microstructure-Interference-Property Relationships in Nanometer-Period X-Ray Multilayers*, Ph.D. thesis, Applied Science and Technology Program, University of California, Berkeley (1993).
- [4.2] R.S. Rosen, D.G. Stearns, M.A. Viliardos, M.E. Kassner, S.P. Vernon and Y. Cheng, *Applied Optics*, **32**, 6975 (1993).
- [4.3] B.M. Clemens and G.L. Eesley, *Physical Review Letters*, **20**, 2356 (1988).
- [4.4] E.E. Fullerton, I.K. Schuller, F.T. Parker, K.A. Svinarich, G.L. Eesley, R. Bhadra and M. Grimsditch, *Journal of Applied Physics*, **73**, 7370 (1993).
- [4.5] J.M. Freitag, B.M. Clemens, *Applied Physics Letters*, **73**, 43 (1998).
- [4.6] W. Chen, Y. Lu, H.J. Maris and G. Xiao, *Physical Review*, **B 50**, 14506 (1994).
- [4.7] J.G. Fujimoto, J.M. Liu, E.P. Ippen, and N. Bloembergen, *Physical Review Letters*, **53**, 1837 (1984).
- [4.8] S.D. Brorson, J.G. Fujimoto, and E.P. Ippen, *Physical Review Letters*, **59**, 1962 (1987).
- [4.9] B. Bonello, B. Perrin, and C. Rossignol, *Journal of Applied Physics*, **83**, 3081 (1998).
- [4.10] J.L. Feldman, M.D. Kluge, P.B. Allen, and F. Wooten, *Physical Review*, **B 48**, 12589 (1993).
- [4.11] D.G. Cahill, H.E. Fischer, T. Klitsner, E.T. Swartz, and R.O. Pohl, *Journal of Vacuum Science and Technology*, **A 7**, 1259 (1989).
- [4.12] G.L. Eesley, C.A. Paddock, and B.M. Clemens, in *Ultrafast Phenomena V*, edited by G.R. Fleming and A.E. Siegman, Springer Verlag, Berlin-Heidelberg, 1986, p. 257.

- [4.13] B. Bonello, B. Perrin, E. Romatet and J.C. Jeannet, *Ultrasonics*, **35**, 223 (1997).
- [4.14] H.T. Grahn, H.J. Maris, J. Tauc, and B. Abeles, *Physics Review*, **B 38**, 6066 (1986).
- [4.15] B. Perrin, B. Bonello, J.C. Jeannet and E. Romatet, *Physica*, **B 219&220**, 681 (1996).
- [4.16] M.N. Özisik, *Heat Conduction*, Wiley, New York, 1980.
- [4.17] D.G. Stearns, R.S. Rosen, and S.P. Vernon, *Applied Optics*, **32**, 6952 (1993).
- [4.18] P.A. Spence, M.P. Kanouff, and A.K. Ray-Chaudhuri, *Proceedings of SPIE on Emerging Lithographic Technologies III*, vol. **3676**, p.724 (1999).
- [4.19] P.B. Mirkarimi, and C. Montcalm, *Proceedings of SPIE on Emerging Lithographic Technologies II*, vol. **3331**, p.133 (1998).

## Chapter 5. Numerical simulations

Although an analytical equation for calculating surface-mode frequencies has been derived in Chapter 2 by solving the eigenvalue problem, it doesn't offer the information of excitation strengths, spectral lineshapes, or amplitudes of optically detected signals. To better understand these experimentally observed quantities and also to see more clearly the whole picture of the physical process, a numerical simulation of the elastic wave equation is required. In this chapter, we will describe the method and results for our simulation in comparison with the analytical model in chapter 2 and the experimental results in Chapter 4.

### 5.1 Overview

To solve the elastic wave equation, first we need to calculate the spatial dependence of the initial thermal stress produced by the pump light pulse. This can be done in a straightforward way by using the transfer-matrix method for electromagnetic waves. The subsequent relaxation of this initial stress will generate acoustic waves according to the equations of elasticity (2.4) and (2.5). A more complete simulation should also incorporate the equation of heat diffusion to calculate the temporal and spatial dependence of the temperature profile, which acts as a driving term in Eq. (2.4). Finally, to calculate the optical reflectivity change induced by these waves, we must sum up the contribution from strain waves at all depths. In other words, we need to know the "sensitivity function"  $f(z)$  as mentioned in Chapter 2. For simplicity, the contribution to  $\Delta R$  from hot electrons in the first 1 ps is not included, i.e., only the lattice thermal stress

is considered. Also, the attenuation of the acoustic waves through all kinds of loss mechanisms is neglected.

## 5.2 Initial stress generation

Consider an electromagnetic wave incident on a Mo/Si multilayer stack (See Fig. 5-1). The energy  $W(z)$  deposited per unit volume at a depth  $z$  is given by

$$W(z) = \frac{\alpha(z)n(z)Q}{A} \left| \frac{E(z)}{E_0^+} \right|^2 \quad (5.1)$$

where  $\alpha$  and  $n$  are the absorption coefficient and the real part of the refractive index,  $Q$  is the incident pulse energy,  $A$  is the illuminated area, and  $E(z)$  and  $E_0^+$  are the electric fields at depth  $z$  in the multilayer and of the incident wave, respectively. For simplicity, we consider all quantities to have only one-dimensional space dependence.

The field amplitude  $E(z)$  in a multilayer is calculated using a transfer-matrix method[5.1]. Referring to Fig. 5-1 for the geometry, let  $E_m^+$  and  $E_m^-$  be the electric-field amplitudes of the forward- and backward-propagating waves in the  $m$ th layer but adjacent to the interface between the  $m$ th and the  $(m+1)$ th layers. The relation between  $(E_m^+, E_m^-)$  and  $(E_{m-1}^+, E_{m-1}^-)$  can be written in matrix form

$$\begin{pmatrix} E_m^+ \\ E_m^- \end{pmatrix} = \frac{1}{t_m'} \begin{pmatrix} e^{-i\delta_m} & -r_m e^{-i\delta_m} \\ -r_m e^{i\delta_m} & e^{i\delta_m} \end{pmatrix} \begin{pmatrix} E_{m-1}^+ \\ E_{m-1}^- \end{pmatrix} \quad (5.2)$$

where

$$\delta_m = \hat{k}_{zm} d_m = 2\pi \left( \frac{\hat{n}_m \cos \phi_m}{\lambda} \right) d_m$$

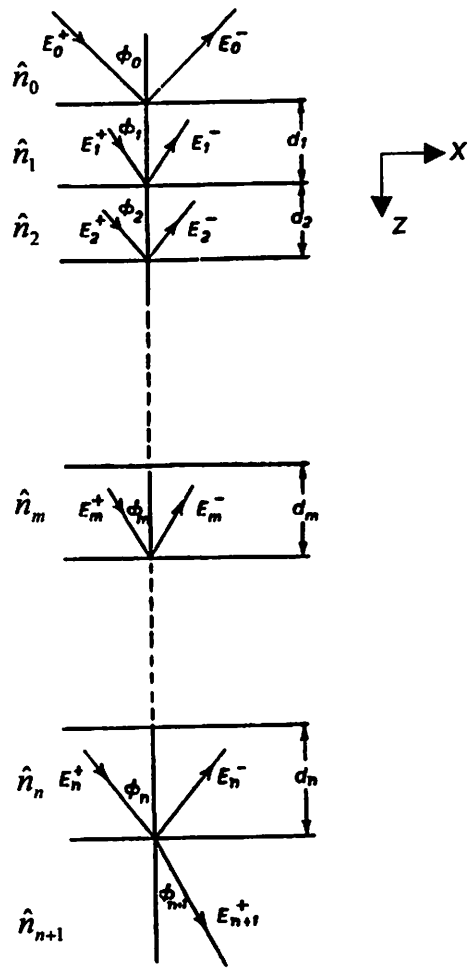


Figure 5-1 The geometry for an electromagnetic wave incident on a Mo/Si multilayer stack

$\hat{n}_m$  and  $\hat{k}_{zm}$  are respectively the complex refractive index ( $\hat{n} \equiv n + i \kappa$ ), and the  $z$  component of the wave vector in the  $m$ th layer.  $\lambda_0$  is the wavelength in vacuum.  $r_m$  and  $t_m$  are the Fresnel coefficients[5.2]:

$$r_m = \begin{cases} \frac{g_{m-1} - g_m}{g_{m-1} + g_m} & (TE) \\ \frac{g_{m-1}/\hat{n}_{m-1}^2 - g_m/\hat{n}_m^2}{g_{m-1}/\hat{n}_{m-1}^2 + g_m/\hat{n}_m^2} & (TM) \end{cases}$$

$$t_m = \begin{cases} \frac{2g_m}{g_{m-1} + g_m} & (TE) \\ \frac{2g_m/\hat{n}_m\hat{n}_{m-1}}{g_{m-1}/\hat{n}_{m-1}^2 + g_m/\hat{n}_m^2} & (TM) \end{cases}$$

where

$$g_m \equiv \sqrt{\hat{n}_m^2 - \cos^2 \phi_0}$$

Once  $(E_m^+, E_m^-)$  is found, the forward- and backward-propagating electric fields at any point  $z$  in the  $m$ th layer is given by

$$\begin{pmatrix} E_m^+(z) \\ E_m^-(z) \end{pmatrix} = \begin{pmatrix} e^{i\hat{k}_{zm}(z - \sum_{i=1}^m d_i)} & 0 \\ 0 & e^{-i\hat{k}_{zm}(z - \sum_{i=1}^m d_i)} \end{pmatrix} \begin{pmatrix} E_m^+ \\ E_m^- \end{pmatrix} \quad (5.3)$$

By using Eqs. (5.2) and (5.3), we can relate the electric field amplitude *at any depth*  $z$  to the incident and reflected waves  $(E_0^+, E_0^-)$  through a transfer matrix:

$$\begin{pmatrix} E_m^+(z) \\ E_m^-(z) \end{pmatrix} = M(z) \begin{pmatrix} E_0^+ \\ E_0^- \end{pmatrix} \quad (5.4)$$

For a point  $z = z'$  in the substrate, the backward-propagating wave  $E_m^-(z')$  has to vanish (since the substrate is considered infinitely thick). Thus we get :  $M_{21}(z')E_0^+ + M_{22}(z')E_0^- = 0$ , and so the reflection coefficient  $r_0$  for the multilayer stack is simply

$$r_0 = \frac{E_0^-}{E_0^+} = -\frac{M_{21}(z')}{M_{22}(z')} \quad (5.5)$$

And the reflectance is given by

$$R = r_0 r_0^*$$

It is noteworthy that this is exactly the same formalism for calculating the EUV reflectance of multilayer coatings[5.3], as mentioned briefly in Chapter 1. The final expression for  $E(z)$ , the total electric field at a depth  $z$ , required in Eq. (5.1) to evaluate  $W(z)$  is

$$E(z) = E^+(z) + E^-(z) = E_0^+ [M_{11}(z) + M_{21}(z) + r_0 (M_{12}(z) + M_{22}(z))] \quad (5.6)$$

For the optical properties of Mo and Si, we used the values  $\alpha_{Si} = 0.9 \times 10^3 / \text{cm}$  ( $\kappa_{Si} = 5.73 \times 10^{-3}$ ),  $n_{Si} = 3.68$ [5.4],  $\alpha_{Mo} = 5.73 \times 10^5 / \text{cm}$  ( $\kappa_{Mo} = 3.65$ ), and  $n_{Mo} = 3.46$ [5.5]. The deposited energy as a function of  $z$  for a Mo/Si multilayer with  $d = 70 \text{ \AA}$  and  $\Gamma = 0.4$  is shown in Fig. 5-2. Since  $\alpha_{Si} \ll \alpha_{Mo}$  most of the energy is deposited in the molybdenum layers. The effective skin depth is about  $500 \text{ \AA}$ . The deposited energy leads to a temperature rise in the multilayer which sets up a thermal stress of magnitude

$$\sigma(z) = \frac{-3BW(z)\beta}{C\rho} \quad (5.7)$$

where  $B$  is the bulk modulus,  $\beta$  is the linear expansion coefficient,  $C$  is the specific heat,



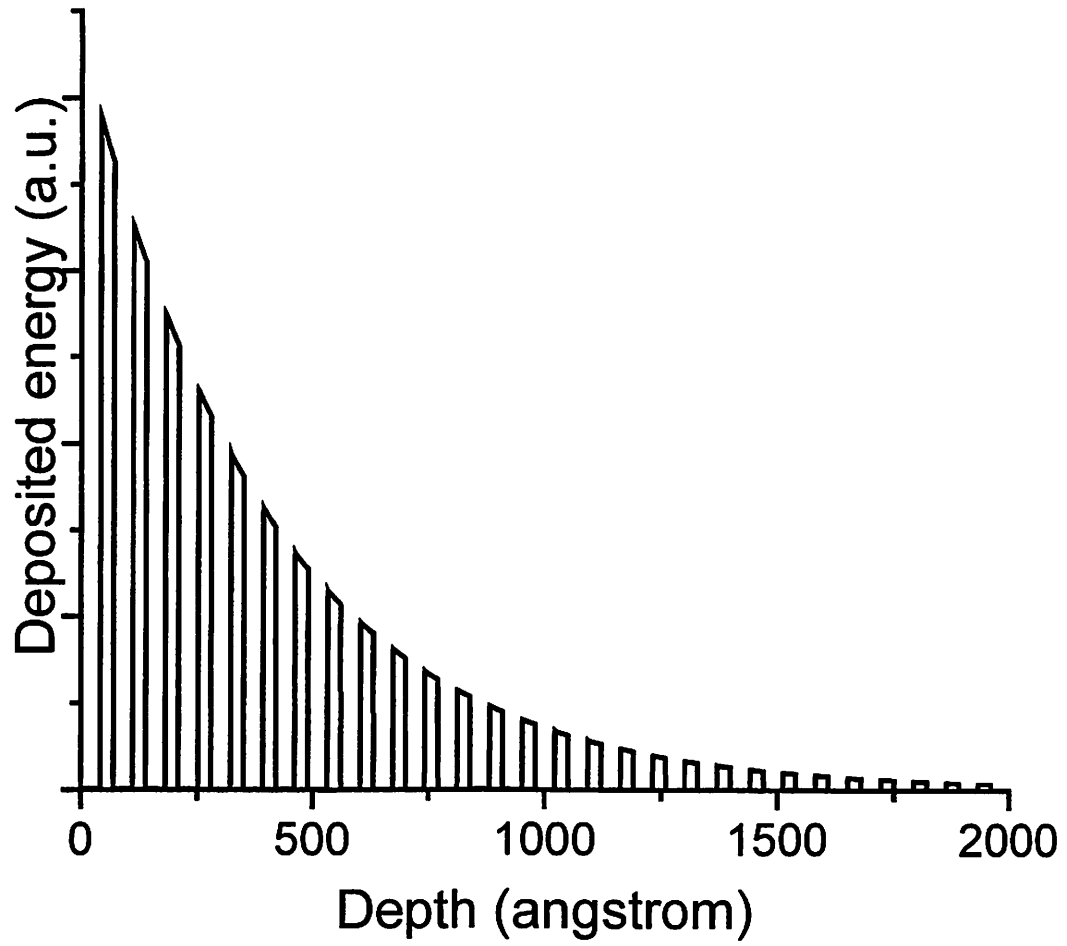


Figure 5-2 The spatial profile of optically deposited energy for a Mo/Si multilayer with  $d$

$= 70 \text{ \AA}$  and  $\Gamma = 0.4$ .

and  $\rho$  is the density. The stress is set up primarily in the Mo layers, and it has an exponential-decay shape with a decay distance determined by  $\alpha_{Mo}$ .

### 5.3 Sensitivity function

The elastic strain in the multilayer induces a change  $\Delta R(\tau)$  of the optical reflectivity. Since the strain is always small, we can define a “sensitivity function”  $f(z)$ [5.6]-[5.7]

$$\Delta R(\tau) = \int f(z)\eta(z, \tau) dz \quad (5.8)$$

To calculate  $f(z)$ , we suppose that there exists a  $\delta$ -function strain at a depth  $z'$

$$\eta(z) = \delta(z - z') \quad (5.9)$$

This causes a discontinuity in the optical properties at  $z = z'$ , and a reflection coefficient  $r'$  at this depth given by[5.7]

$$r' = \frac{i2\pi}{\lambda_0} \left( \frac{\partial n}{\partial \eta} + \frac{\partial \kappa}{\partial \eta} \right) \quad (5.10)$$

where  $\lambda_0$  is the light wavelength in vacuum, and  $n$  and  $\kappa$  are the real and imaginary parts of the index of refraction. It is then straightforward to calculate the new transfer matrix and the new reflectance  $R'$  following the procedure in §5.2. The reflectivity change  $\Delta R$  obtained this way is equal to  $f(z')$  according to Eq. (5.8). The general form of  $f$  in a *bulk* material is an exponentially-damped oscillation with a nonzero phase at the surface  $z = 0$ . The periodicity of this oscillation is half the wavelength of light in the material. The range of  $f$  is determined by the absorption length of the light. For a *multilayer*,  $f$  has a more complicated shape due to the additional periodicity of the structure. In reference

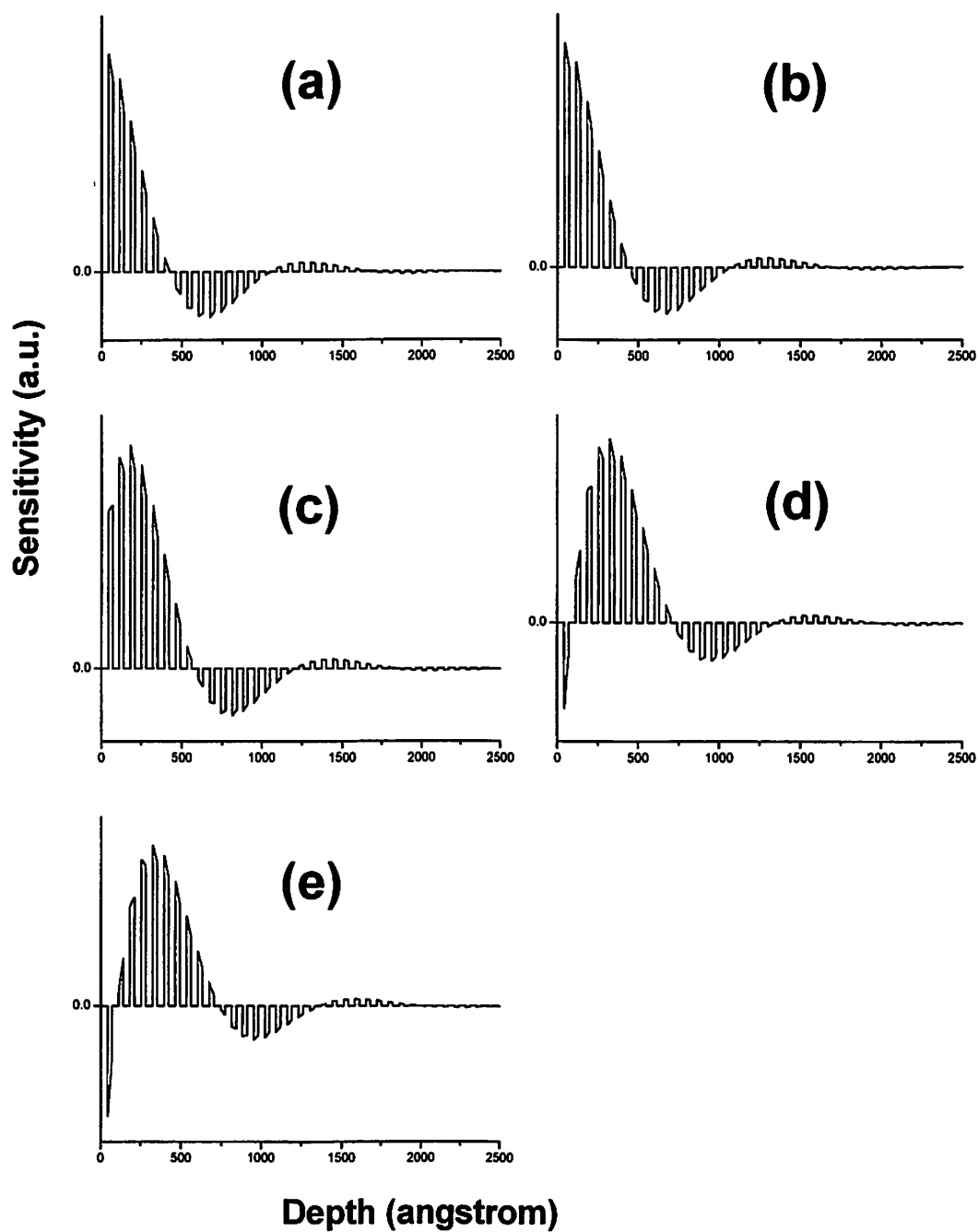


Figure 5-3 The sensitivity function  $f(z)$  for various ratios of  $\partial n / \partial \eta$  to  $\partial \kappa / \partial \eta$  in Mo: (a) 100:1, (b) 10:1, (c) 1:1, (d) 1:10, and (e) 1:100.

[5.7] and [5.8], it is found that in a-Si:H the strain-induced changes in the optical reflectivity are much smaller than in other materials. Therefore I assume that  $\partial n / \partial \eta$  and  $\partial \kappa / \partial \eta$  are negligible in silicon and thus  $f = 0$  in Si layers. Figure 5-3 shows the calculated  $f(z)$  for various ratios of  $\partial n / \partial \eta$  to  $\partial \kappa / \partial \eta$  in molybdenum. This ratio determines the phase of the damped oscillation (envelope of the square wave) at  $z = 0$ . For the calculation of  $\Delta R$  in this chapter, I use the  $f$  with  $\partial n / \partial \eta : \partial \kappa / \partial \eta = 1 : 1$ . In fact, not much difference is observed using a different  $f(z)$  curve or even assigning a small non-zero  $\partial n / \partial \eta$  and  $\partial \kappa / \partial \eta$  in Si.

## 5.4 Calculation of $\Delta R$

### 5.4.1 Approach 1

To calculate  $\Delta R(\tau)$  for a multilayer, first we have to solve the 1-D equations of elasticity numerically:

$$\sigma(z, \tau) = 3 \frac{1 - \mu}{1 + \mu} B \eta(z, \tau) - 3 B \beta \Delta T(z, \tau), \quad (2.4)$$

and

$$\rho \frac{\partial^2 u}{\partial \tau^2} = \frac{\partial \sigma}{\partial z} \quad (2.5)$$

$$\left( \eta \equiv \frac{\partial u}{\partial z} \right)$$

A way to simplify the calculation is to assume that the light pulse sets up an initial stress  $\sigma(z, 0)$  *instantaneously*, and neglect the thermal expansion term (the last term) in Eq. (2.4)[5.9]. In other words, we solve a simplified set of equations of elasticity

$$\left\{ \begin{array}{l} \sigma(z,\tau) = 3 \frac{1-\mu}{1+\mu} B\eta(z,\tau) \\ \rho \frac{\partial^2 u}{\partial \tau^2} = \frac{\partial \sigma}{\partial z} \end{array} \right. \quad (5.11)$$

with initial conditions

$$\sigma(z,0) = \frac{-3B\mathcal{W}(z)\beta}{C\rho} \quad \text{and} \quad u(z,0) = 0$$

The boundary condition requires that the strain be free at the surface:

$$\sigma(0,\tau) = 0$$

This approach reduces computation time by neglecting the time-varying driving term  $3B\beta\Delta T(z,\tau)$  in Eq. (2.4), which corresponds to a thermal stress due to lattice expansion. Consequently, the non-vibrational signal related to lattice heating will be absent in the calculated  $\Delta R$  curve. Nevertheless, the acoustic vibrations of interest presumably will not be affected much by this approximation.

A program solving these partial differential equations in a multilayer structure was constructed with a finite difference scheme[5.10]-[5.13] which is second-order accurate in both space and time variables[5.14]. Abrupt Mo/Si interfaces were assumed. The stepsizes of the spatial and temporal grids were  $1 \text{ \AA}$  and 10 fs, respectively. The total time period for this simulation is 500 ps (50,000 time steps). A calculated  $\Delta R(\tau)$  for a multilayer with  $d = 70 \text{ \AA}$  and  $\Gamma = 0.4$  is shown in Fig. 5-4(a). The response is dominated by an undamped oscillatory signal at a frequency of 1.02 THz. This is the frequency of the surface mode in the 2<sup>nd</sup> gap. There is also extra structure in  $\Delta R(\tau)$ , which contains

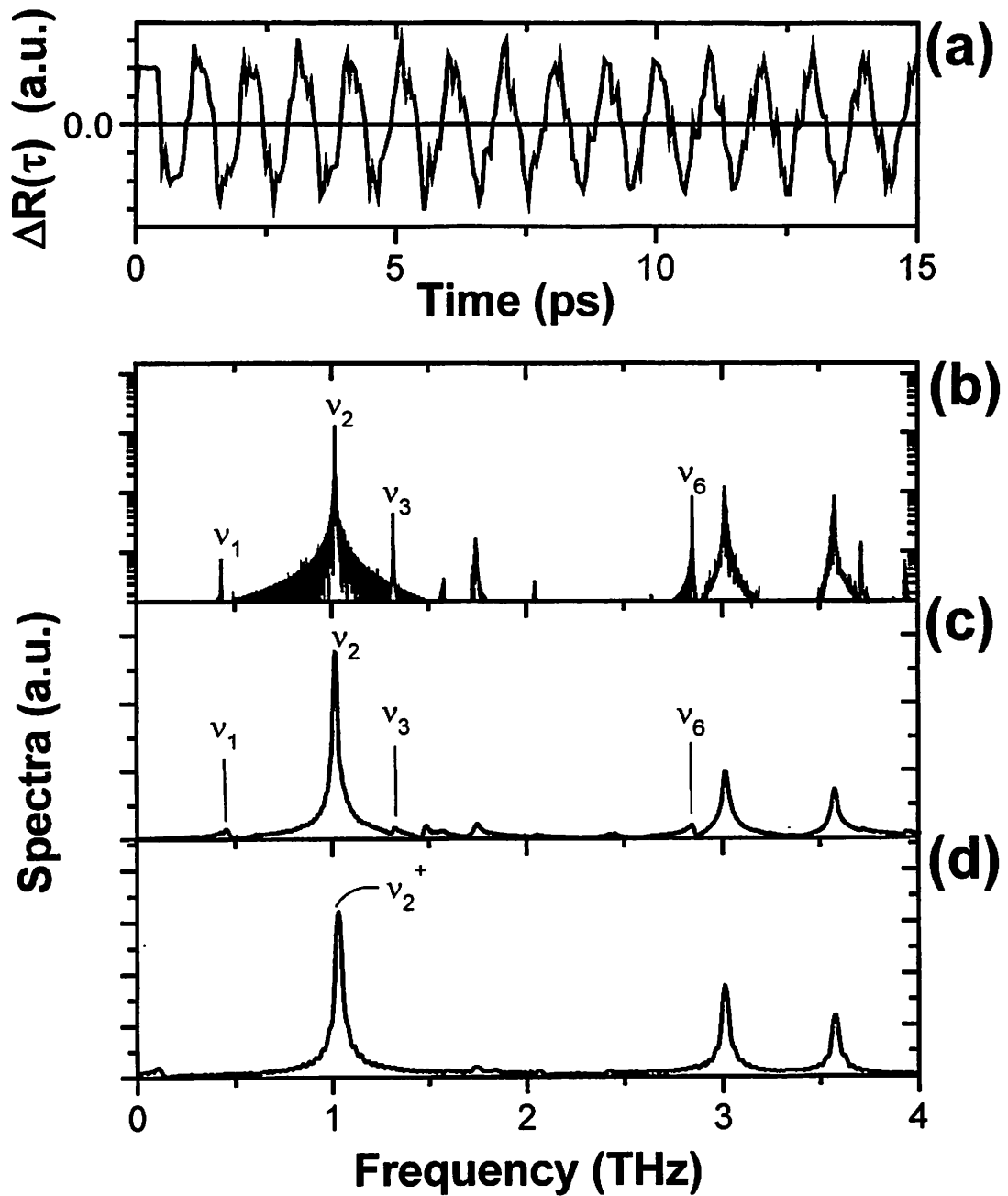


Figure 5-4 (a)  $\Delta R(\tau)$  for a multilayer with  $d = 70 \text{ \AA}$  and  $\Gamma = 0.4$  using approach 1. (b) The corresponding vibration spectrum (semi-log). (c) The spectrum with  $T_a = 15$  ps. (d) The spectrum for a multilayer begins with molybdenum.

frequency components above and below  $v_2$ . This extra structure is due to the other surface modes and bulk modes of the multilayer. Fig. 5-4(b) shows the vibration spectrum (semi-logarithmic) by taking a Fourier transform of the derivative of  $\Delta R(\tau)$ . Several surface modes appeared on the spectrum and were labelled. The 2<sup>nd</sup>-gap mode was most favorably excited as expected. Some spikes other than the labelled surface modes were also found to exist. These are the bulk modes near the upper or lower edges of the frequency gaps which have a very small group velocity and stay near the surface for tens of picoseconds. For the bulk modes away from the gaps, the group velocity is higher and they propagate out of detection range in a much shorter time.

One problem in our simple simulation is that the vibrations are undamped because the equations we used are *adiabatic* in nature. To keep the problem simple, we circumvent the trouble of incorporating loss mechanisms into simulation by enforcing an exponential-decay time constant  $T_a$  on the calculated  $\Delta R(\tau)$  curves. As an example, Fig. 5-4(c) shows a spectrum (linear scale) with  $T_a = 15$  ps. The 2<sup>nd</sup>-gap mode becomes less pronounced, and the spectral width of all peaks are now reasonably wide due to the imposed lifetime. However, there is still a disagreement between this spectrum and the real one in Fig. 4-2(a): the calculated relative strength for each mode is by no means close to the experiment. Specifically, the excitation of higher-frequency vibrations was overestimated. The primary reason for this discrepancy is that we made an unrealistic assumption of *instantaneous* excitation. It corresponds to a very broad continuum in the spectrum and consequently, vibrations at very high frequencies still have good chances of being excited. To solve this problem, a finite period of time for stress build-up has to be considered. We will discuss this more in the next section.

According to the results of §2.2.2, surface modes do not exist for the multilayer configuration with molybdenum as the topmost layer. As a test for the validity of our program, we also calculated  $\Delta R(\tau)$  in this case. The spectrum (Fig. 5-4(d)) shows that indeed, all of the surface modes have completely disappeared, but many bulk modes near band edges can still be excited and detected. (The peak labelled as  $\nu_2^+$  is actually the bulk modes near the upper edge of the 2<sup>nd</sup> gap, although it is very close to  $\nu_2$ .)

### 5.4.2 Approach 2

Although the first approach is mathematically simpler and allows us to study, to some extent, the vibrational behavior of a multilayer structure, it cannot yield a very satisfying result that helps to interpret experimental observations. To do a better job, we need to consider the finite build-up time for thermal stress and monitor the subsequent evolution of the thermal stress profile, which continuously drives the structure into vibration. The exact equation (2.4), instead of (5.11) has to be solved, and so the heat diffusion equation governing the evolution of lattice temperature  $\Delta T(z, \tau)$  has to be added in the computation:

$$\frac{\partial^2 T}{\partial z^2} + S(z, \tau) = \frac{1}{D} \frac{\partial T}{\partial \tau} \quad (4.6)$$

The source term  $S(z, \tau)$  is assumed to have the following form:

$$S(z, \tau) = \frac{1}{t_1 \sqrt{\pi}} \frac{W(z)}{k} e^{-\tau^2 / t_1^2} \quad (5.12)$$

where  $W(z)$  is the energy deposited by a laser pulse,  $k$  is the thermal conductivity, and the variable  $t_1$  takes into account the finite laser pulse width and the delay due to electron -



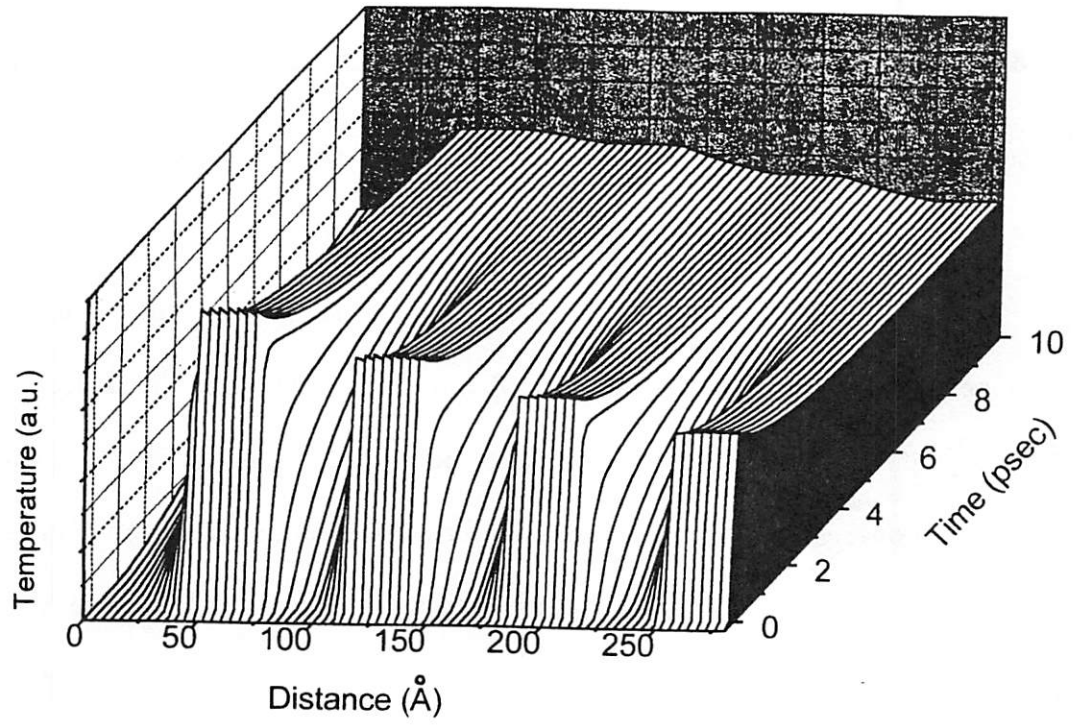


Figure 5-5 The calculated spatiotemporal profile for temperature rise in a Mo/Si multilayer ( $d = 70 \text{ \AA}$  and  $\Gamma = 0.4$ ) with  $t_1 = 0.1 \text{ ps}$ .

phonon heat exchange in Mo. For each time step, I divided the 10-fs interval into 250 increments and solved Eq. (4.6) in each sub-loop. The updated temperature profile after 250 cycles was then fed into Eq. (2.4) for computing the stress and strain. Fig. 5-5 shows an example of the calculated spatiotemporal temperature profile in a Mo/Si multilayer ( $d = 70 \text{ \AA}$  and  $\Gamma = 0.4$ ) with  $t_1 = 0.1 \text{ ps}$ . It takes about 5 to 10 ps for the temperature profile to equalize among Mo and Si layers. This local thermalization time is mainly determined by the thermal conductivity of amorphous silicon. For a purely metal multilayer such as Mo/Be or Cu/W, this process occurs in a much shorter time scale, and the excitation pattern of acoustic waves will be different.

Fig. 5-6(a)-(d) display the  $\Delta R(\tau)$  traces calculated with the new approach for  $t_1 = 400, 500, 600$  and  $700 \text{ fs}$ , respectively ( $d = 70 \text{ \AA}$  and  $\Gamma = 0.4$ ). Apart from an oscillatory signal due to acoustic waves, we see a familiar non-vibrational signal due to thermal expansion, which shows up in every experimentally measured curves. Clearly the ratio of vibrational to non-vibrational parts is a very sensitive function of  $t_1$ . The amplitude ratio of the 2<sup>nd</sup> surface mode to the non-vibrational signal ( $\Delta R_{v_2} / \Delta R_{non-vib}$ ) is about 0.40, 0.16, 0.05 and 0.015 for  $t_1 = 400, 500, 600$  and  $700 \text{ fs}$ , respectively. The trend that this ratio drops as we increase  $t_1$  is obviously because a rounded step excitation has less high-frequency contents. This argument also explains the fact that the vibration amplitude drops as  $d$  is decreased from  $325 \text{ \AA}$  to  $69 \text{ \AA}$  (see §4.1). Compared with the experimentally measured ratio  $\Delta R_{v_2} / \Delta R_{non-vib} = 0.06$ ,  $t_1 = 600 \text{ fs}$  is the closest to reality. Since this  $t_1$  is considerably longer than the laser pulse width  $190 \text{ fs}$ , it offers a good

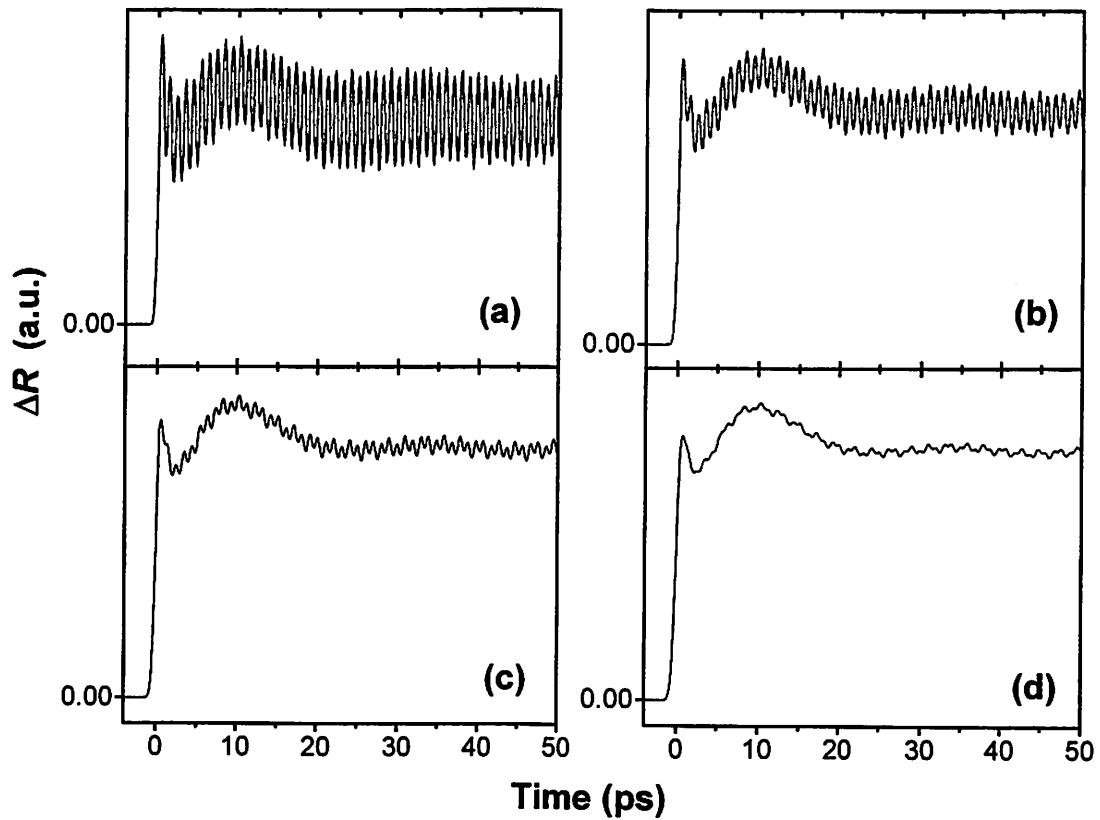


Figure 5-6 The  $\Delta R(\tau)$  traces calculated via approach 2 for  $t_1 =$  (a) 400, (b) 500, (c) 600, and (d) 700 fs, respectively ( $d = 70 \text{ \AA}$  and  $\Gamma = 0.4$ ).

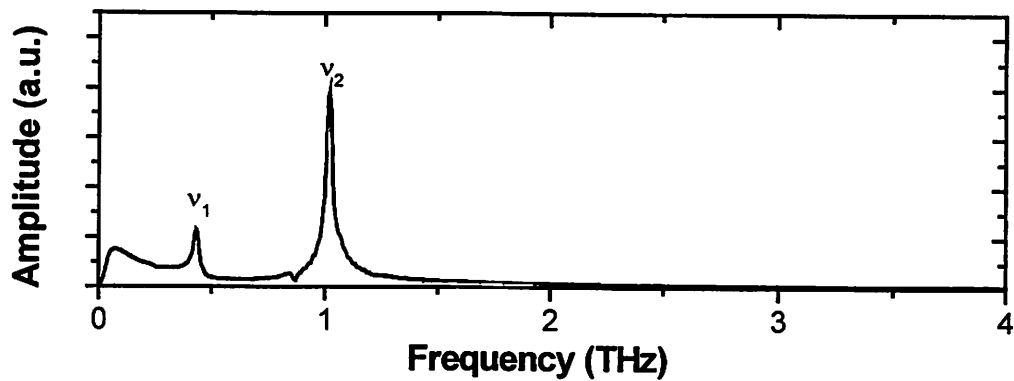


Figure 5-7 The corresponding spectrum for the curve with  $t_1 = 600$  fs.

estimate to the electron-phonon interaction time  $\tau_{e-p}$  in molybdenum. The corresponding spectrum for the curve with  $t_1 = 600$  fs is shown in Fig. 5-7. As before, a 15-ps exponential decay time was enforced on the calculated  $\Delta R(\tau)$ . The relative amplitudes for the 1<sup>st</sup> and the 2<sup>nd</sup> surface modes are also in very good agreement with the experiment. Another interesting feature of the real spectrum that we want to explain is the strange lineshape near  $\nu_2$  for  $\Gamma = 0.4$  (see Fig. 4-6(a)). Unfortunately, computer simulation did not reproduce this lineshape at  $\Gamma = 0.4$ . However, the assumed 2-sublayer structure in our calculation deviates from the real one due to silicide formation, and also the  $\Gamma$  used in Fig. 4-6 is not a well-defined number that really represent the Mo layer thickness. Therefore it is fair to try a certain range near “ $\Gamma$ ”=0.4. Fig. 5-8(a)-(e) display the calculated spectra with  $\Gamma$  varying from 0.414 to 0.357. At  $\Gamma = 0.37 \sim 0.38$ , the lineshape around  $\nu_2$  starts to resemble that in Fig. 4-6(a) – featuring asymmetric double peaks with a sharp dip in between. Note that the same lineshape can be generated with our first simulation approach, which precludes the possibility that it is caused by some nonlinear coupling among waves.

As we have mentioned in §5.4.1, some bulk modes close to the upper or lower edges of the frequency gaps can be excited and detected due to their low group velocity. We attribute the side peak next to  $\nu_2$  simply to the bulk modes near the upper edge of the 2<sup>nd</sup> gap. The relative excitation strengths for these bulk modes depend on the geometry of the multilayer because certain boundary conditions at interfaces and at the surface need to be satisfied. The calculated spectrum for  $\Gamma = 0.5$  was shown in Fig. 5-8(f) for comparison. The peak at  $\nu_2$  has an asymmetric shape, which is also in agreement with

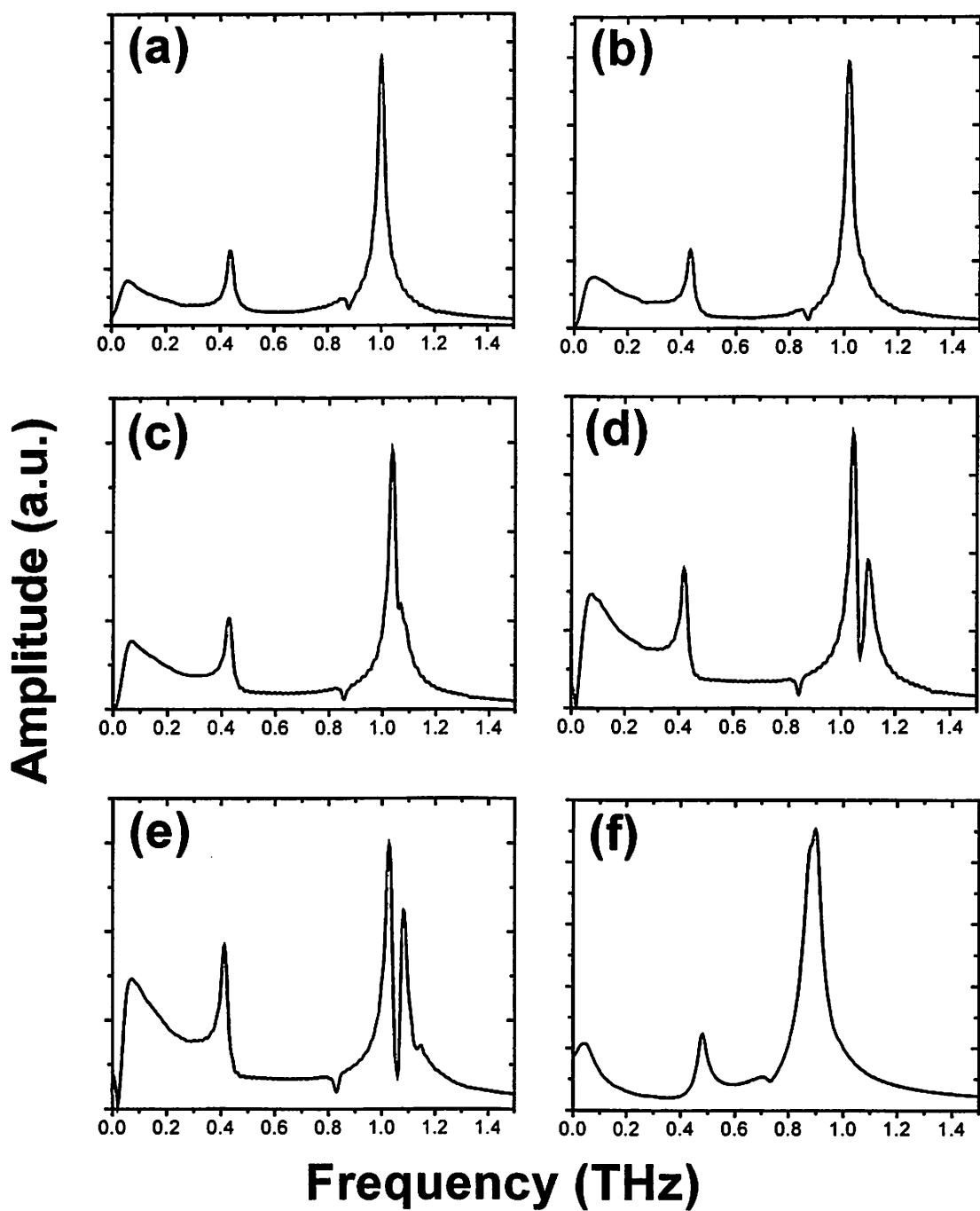


Figure 5-8 The calculated spectra with various  $\Gamma$  values: (a) 0.414 ( $d_{mo} = 29 \text{ \AA}$ ), (b) 0.4 ( $d_{mo} = 28 \text{ \AA}$ ), (c) 0.386 ( $d_{mo} = 27 \text{ \AA}$ ), (d) 0.371 ( $d_{mo} = 26 \text{ \AA}$ ), (e) 0.357 ( $d_{mo} = 25 \text{ \AA}$ ), and (f) 0.5 ( $d_{mo} = 35 \text{ \AA}$ ).

the real spectrum in Fig. 4-6(b). The low frequency components (below  $\nu_1$ ) in Fig. 4-6(a) and (b) are considerably smaller than the simulated results, which is probably owing to the cancellation effect of our alternating-pump detection scheme.

## References

- [5.1] See for example, O.S. Heavens, *Optical properties of thin solid films*, Dover Publications, New York, 1965.
- [5.2] In fact,  $t_m'$  is the transmission coefficient for an electromagnetic wave incident from layer  $m$  back to layer  $(m-1)$ , whereas  $r_m$  is the reflection coefficient for a wave incident from layer  $(m-1)$  into  $m$ .
- [5.3] J.H. Underwood and T.W. Barbee, Jr., *Applied Optics*, **20**, 3027 (1981).
- [5.4] *Landolt-Bornstein Numerical Data and Functional Relationships in Science and Technology*, Springer-Verlag, Berlin-Heidelberg, 1982, New Series, **III/17a**, pp. 386-387.
- [5.5] Same as reference [3.7].
- [5.6] H.T. Grahn, H.J. Maris, and J. Tauc, *IEEE J. Quantum Electron.*, **25**, 2562 (1989).
- [5.7] C. Thomsen, H.T. Grahn, H.J. Maris, and J. Tauc, *Physics Review*, **B 34**, 4129 (1986).
- [5.8] C. Thomsen, H.J. Maris, and J. Tauc, *Thin Solid Films*, **154**, 217 (1987).
- [5.9] H.T. Grahn, H.J. Maris, J. Tauc, and B. Abeles, *Physics Review*, **B 38**, 6066 (1986).
- [5.10] A.R. Mitchell and D.F. Griffiths, *The Finite Difference Method in Partial Differential Equations*, John Wiley & Sons Ltd., 1980.
- [5.11] G.E. Forsythe and W.R. Wasow, *Finite-Difference Methods for Partial Differential Equations*, John Wiley & Sons, Inc., 1960.
- [5.12] V. Vemuri and W.J. Karplus, *Digital Computer Treatment of Partial Differential Equations*, Prentice-Hall, Inc., 1981.

[5.13] V.G. Ganzha and E.V. Vorozhtsov, *Numerical Solutions for Partial Differential Equations : Problem Solving Using Mathematica*, CRC Press, Inc., 1996.

[5.14] G. Cohen and P. Joly, *SIAM Journal of Numerical Analysis*, **33**, 1266 (1996).



# Chapter 6. Conclusions

In previous chapters, the experimental and theoretical studies of picosecond ultrasonics in Mo/Si EUV multilayers have been presented. Much has been accomplished with this dissertation. Specifically, a strong foundation has been made for applying this technique in nondestructive characterization of multilayers. This chapter will summarize the works in previous chapters and point out some future directions.

## 6.1 Conclusions

This section lists briefly the main conclusions drawn from each of the four preceding chapters in this dissertation. The subsections follow the chapter organization.

### 6.1.1 Analytical theory of picosecond ultrasonics

The basic theory for acoustic wave generation via optical pulse excitation and the subsequent evolution according to the elastic wave equation were discussed in Chapter 2. The detection of these acoustic waves is based on a strain-induced change in optical reflectivity. In bulk materials, a bipolar strain pulse propagating at the longitudinal sound velocity  $c$  is excited. By measuring the delay time and amplitude of the echoed pulse, one can determine  $c$  (or the film thickness) and the acoustic attenuation coefficient. In a superlattice, more complicated vibrations can be excited in addition to the propagating pulse. The periodicity imposed by the structure introduces new features in the acoustic-phonon dispersion curve: a reduced first Brillouin zone, the opening of frequency gaps (stop bands), and the existence of surface modes within these gaps. By solving an elastic eigenvalue problem, the folded dispersion curve for a 2-sublayer

superlattice can be calculated by an analytical equation (2.29):

$$\cos( qd ) = \cos( \omega d_1 / c_1 ) \cos( \omega d_2 / c_2 ) - \frac{(p_{12} + p_{21})}{2} \sin( \omega d_1 / c_1 ) \sin( \omega d_2 / c_2 ) \quad (2.29)$$

And the frequencies for the surface modes are determined by Eq. (2.38)

$$p_{12} \tan( \omega d_1 / c_1 ) + \tan( \omega d_2 / c_2 ) = 0 \quad (2.38)$$

The theory was further extended to include an  $n$ -sublayer structure with arbitrary cap layers. For example, a Mo/Si multilayer with silicide interdiffusion layers can be approximately treated as a 4-sublayer superlattice (Mo / silicide #1/ Si /silicide #2) with a SiO<sub>2</sub>/Si cap layer. The impact of silicide and oxide layers roughly scales inversely with  $d$ .

This formalism, although offers an expression for eigen-mode frequencies, does not deal with the excitation strengths and vibrational lineshapes. To obtain this information, numerical simulations of the elastic wave equation were carried out in Chapter 5.

### 6.1.2 Experimental setup – the alternating-pump technique

Chapter 3 described the details of our experimental setup for picosecond ultrasonics using a time-resolved transient reflectivity technique. In addition to some methods for enhancing the S/N ratio, such as lock-in detection and an auto-balanced detector circuit, a novel alternating-pump technique was proposed and implemented.

The basic idea of this technique is to suppress the large non-vibrational signal by a smart detection scheme, and thereby eliminating the accompanying noise. We have demonstrated the capability of this technique to suppress the low-frequency laser fluctuation noise by up to 20 dB. In addition, it can also selectively reveal the weaker

1<sup>st</sup>-gap surface mode by suppressing the stronger 2<sup>nd</sup>-gap mode, and helps to increase the measurement precision for  $v_1$ .

### 6.1.3 Experimental results

The results of various experimental studies as well as demonstrations of the utility of picosecond ultrasonics as a nondestructive characterization tool for Mo/Si multilayers were presented in chapter 4.

As many as three surface modes ( $n = 1, 2,$  and  $6$ ) were observed in our Mo/Si multilayer samples. The 1<sup>st</sup>- and the 2<sup>nd</sup>-gap modes were found in all well-coated samples, but the 6<sup>th</sup>-gap mode diminishes rapidly as  $d$  decreases and can not be detected in the samples with  $d \sim 70 \text{ \AA}$ . The relation of these frequencies  $v_n$  with  $(d, \Gamma)$  was studied experimentally and compared to the analytical theory in Chapter 2. Each  $v_n$  was found inversely proportional to  $d$ , and the ratio of any two of them depends only on  $\Gamma$ . These relations can be exploited to extract the multilayer parameters  $(d, \Gamma)$  by measuring  $v_1$  and  $v_2$  simultaneously. For example, we successfully mapped the thickness profile of a 2% graded sample. Also, we performed a cross-correlation experiment with at-wavelength EUV reflectometry on seven test samples. The results of these two techniques were in good agreement except for a systematic offset due to a calibration drift.

The non-vibrational component of the  $\Delta R$  signal due to hot electrons and lattice heating was also studied. The  $\Delta R(\tau)$  curves of Mo and Si films were measured in comparison with those of Mo/Si multilayers with various  $\Gamma$ . It is found that the small thermal conductivity in amorphous silicon hampers the heat diffusion process and causes

the observed slow decay of  $\Delta R(\tau)$  curves.

Chapter 4 also discussed the laser damage to multilayers. Although it has a significant impact on the surface modes, the effect on EUV reflectivity was negligible. The damage is found to be localized laterally and shallow in depth. The mechanism for this damage is most likely due to changes in material properties, probably because of relaxation of the intrinsic film stress.

#### 6.1.4 Numerical simulations

Numerical simulations for the physical processes of the generation, evolution, and detection of acoustic waves in Mo/Si multilayers were performed and discussed in Chapter 5. The spatial forms of the optically deposited energy  $W(z)$  and the sensitivity function  $f(z)$  were calculated using a transfer-matrix method in electromagnetics. To compute the spatiotemporal profile of the strain waves  $\eta(z, \tau)$ , two simulation approaches for solving equations of elasticity were used. For simplicity, the electronic contribution to  $\Delta R$  was neglected and the acoustic attenuation was not considered.

Approach 1 ignored a time-varying thermal expansion term, which acts as a driving force in the equations of elasticity, and treated the problem as a simple relaxation process of an initial stress field. Neglecting thermal expansion resulted in absence of the non-vibrational signal. Nevertheless, the vibration behaviors in a multilayer can still be probed with this approach. Various surface and bulk modes were excited and the frequencies agreed with the values predicted by the analytical equations in Chapter 2. A more serious problem of this approach is the assumption of an instantaneously built-up stress field, which leads to an incorrect excitation amplitudes for vibration modes.

Approach 2 incorporated the heat diffusion equation into computation to track the

evolution of the temperature profile. Instead of assuming an instantaneous initial stress, a Gaussian heat source with an adjustable time constant,  $t_1$ , was used to account for the finite laser pulse width and the delay time for electron-to-lattice heat transfer. The amplitude of vibrations is a sensitive function of  $t_1$ , and decreases rapidly (in a time scale of 100 fs) with  $t_1$ . Simulation results show that this  $t_1$  delay is about 600 fs, which is a rough estimate for the electron-phonon interaction time in Mo.

With this approach, the calculated relative strengths of vibration modes agree well with the experiment. In addition, an experimentally observed spectral lineshape (Fig. 4-6(a)) featuring asymmetric double peaks (around  $\nu_2$ ) and a sharp dip in between was reproduced by our simulation with a slightly different  $\Gamma$ . The weaker peak slightly above  $\nu_2$  is attributed to the bulk modes near the upper edge of the 2<sup>nd</sup> gap ( $\nu_2^+$ ).

## 6.2 Future directions

### 6.2.1 Experimental setup

Several modifications can be made on our present setup to improve the signal level and overall performances of the system:

- (1) To further enhance the S/N ratio, an interferometric method[6.1] detecting the displacement of the surface of the sample can be implemented in conjunction with our present alternating-pump setup. It has been demonstrated by B. Perrin *et al.* that the interferometric method offers a stronger signal level than photoreflectance measurements. The alternating-pump scheme can be easily integrated with their interferometric setup, and the combination hopefully can further improve the detection limit.

- (2) As mentioned in Chapter 4, the dc offset in the  $\Delta R(\tau)$  traces due to accumulated heat deposited by the light pulse train is proportional to  $\omega_c^{-1/2}$ , where  $\omega_c$  is the chopping frequency of the modulator. By increasing  $\omega_c$  from 100 kHz to 10 MHz, this offset (and its accompanying noise) can be reduced by a factor of 10. In addition, the laser fluctuation noise is very low at such a high frequency. Currently, our  $\omega_c$  was limited by the bandwidth of the auto-balanced detector circuit and the frequency response of the AO modulator. Replacing them with higher-frequency counterparts will hopefully reduce the noise and improve the detection limit on  $\Delta R$ .
- (3) The data-averaging time can be reduced by increasing the scan rate ( $\sim 2$  Hz for now) or decreasing the number of traces ( $= 256$  currently) for averaging. The choice for these numbers is not limited by the equipment but by the signal-to-noise ratio. With the 100- $\mu$ s minimum time constant of our RF lock-in amplifier, the upper limit for the scan rate is 10 Hz, for a 1000-point trace. If the S/N ratio allows this scan rate and requires only 128 traces for averaging, then the data-averaging time can be reduced from 2 minutes to 13 seconds.
- (4) A calibration drift in the position output ( $V_{po}$ ) of the optical delay line was found as mentioned in §4.7. A more reliable and accurate way of real-time position detection such as optical interferometry can solve this problem.
- (5) The light pulsewidth in our setup is limited by the dispersion in the 6-cm-thick AO crystal. By using a thinner crystal and, if possible, using a better laser system with shorter pulses, our temporal resolution can be reduced to less than 100 fs.

### **6.2.2 Experiments and applications**

There are some other related experiments and applications that can be performed

with this technique:

- (1) In principle, our alternating pump technique can be applied to characterization of other multilayer structures such as Mo/Be or Ru/Si EUV multilayers, and W/C multilayers for soft x-rays. It can also be used for semiconductor or metal superlattices such as AlGaAs/GaAs, Ag/Al, etc.
- (2) Since the laser spot sizes are small and the laser beams are not incident at a grazing angle, this technique can be used for multilayers coated on curved optics, which cannot be probed by x-ray diffraction.
- (3) In Section 4.4,  $d$  and  $\Gamma$  were extracted by interpolation among five empirical data points. To achieve a better accuracy, more reference data points near  $\Gamma = 0.4$  are needed for interpolation.
- (4) On the vibration spectrum, the side peak and the adjacent sharp dip just above the  $\nu_2$ -peak are signatures for Mo/Si multilayers with  $\Gamma$  near 0.4. By carefully studying the relation between their frequencies and the multilayer geometry, we can probably make use of them to improve our measurement precision.
- (5) For coating EUVL optics, it is very important to have the process of thin film deposition under control to achieve a uniform thickness of multilayers. It is desirable to have an in-situ monitoring tool and a feedback loop to control the deposition rate. This picosecond-ultrasonic technique can be implemented in the deposition chamber to serve this purpose.

### 6.2.3 Numerical simulations

A few modifications can be added to our simulation program:

- (1) To reproduce the damping of vibrations and the finite linewidths in the real data, we

must consider acoustic attenuation in the structure. Many mechanisms such as electron-phonon interaction, phonon-phonon interaction, scattering and absorption of phonons at interfaces and the free surface, scattering at grain boundaries in the polycrystalline Mo layers, ... etc. might contribute to the acoustic attenuation. In particular, W. Chen *et al.*[6.2] pointed out that a reflection loss of  $\sim 6\%$  at the free surface is a very likely culprit for surface-mode attenuation in Al/Ag superlattices.

- (2) For an accurate simulation in the first 1 ps, the heat exchange between hot electrons and the lattice in Mo should be included. The process is governed by a set of coupled nonlinear differential equations[6.3]:

$$C_e(T_e) \frac{\partial T_e}{\partial \tau} = k \frac{\partial^2 T_e}{\partial z^2} - g(T_e - T_l) + S(z, \tau) \quad (6.1)$$

$$C_l \frac{\partial T_l}{\partial \tau} = g(T_e - T_l) \quad (6.2)$$

where  $C_e$  and  $C_l$  are the electronic and lattice heat capacities,  $k$  is the thermal conductivity, and  $T_e$  and  $T_l$  are the electron and lattice temperatures, respectively.  $S(z, \tau)$  represents the heat source term due to the laser pulse.  $g$  is the electron-phonon coupling constant. Note that the electronic heat capacity  $C_e$  depends linearly on  $T_e$ . The contribution to stress by a free-electron gas is[6.2]:

$$\sigma_{ij}(z) = -\frac{2}{3} W(z) \delta_{ij} \quad (6.3)$$

where  $W(z)$  is the energy deposited per unit volume at a depth  $z$ . The thermal stress due to the lattice is given by

$$\sigma_{ij}(z) = -\gamma_l W(z) \delta_{ij} \quad (6.4)$$

where  $\gamma_l$  is the lattice Gruneisen constant and is generally in the range 1 - 3. So the



lattice stress is somewhat larger than the electronic stress given the same energy. By incorporating Eqs. (6.1)–(6.4) with the equations of elasticity, we can study the thermal-elastic behaviors in the subpicosecond regime.

- (3) The initial stress difference between Mo and Si layers is smoothed out by the diffusion of electrons that occurs before they lose their energy to the phonon bath[6.4]. An extra parameter describing this smoothing can be added into the program to simulate this effect.
- (4) As mentioned in Chapter 5, our computer program was constructed with finite difference scheme accurate to the second order in space and time. According to reference [6.5], a fourth-order finite difference scheme in layered media can be constructed, and it offers a better accuracy and stability.
- (5) Interface roughness and interdiffusion might play a role in acoustic attenuation and could also affect the vibration behavior of the multilayer stack. A proper treatment of the interfaces is needed for a more realistic simulation.

## References

- [6.1] B. Perrin, B. Bonello, J.-C. Jeannet, and E. Romantet, *Progress in Natural Science*, **6**, S-444 (1996).
- [6.2] W. Chen, Y. Lu, H.J. Maris and G. Xiao, *Physical Review*, **B 50**, 14506 (1994).
- [6.3] S.I. Anisimov, B.L. Kapeliovich, and T.L. Perel'man, *Soviet Physics JETP*, **39**, 375 (1975).
- [6.4] R.W. Schoenlein, W.Z. Lin, J.G. Fujimoto, and G.L. Eesley, *Physical Review Letters*, **58**, 1680 (1987).
- [6.5] G. Cohen and P. Joly, *SIAM Journal of Numerical Analysis*, **33**, 1266 (1996).